High Performance & Smart Manufacturing

(Article begins on next page)

04 August 2020

Doctoral Dissertation
Doctoral Program in Electronic Engineering (29th Cycle)

High Performance Smart Manufacturing

By

Francesco Perrucci
****

Supervisors:
Prof. Fabrizio Pirri
Prof. Luciano Scaltrito

Doctoral Examination Committee:
Prof. Benedetti Matteo, Referee, Università degli studi di Trento
Prof. Mazzolai Barbara, Referee, IIT – Istituto Italiano di Tecnologie

Politecnico di Torino
2018

Declaration

I hereby declare that, the contents and organization of this dissertation constitute my own original work and does not compromise in any way the rights of third parties, including those relating to the security of personal data.

Francesco Perrucci

2018

* This dissertation is presented in partial fulfillment of the requirements for **Ph.D. degree** in the Graduate School of Politecnico di Torino (ScuDo).

"Moving from interest to interest,

building skills in different areas,

synthesizing the knowledge acquired along the way"

E.Wapnick

Abstract

Digital evolution involves transversely manufacturing processes and production support tools by changing the physical characteristics of factories and consequently the corporate structures. Both roles and skills of the professional figures employed in the production field are transformed and redefined. Rapid prototyping technologies have changed the concept of product design and manufacture. The initial interest in these technologies was economical: help product development by producing prototypes, useful for both validation purposes and design optimization, quickly and by reducing costs. Therefore, corrections can be made in the early stages of the project, greatly reducing design costs. In addition, additive manufacturing, more flexible than traditional processes, does not involve the use of expensive molds, avoids excessive waste of material, and allows to realize objects composed by complex structures and undercuts. Additive Manufacturing has been shown to be one of the key factors for sustainable economic growth, increasing competitiveness and technological innovation with the potential to transform global manufacturing industry and influencing the environmental impact.

The Ph.D. research activity on High Performance & Smart Manufacturing has been held in Materials and Micro Systems Laboratory of Politecnico di Torino (ChiLab) and in collaboration with Microla Optoelectronics S.r.l..

First steps have been moved on the study of the Additive Manufacturing methodologies and techniques already present on the market. With 'High Performance Manufacturing' as keywords of the PhD activity, the optimization of stereolithographic printing process is only one aspect that has been taken into account.

The main part of the PhD research activity was dedicated to the improvement of additive manufacturing process. A first part relies on the study of new smart materials, with intrinsic features which provide to the printed objects a concrete function. For this purpose, a study about building process parameters on functionalized photosensitive polymer was conducted. Furthermore, aromatic polymers have been studied and laser processed with the intent to make them conductive and, in the future, reliable into additive manufacturing processes.

A second part was dedicated to the integration of stereolithographic processes both at micro and nano scale. The microfluidic filtration system developed in this study was designed to be used on a wide range of cells sorting/filtration as, for example, the blood cells. This activity was made possible thanks to the great collaboration

with the laboratory Laser Zentrum of Hannover (LZH, Germany). At the LZH laboratories, a two-photon polymerization (2PP) set-up allowed the fabrication of different nano-structures for microfluidic application.

The texture of this work is the following: in the first sections the theoretical basis related to the additive manufacturing technologies are explained. The second section is about the stereolithography process and, finally, the third section is completely dedicated to the experimental activity. The third section can be subdivided in three parts: printing process optimization, 3d printing of functionalized polymers and nano-micro-printing integration for MEMS applications.

Index

List of Figures

List of Tables

Chapter 1

1 Laser Physics and Theory

1.1 Introduction to Light and LASER

The term LASER is an acronym for "light amplification by stimulated emission of radiation". Laser radiation is an electromagnetic wave generated by an active medium [1] characterized by a specific wavelength strictly related to the number of electric and magnetic field oscillations per time unit (frequency). It is known that, for an electromagnetic wave, the relation between wavelength (λ) and frequency (f) is reported in Equation 1.1:

$$\lambda * f = c \qquad \text{Equation 1.1}$$

Where 'c' is the speed of light in vacuum (3 E+08 m/s). According to this relation, the wavelength decreases as frequency increases.
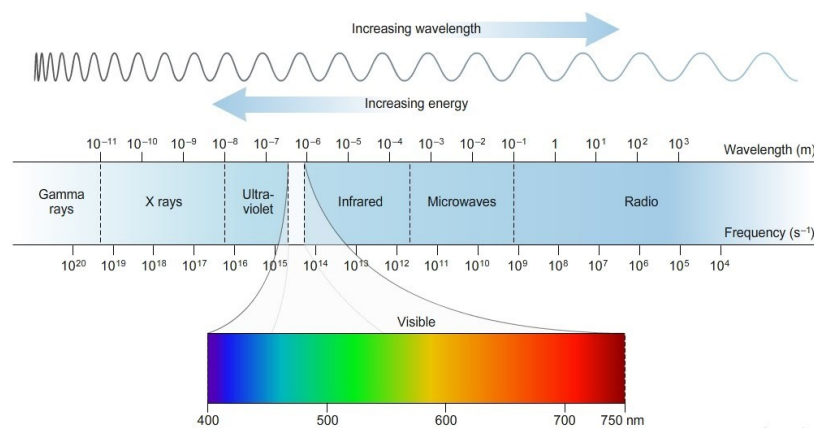
Figure 1.1 - Electromagnetic Spectrum

Figure 1.1 shows the electromagnetic spectrum; it is a commonly accepted scheme to identify different wavelength regions according to their effect on the matter but, actually, the boundary between the different regions are not so strict[2].

One of the peculiarities of light is its dual nature: it acts not only as a wave but also as a flow of discrete particles, called photons. The latter are energy carriers, each transporting an energy E as reported in Equation 1.2:

$$E = h * f = \frac{h * c}{\lambda}$$

<div align="right">**Equation 1.2**</div>

where h is Planck's constant, equal to $6.6*10^{-34}$ J·s. This equation indicates that the photon energy associated with a light wave increases as the wavelength decreases.

A LASER is known to be a monochromatic and collimated wave characterized by spatial and temporal coherence. The emission of coherent and collimated waves is the result of active medium pumping (energy transfer) and subsequent optical amplification. Thanks to these properties, LASER has become useful in science, engineering and technology as a highly focused energy carrier [3].

As previously said, a LASER is generated by an active medium, which can be solid, like crystals glasses or semiconductors (known as solid-state laser), liquid or gaseous: depending on the medium, the emission is characterized by certain power and wavelength. A further classification divides the LASER into four main categories: neutral atom lasers, ion lasers, molecular lasers and excimer lasers [3].

Typical commercially available lasers for material processing are reported in Table 1.1.

Table 1.1 - Commercially available laser and their applications [3]

Laser	Year of discovery	Commercialised since	Applications
Ruby	1960	1963	Metrology, medical applications, inorganic material processing
Nd-Glass	1961	1968	Length and velocity measurement
Diode	1962	1965	Semiconductor processing, biomedical applications, welding
He-Ne	1962		Light-pointers, length/velocity measurement, alignment devices
CO_2	1964	1966	Material processing-cutting/joining, atomic fusion
Nd-YAG	1964	1966	Material processing, joining, analytical technique
Ar+	1964	1966	Powerful light, medical applications, material processing
Dye	1966	1969	Pollution detection, isotope separation, scientific purposes due to wavelength tunability
Cu	1966	1989	Isotope separation
Excimer	1975	1976	Medical application, material processing, colouring
Ti-Saphire	1982		Scientic purposes: tunable ultrashort laser pulses due to the large bandwidth

Among them, CO_2 and Neodymium (Nd) based LASER sources are of great interest in industrial field.

1.2 Optical amplification

This chapter focuses on the functioning, and deepens some fundamentals, of LASER.

Prior to any discussion, it is important to define the concept of energy level, which is central to explain LASER operations. Indeed, the light amplification occurs when an atomic or molecular system is subjected to transitions between different energy levels. An energy level can be described as the energy owned by an electron orbiting around the nucleus along its orbital. When the electron is excited from an external source and acquires sufficient energy, it can change the orbital, and by consequence its energy, to an upper level. As an example, the energy levels for the hydrogen atom are reported in Figure 1.2.
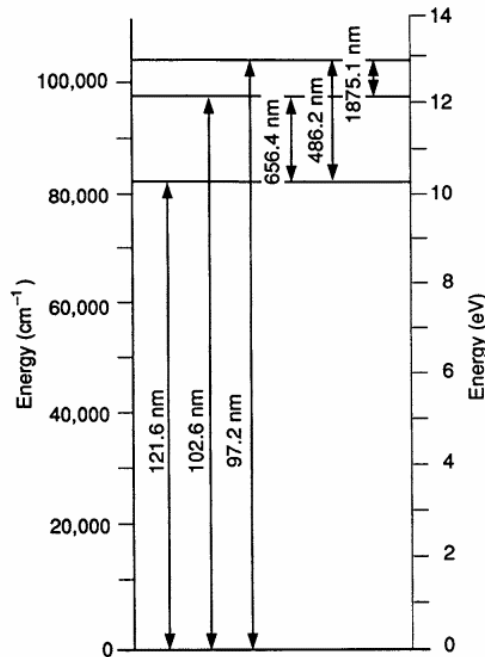
Figure 1.2 - Partial energy level diagram of the hydrogen atom, with wavelengths indicated for several transitions. Energy is indicated both in energy units (electron volts) and in wavenumber units (reciprocal centimetres) [2]

This simplistic view is no more valid if a material (in solid, liquid or gaseous form) is considered instead of atoms or molecules, since it is composed by a vast number of interacting molecules. The higher the density, the stronger the interaction between molecules, which will be more relevant in a condensed material than in a gas [2]. This interaction can lead to energy levels joining in conduction and valence bands or, conversely, keep separate forming narrow energy bands and metastable levels. The latter are fundamental for population inversion (when more electrons are in the excited state rather than the fundamental one) and are typical for transition metal elements and rare earth elements, which for this reason are employed as dopants in LASER field [4].

As described in Figure 1.3, starting from a simple two-level energy system, characterized by energy E_1 and E_2, an electron can be found at the lower energy level if its atom is at the fundamental state. When a transition between the two levels occurs, the atom absorbs or emits a photon which frequency is equal to f=E/h, where E is the delta energy between E_1 and E_2 and h the Planck's constant. If an atom absorbs energy and its electrons go from lower state E_1 to upper state E_2, it comes

to excitation. Conversely, a photon is emitted and the atom comes back to the fundamental state. It is important to remark that in a two-level energy system when an electron moves from lower to upper state by the interaction with a photon, it doesn't maintain its excited state for a long time. Almost immediately after the transition, it will return to the ground state. This behavior is not sufficient for a LASER operation. Indeed, in order to have population inversion, a three- or four-level energy system is required. So, when a lasing material is subjected to an electromagnetic wave, three different radiative processes may take place: absorption, spontaneous and stimulated emission. [5].

In the next paragraphs a description of the three radiation processes is reported.
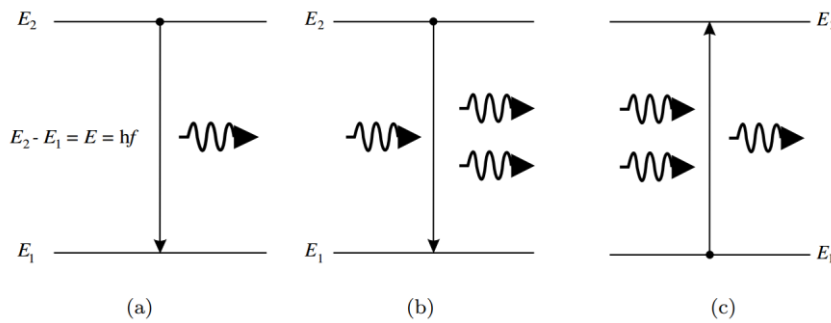
Figure 1.3 - Simple two-level energy system which describes radiative processes. a) spontaneous emission, b) stimulated emission, c) absorption.

1.2.1.1   Absorption

Before reaching the excited state, it is necessary that a determined energy amount is provided to the system by a radiation field. To provide a more detailed description, let's name the population density of the fundamental state N_1 and the one of the excited state N_2. When the radiation with frequency f is applied, the electrons gain energy and move from the lower state to the upper; this process is called absorption and can be mathematically described by Equation 1.3.

$$\left[\frac{dN_2}{dt}\right] = -\left[\frac{dN_1}{dt}\right] = B_{12} * N_1 * \rho(f) \qquad \text{Equation 1.3}$$

where B_{12} refers to the absorption probability per unit spectral energy density and $\rho(f)$ is the average spectral energy density per unit frequency for blackbody radiation. At thermal equilibrium, the absorption rate must equal the sum of the stimulated and spontaneous emission rates.

1.2.1.2   Spontaneous emission

The spontaneous emission, also referred to as fluorescence, is the radiative process previously described typical for two-level energy systems. In accordance with the previous definition of N_1 and N_2, the transition rate from N_2 to N_1 can be formulated as Equation 1.4.

$$\left[\frac{dN_2}{dt}\right] = -\left[\frac{dN_1}{dt}\right] = -A_{21} * N_2$$

<div align="right">**Equation 1.4**</div>

where A_{21} is the spontaneous emission probability. The inverse of A_{21} is τ_{21} called spontaneous emission lifetime, which is the average survival time of the electrons in the excited energy state E_2. The probability that an atom will undergo a spontaneous decay in time is $A_{21}dt$. The mathematical relation between N_2 and average lifetime is given by Equation 1.5.

$$N_2 = N_2^0 * \exp\left(-\frac{t}{\tau_{21}}\right)$$

<div align="right">**Equation 1.5**</div>

Where N_2^0 is the value of N_2 at t=0. If a system is subjected to spontaneous emission, the output radiation won't be characterized by a precise phase or direction and the value of N_2 will rapidly drop in favour of a resettlement in the lower energy level and a consequent increment of N_1.

1.2.1.3   Stimulated emission

Stimulated emission occurs when a photon interacts with a system which is yet in its excited state. The result of the interaction consists of two emitted photons with the same frequency, phase and direction of the input one and the drop of the excited electron from the upper to the lower energy level, as reported in Figure 1.3b. This interaction generates an amplification of the light intensity in the system, which is the origin of the acronym LASER: Light Amplification by Stimulated Emission of Radiation [2]. In contraposition with the absorption process, the stimulated emission is given by Equation 1.6.

$$\left[\frac{dN_2}{dt}\right] = -\left[\frac{dN_1}{dt}\right] = -B_{21} * N_2 * \rho(f)$$

<div align="right">**Equation 1.6**</div>

In this equation, B_{21} represents the stimulated emission probability per unit time and per unit spectral energy density. Comparing Equation 1.6 with Equation 1.4, we can observe that the stimulated emission is the inverse of stimulated absorption. If N_1 is greater than N_2, the probability that an absorption process occurring increases compared to the probability of an emission process, and vice versa. When the light beam goes through a material system with N_1 atom density at level 1 and N_2 atoms density al level 2, if level 2 is higher than level 1, an absorption process occurs, and the light intensity decrement, in z direction, is given by Equation 1.7.

$$I(z) = I(0) * e^{(-\alpha * z)}$$

<div align="right">**Equation 1.7**</div>

where α is the absorption coefficient and is given by Equation 1.8.

$$\alpha = \left(\frac{c^2}{4 * \pi * \tau * f^2}\right) * \left[\frac{\ln 2}{\pi}\right]^{\frac{1}{2}} * \left(\frac{N_1}{\Delta f}\right)$$

<div align="right">**Equation 1.8**</div>

Assuming τ as the fluorescent lifetime of the material, and c as the velocity of light in the material. Amplification by stimulated emission increases the light intensity according to Equation 1.9.

$$I(z) = I(0) * e^{(g * z)}$$

<div align="right">**Equation 1.9**</div>

where g, the gain coefficient, is reported in Equation 1.10.

$$g = \left(\frac{c^2}{4*\pi*\tau*f^2}\right)\left[\frac{\ln 2}{\pi}\right]^{\frac{1}{2}} * \left(\frac{N_2}{\Delta f}\right)$$

<div align="right">**Equation 1.10**</div>

Coefficient α and coefficient g have similar forms, because of absorption and stimulated emission are similar processes, but absorption is the inverse process of stimulated emission speaking of light intensity modification passing by a material, which is given by Equation 1.11.

$$I(z) = I(0*)e^{\left\{\left(\frac{c^2}{4*\pi*\tau*f^2}\right)*\left[\frac{\ln 2}{\pi}\right]^{\frac{1}{2}}*\left(\frac{N_2-N_1}{\Delta f}\right)*z\right\}}$$

<div align="right">**Equation 1.11**</div>

From the previous equation, if N_2 is greater than N_1, the exponential will be positive, so light intensity will increase exponential in z direction, indeed if N_1 is greater than N_2 it will decrease. The atom density condition $N_2 > N_1$ is the physical requirement for laser generation, and it is called "population inversion", otherwise the light intensity will decrease exponentially in z direction. In order to reach the population inversion, a material must have more electrons in a high-lying energy level at which fluorescent emission begin than in the lower-lying energy level at which it ends. However, for a material in thermal equilibrium, the ratio between atoms at higher level and atoms at lowest level is ruled by Equation 1.12.

$$\frac{N_2}{N_1} = e^{\left(\frac{-(E_2-E_1)}{k*T}\right)}$$

<div align="right">**Equation 1.12**</div>

where k is Boltzmann's constant, equal to $1.38*10^{-16}$ erg/deg.

According to Equation 1.12, at thermal equilibrium N_1 is greater than N_2. In order to reach population inversion, the thermal equilibrium must be subverted, suppling energy to the system to rise electrons to higher levels. This process is usually called "pumping." There are many kind of pumping method, like optical pumping or electrons collisions in a gas. In order to achieve a population inversion, a system

which has more than two energy levels must be pumped. As represented in Figure 1.4, laser materials can be represented with a three-level energy system or with a four-level energy system. In a three-level energy system, he fluorescence process ends at the lowest energy level, indeed in a four-level energy system the fluorescence process ends at an intermediate energy level.
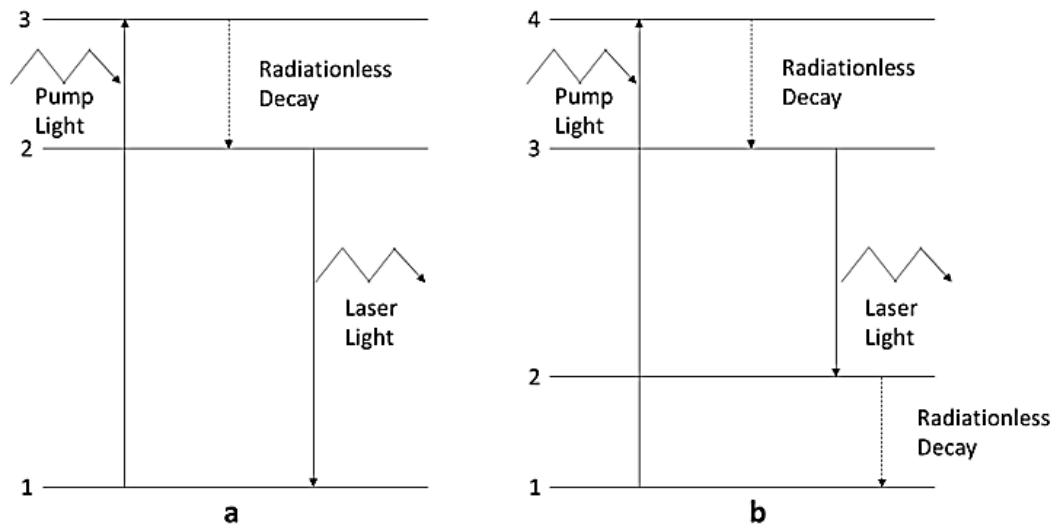
Figure 1.4 – Two different energy level systems. The incident light, when the system is in the higher energy level status, allows the emission of laser light. a. Three-level system, the laser emission brings he system to the lowest energy level b. Four-level system, the laser emission brings the system to an intermediate energy level above the lowest energy level.

In the three-level system, population inversion can be induced by increasing the electrons to highest energy levels with an energetic pumping. Light with a natural frequency $f_3=(E_3-E_1)/h$ is absorbed by material and excites electrons from ground level to the highest one. A consequential radiatonless decay brings the electrons to an intermediate level, with an exothermal process. So, light is emitted with a frequency $f_2=(E_2-E_1)$, and all the electrons drop to the ground energy level. Although stimulated emission is possible in a three-level system, an intense pumping is required, because of more than half of all the electrons must be moved to level 2. A four-level system turns out to be more convenient, since there are two radiatonless transitions, from level 4 to level 3 and for level 2 to ground level, the stimulated emission occurs when the electrons drop from level 3 to level 2 at a frequency $f_3 = (E_3-E_2)/h$, therefore requires a much lower auxiliary energy (pumping). The most common methods of supplying energy to a system to generate population inversion are mainly 3:

- Optical pumping;
- Resonant transfer of energy by collisions with other molecules;
- Excitation by collisions with energetic electrons

1.2.2 Optical pumping

The most used pumping method is the optical pumping, in which the population inversion is generated by supplying energy to the material through a light beam. To achieve the inversion, different light sources are used, such as lamp or semiconductor laser diodes. An example of lasers that use optical pumping are solid-state lasers, such as infrared lasers with active medium Nd: YAG, which generate e laser beam with a frequency of 1064nm. Typical energy level for Nd:YAG are reported in Figure 1.5.
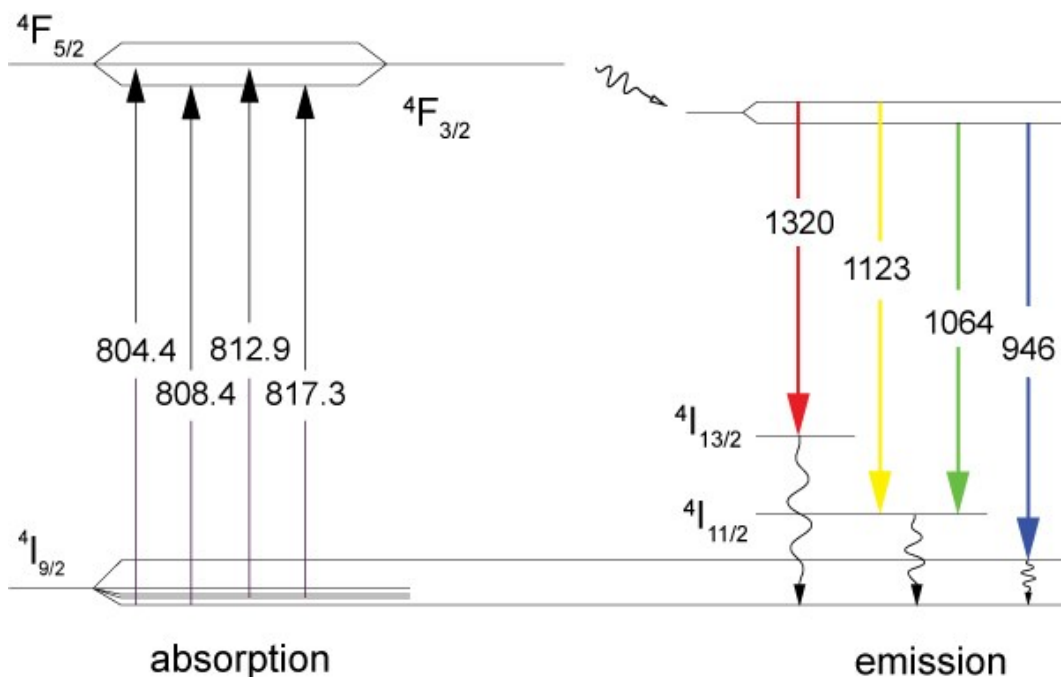
Figure 1.5 - The relevant energy levels of Nd-YAG for optical pumping with laser diodes having wavelengths around 808 nm [6]

About optical pumping, laser diodes are more suitable than lamp, because of their better efficiency, their spatial coherence, because is easier matching their frequency with absorption spectrum of active medium.

1.2.3 Resonant cavity

The resonating cavity or resonator is one of the fundamental elements present in each laser (the structure is based on the Fabry-Pérot model). The stimulated emission process can be greatly amplified if the laser-active medium is placed between two mirrors. Between these two mirrors the photons are reflected in both directions at the speed of light, thus repeatedly crossing the laser-active medium. In this way, a feedback optical amplifier is obtained, a generator capable of generating light waves (Figure 1.6). For the system to work, it is necessary that the distance L between the two opposite mirrors is exactly an integer multiple of a half-length of the wave generated by stimulated emission.

The optical resonator can oscillate on many different "ways". Axial (longitudinal) and non-axial or spatial (transverse) modes are distinguished. In transverse modes the wave phase is no longer homogeneous on the whole surface of the mirror, so there are multiple beams inside the laser beam. The optical oscillator also influences the "reflective" behaviour of the laser beam; in order that this ray can escape from the cavity to pass into free space, one of the two mirrors is in fact made slightly permeable to the corresponding wavelengths. In this way, only those rays that are reflected in a perfectly parallel way leave the laser in the form of coherent light.
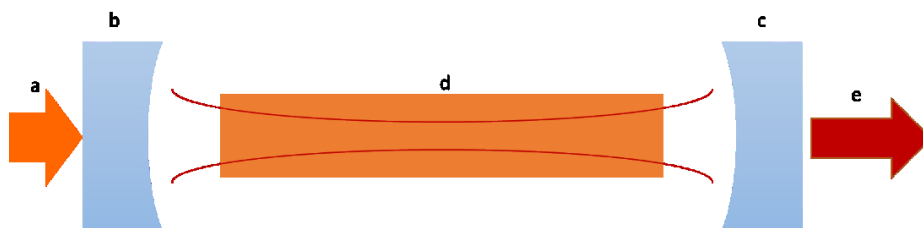
Figure 1.6 - Nd:YAG solid-state laser cavity example. a. Input laser @808nm; b. First mirror, highly transparent to 808nm radiation and highly reflective to 1064nm radiation; c. Second mirror, partially transparent to 1064 nm radiation; d. Nd:YAG crystal, which absorbs 808nm radiation and emits 1064nm radiation; e. Output laser @1064nm

1.2.4 Q-Switched Lasers

The Q-switching is a practice used for the emission of pulsed laser beams, exploiting the losses inside a resonant cavity [7]. This technique allows to obtain

pulses in the order of the nanosecond, which have a high peak power combined with a high pulse energy. If the Q-switch element is held open, the resonant cavity has high losses, preventing the formation of the laser beam. In this way, the active medium is charged with the energy coming from the pumping source (Figure 1.7). Then, the losses are suddenly reduced, so that the laser radiation grows suddenly. Once the intracavity energy has reached the saturation energy, the gain becomes saturated, and the peak of power is reached.

The pulse duration typical of this technique is in the region of nanoseconds, the energy in the region of millijoules, the peak power reaches the kilowatts, while the repetition frequency of the pulses is typically between 1 and 100 kHz.

There are mainly two types of Q-switch elements:

- Active Q-switches, in which the losses are modulated through an active element, usually acoustic-optical or electro-optic, controlled by a trigger signal. There are also mechanical active q-switches, such as rotating mirrors or mirrors mounted on linear axes, which can replace the second mirror of the resonant cavity.
- Passive Q-switches, in which the losses are modulated through saturable absorbers. Pulse energy and pulse duration are fixed, while pulse frequency can be varied by pump power modulation.

Compared to active Q-switching, passive Q-switching is a simpler and cheaper technique and is suitable for very high pulse repetition rates. However, the energy of the individual pulsation is generally lower.
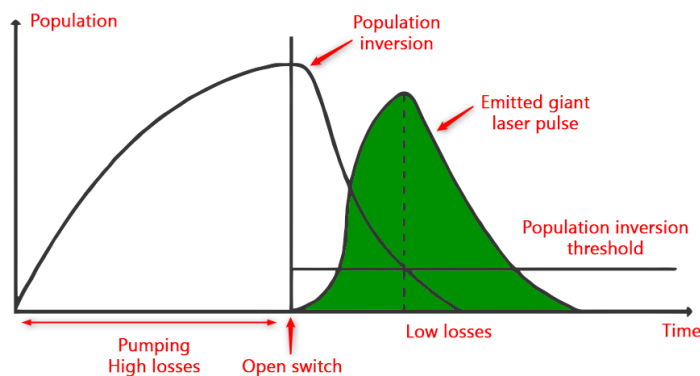
Figure 1.7 - The scheme of the giant laser pulse production in the Q-switched regime

1.2.5 Mode-Locking Lasers

A technique that generates laser pulses in the pico- and femtosecond region is the Mode-Locking [8]. With this technique, it is possible to trap the laser pulse, by making it circulate inside the resonator. Whenever the second mirror that makes up the cavity is struck by the laser impulse, a part of its energy is emitted, creating a train of impulses. The round-trip of the resonator is the parameter that determines the pulse repetition rate, with values typically between 50 and 500MHz, with peaks of 100GHz. Pulse duration typically occurs between tens of femtoseconds and tens of picoseconds. The limit of Mode-Locking lasers is that the pulse energy is limited, because of the high pulse frequency, with values in the picojoule region. It is possible to analyze this mode both in the time domain and in the frequency domain. There are several types of mode-locking techniques:

- Active Mode-Locking, obtained by using an active modulator, usually of an electro-optical type, that is able to synchronize the losses of the resonant cavity with the round-trips. This element is placed near one of the two mirrors that make up the cavity;
- Passive Mode-Locking, obtained by means of a saturable absorber, and allows to obtain shorter pulses of the active mode.

1.2.5.1   Amplitude modulation Mode Locking

If one considers the mode-locking in the frequency domain, if a mode has optical frequency, ν and is amplitude-modulated at a frequency νm, the resulting signal has sidebands at optical frequencies $\nu-\nu m$ and $\nu+\nu m$. In the case the modulator is driven at the same frequency as the cavity-mode spacing $\Delta\nu$, then these sidebands correspond to the two cavity modes adjacent to the original mode. Since the sidebands are driven in-phase, the central mode and the adjacent modes will be phase-locked together. Further operation of the modulator on the sidebands produces phase-locking of the $\nu-2\nu m$ and $\nu+2\nu m$ modes, and so on until all modes in the gain bandwidth are locked. What we understand it that this amplitude modulation can be considered as a frequency modulation mode-locking. The sideband frequencies are generated using a modulator device based on the electro-optical effect. When this device is placed in the laser cavity and it is driven with an electrical signal, induces a small, sinusoidal varying frequency shift in the light passing through it. If the modulation frequency is matched to the roundtrip time of

the cavity, then some light in the cavity sees repeated up-shifts in frequency, and some repeated downshifts. After many repetitions, the up-shifted and down-shifted light is swept out of the gain bandwidth of the laser. The only light which is unaffected is that which passes through the modulator when the induced frequency shift is zero, which forms a narrow pulse of light. It is instructive to consider the synthesis of a periodic pulse train by superposition of sinusoidal oscillations (Figure 1.8) with equally spaced frequencies, corresponding to different axial resonator modes in a mode-locked laser. The larger the number of frequency components involved, the shorter can be the duration of the generated pulses.
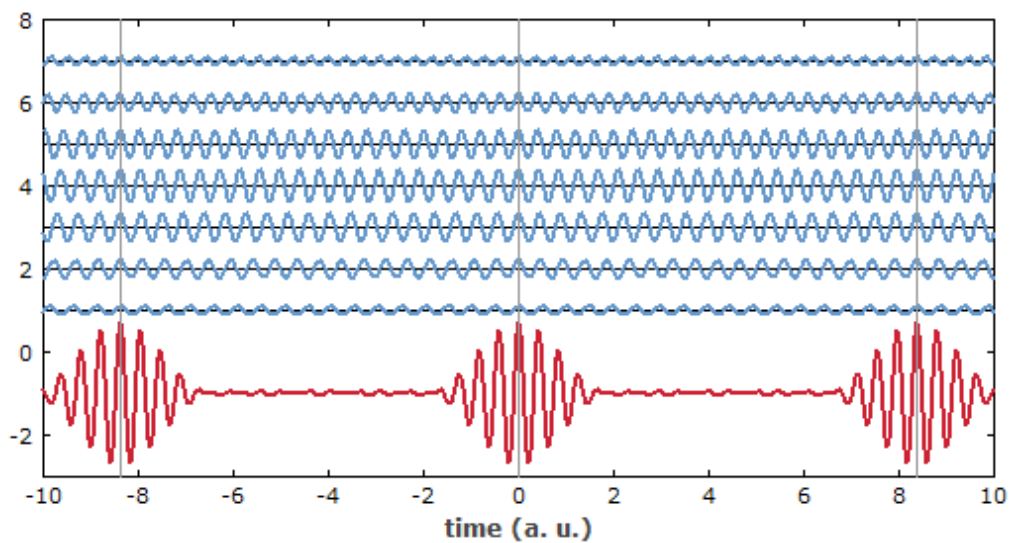
Figure 1.8 - Synthesis of a periodic pulse train (red curve) by adding seven oscillations with slightly different frequencies (blue curves). The vertical lines indicate points in time where all the oscillations add up in phase[9].

An important aspect is that there must be a fixed phase relationship between these modes. This is illustrated in Figure 1.9: the blue curve shows a pulse train with a fixed phase relationship (phase-locked), so that at regular temporal positions (e.g. at $t = 0$) the electric fields of all frequency components add up to a maximum of the total field strength. The red curve shows the electric field for the same strength of all frequency components, but with random relative phases.
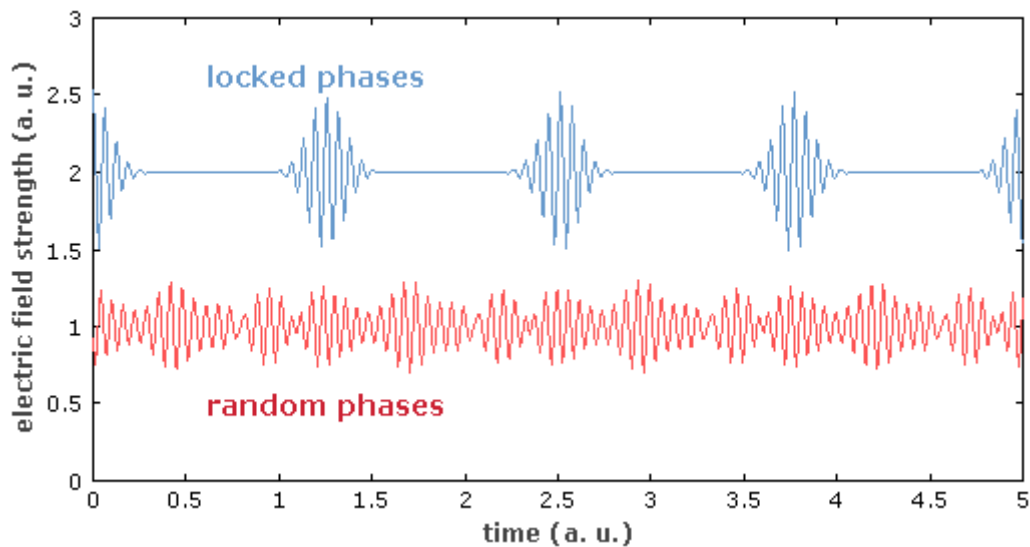
Figure 1.9 - Temporal evolution of the intracavity field in a laser, once with a fixed phase relationship between the modes (mode-locked state), once with random phases[9].

1.2.5.2 Frequency modulation Mode Locking

Side bands can also be generated by a phase modulator instead of an amplitude modulator. This technique is called *FM mode locking* (FM = frequency modulation), although the term *phase modulation mode locking* would seem to be more appropriate. However, the generated sidebands are out of phase with the carrier, which leads to a chirp on the steady state pulse. A chirp is a signal in which the frequency increases (up-chirp) or decreases (down-chirp) with time (Figure 1.10).
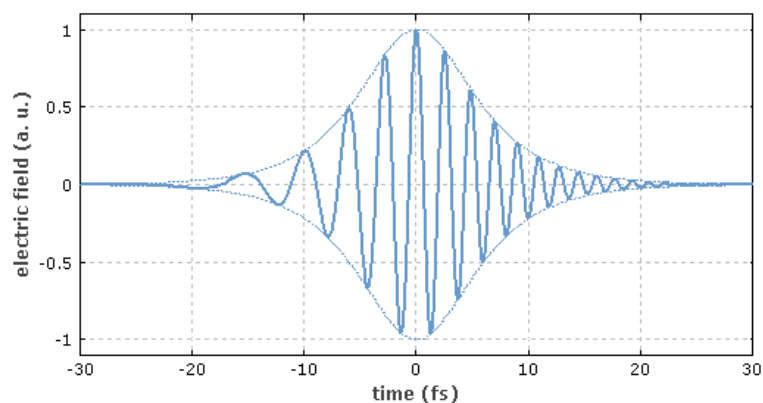
Figure 1.10 - Example of chirp signal [10]

The sequence represented in Figure 1.11 show the generation of a chirped pulse related to the phase shift. When the shift between each mode is 0 then the amplitude of the pulse is the highest.
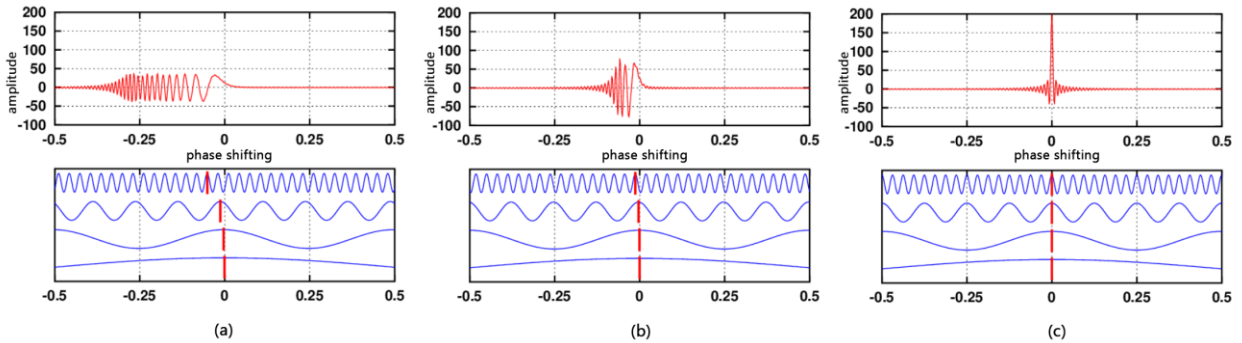
Figure 1.11 - Chirped pulse generation by phase shifting of four sine waves at different frequency; Time sequence start from image (a) and finish with image (c). The red line in the waves give the relative phase shift to the other sine waves. When the phase shifting is null the red signal is at the maximum amplitude [11]**.**

1.3 Beam Quality

Any rotational symmetrical laser beam may be characterized by the following three parameters (see Figure 1.12).

(1) Beam waist position z_0,
(2) Radius of the beam waist w_0,
(3) Far-field divergence angle Θ_0.
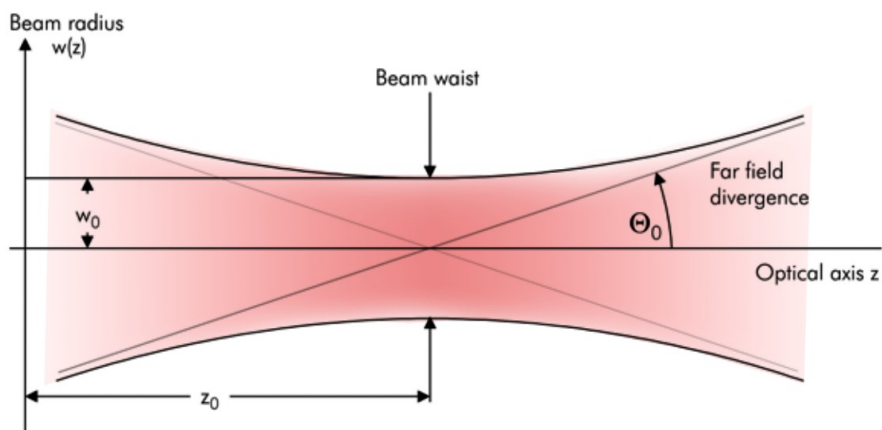
Figure 1.12 - Laser beam in the focus point

Various characteristic numbers are used to describe the beam quality of a laser beam: K, M² as well as the beam parameter product (BPP). These characteristic numbers are directly converted into each other by simple calculations. The beam parameter product is derived from the above-mentioned parameters used to describe rotation-symmetrical laser beams. The beam parameter product is the product of the w_0 and Θ_0 values and remains constant over the entire laser beam region. Changing the diameter; for instance, by installing lenses and/or telescopes, will always influence the divergence. Thus, the beam parameter product is a measure of focusability. Only the use of optical systems with aberration or aperture effects may influence the beam parameter product along the external optical path. The K and M2 values are a standardized measure of the beam parameter product and pertain to the physical limits of a laser beam and it's focusability. The full context is reported in Equation 1.13.

$$K = \frac{1}{M^2} = \frac{\lambda}{\pi} * \frac{1}{w_0 * \theta_0}$$

Equation 1.13

Both characteristic numbers are commonly used to characterize lasers whose beam quality is close to ideal; i.e., with K values in the range of 0.1 to 1 resp. M² values between 1 and 10. The beam parameter product ($w_0*\Theta_0$) is frequently utilized instead of K and M² to characterize lasers whose beam quality is relatively far from the ideal; i.e., with K values considerably below 0.1 resp. M² larger than 10. The three mentioned characteristic numbers may be used to characterize all lasers with rotation symmetrical laser beams. Figure 1.13 shows typical areas of laser application in relation to the beam parameter product and the laser power.
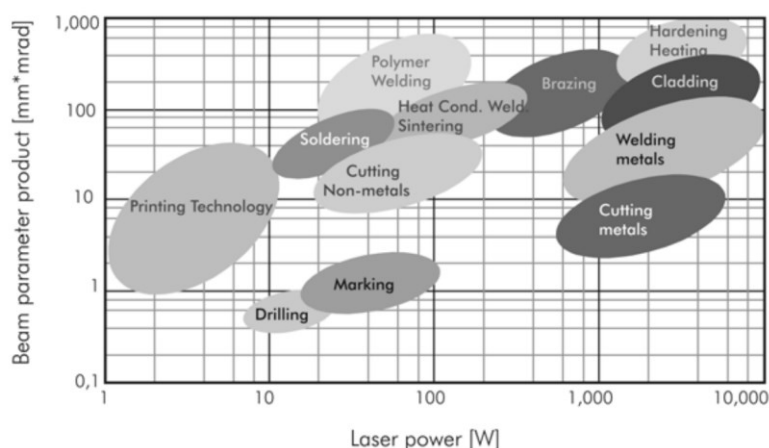
Figure 1.13 – Map of different laser applications, related to beam parameter product (on the vertical axis) and laser power (on the horizontal axis) [1]

Any laser beam may be focused; i.e., it may be reduced to a tiny beam diameter by using appropriate optical elements, such as curved mirrors or lenses with a focal distance f (see Figure 1.14). The focusing radius r_{foc} of a symmetrical laser beam with a wavelength λ may be calculated according to the Equation 1.14, as long as the radius r of the laser beam on the mirror, the far-field angle of divergence Θ_0, and the beam characteristic number K are known.

$$r_{foc} = \frac{f * \lambda}{r * \pi * K}$$

Equation 1.14
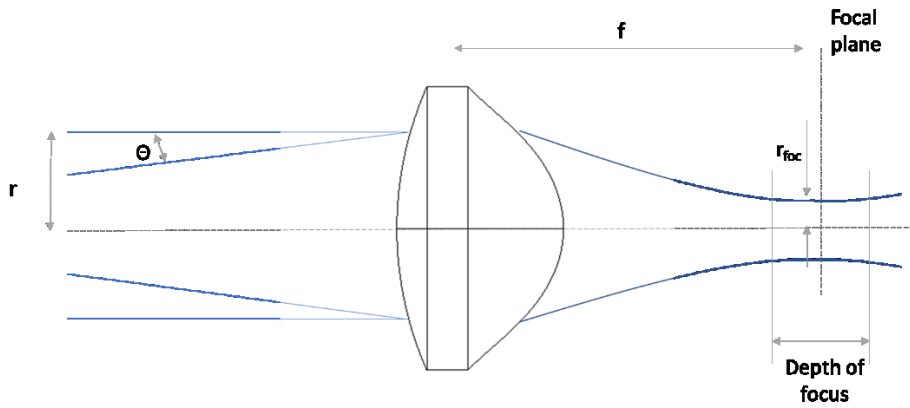
Figure 1.14 – A representation of a general focusing process of a divergent beam through an optical lens.

Equation 1.15 shows that an ideal laser beam (K = $1/M^2$ = 1) with an ideal optical element at a focal distance f may be focused on a very tiny spot radius:

$$r_{foc}^{ideal} = \frac{f * \lambda}{r * \pi}$$

Equation 1.15

The Rayleigh length distance is the distance from the focus at which the cross-sectional area of the laser beam has doubled. The depth of focus, by definition, is twice as long as the Rayleigh distance. This is quantified in Equation 1.16:

$$z_{Rayleigh} = \frac{f^2 * \lambda}{2 * r^2 * \pi * K}$$

Equation 1.16

Chapter 2

2   Fundamentals of Polymers

2.1 Introduction

A polymer is defined as "a substance composed of molecules which have long sequences of one or more species of atoms or groups of atoms linked to each other by primary, usually covalent, bonds" [12]. The repeat units are called monomers and they can undergo modifications (e.g. loss of chemical groups) during the formation of polymers chain, a process known as 'polymerization'.

The widespread use of polymer in ordinary life [13] is motivated by the huge variability and range of properties which characterize both synthetic and natural polymers [14]. Nylon® and Plexiglass ® are two common examples of synthetic polymers, while the most commonly known natural one are DNA and proteins.

Further classification divides polymers into two categories: organic and inorganic polymers. The first is about polymer which chain is composed only by carbon and hydrogen atoms (e.g. polyethylene, polypropylene) or carbon and hydrogen with other elements (e.g. polyvinyl chloride has a chlorine attached to the carbon backbone). When an element different from carbon is included in the carbon backbone, it comes to organic polymers like Nylon®. On the contrary, inorganic polymers have the main chain composed by elements other than carbon, for example silicon or phosphorous [15].

2.1 The structure of polymers

Based on the spatial arrangement of chains, it is said that polymer have a linear or non-linear structure as reported in Figure 2.1.
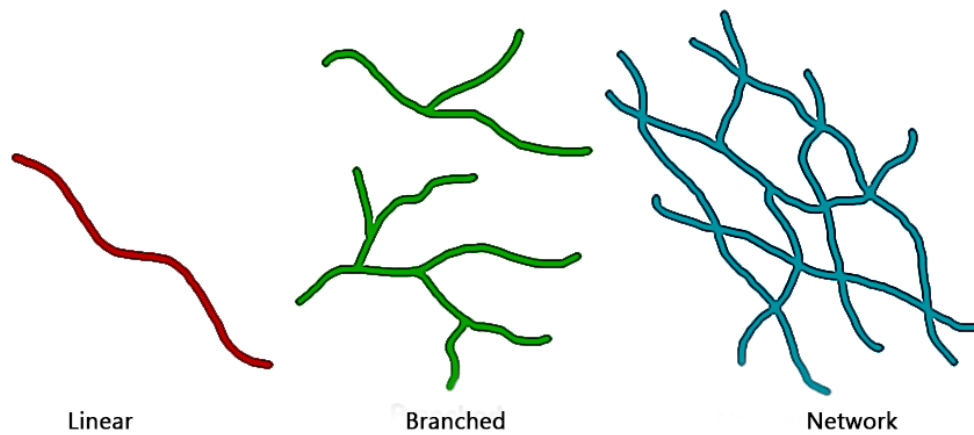
Figure 2.1 - Polymers structures

A linear structure can be defined as a chain with only two extremities. Otherwise, branched or network polymers are considered. The first are composed by one main chain, often called backbone, with side chains anchored with covalent bonds at junction points. These polymers are identified by the number and size of branches. Differently, network polymers have chain all connected one another and are characterized by the so-called degree of crosslinking, which is nothing else than the number of junction points per unit volume.

Since this thesis work is about additive manufacturing, a classification which has not been reported yet is now proposed. It is based on the structure difference and is strictly related to the rapid prototyping technologies employed to process such materials. Three main categories can be listed: thermoplastic polymers, rubbers and thermosets. Thermoplastics are linear or branched polymers; upon heating, they can be molded or extruded and on cooling they can crystallize or produce non-crystalline structures depending on the degree of branching and regular repetition of the constituent molecules. At room temperature they are characterized by a plastic mechanical behavior. Rubbers, differently from thermoplastics, show elastomeric properties due to their lightly crosslinked network which allows for relative movement among the flexible chains. However, the presence of this network forbids melting when heated and organizes as a crystalline or amorphous structure when cooled. Finally, thermosets are similar to rubbers for their network structure, but the difference is the high degree of crosslinking which provides mechanical stability. If they are subjected to increasing temperature, they degrade rather than melt, a typical behavior for photo-reticulated resins.

2.2 Molecular arrangement of polymers

Considering the units of a polymer chain, homopolymers or copolymers can be found. The first are the repetition of the same monomeric unit and are designated as $[A]_n$ where 'A' is the monomer nomenclature and 'n' is the number of units. The latter comprise chains in which more than one type of monomer are involved. By varying the position of the repeating units, the copolymers can be classified as: alternating, periodic, statistical, block, grafted. Figure 2.2 shows a schematic description of each polymer. As the name explains, alternating copolymers (Fig. 18.2) are composed by alternating monomers and are named as $[AB]_n$. Periodic copolymers are quite different since the monomers appear with a different periodicity as $[A_nB_m]$ where 'n' is different from 'm'. In a statistical copolymer, the presence of a monomer residue at a particular point in the chain is not related to the type of surrounding monomers; this is the reason why statistical copolymers are named also 'random copolymers' (Fig. 18.3). Block copolymers are the result of the bond between homopolymers: if two or three different chemical species are present, it comes to di-block or tri-block copolymers. Finally, grafted copolymers show side chains which can be different from backbone chain.

Figure 2.2 - Arrangement of copolymers repeating unit: (18.1) homopolymer (18.2) alternating copolymers (18.3) random copolymers (18.4) Block copolymers (18.5) grafted copolymers

2.3 Polymers synthesis

The term 'polymerization' is often imprecisely used to identify the process of monomer combination to obtain more or less organized structures with the desired mechanical and chemical properties. Indeed, the description of polymerization processes is surely more complex and should be divided in at least two classes: condensation and addition polymerization.

2.3.1 Condensation polymerization

Condensation polymerization is also known as step-growth polymerization and is typical for different monomers which react together releasing a small molecule like water. As the name explains, step-growth polymerization involves two main phases: (i) two monomers react and produce an oligomer and (ii) the oligomers join together in a longer chain. Usually no specific initiation step is required, so any pair of molecules, if proper, can react together.

More in detail, a condensation polymerization occurs when an organic base (e.g. alcohol or amine) and an organic acid (e.g. carboxylic acid or acid chloride) join together releasing a molecule of water. An example is reported about the condensation between acetic acid and ethyl alcohol giving ethyl acetate and a molecule of water (Equation 2.1).

$$CH_3COOH + C_2H_5OH \rightarrow CH_3COOC_2H_5 + H_2O$$
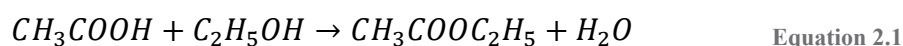
<div align="right">Equation 2.1</div>

More in general, the reaction can be written as explained in Equation 2.2.

$$RNH_2 + HOOCR' \rightarrow RNHCOR' + H_2O$$

<div align="right">Equation 2.2</div>
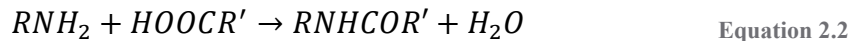
Where R and R' generic chemical groups. Differently from the previous condensation example, for an efficient polymerization it is important that the first reaction product has a reactive site in order to go on with the chain growth.

The reaction can be written again in a general form as visible in Equation 2.3. A diacid monomer react with a diol monomer to obtain a Dimer.

$$HOOC - R_1 - COOH + HO - R_2 - O$$
$$\rightarrow HOOC - R_1 - COO - R_2 - OH + H_2O$$
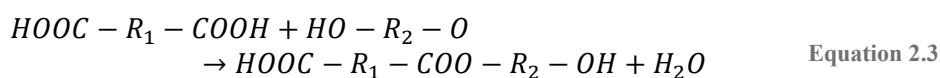
<div align="right">Equation 2.3</div>

R1 and R2 are generic chemical groups. As Equation 2.3 shows, the reaction product has at the extremities two reactive groups: the acid group (COOH) and the hydroxyl group (OH). These reactive groups are referred to as 'functionalities' and are of primary importance for condensation polymerization. For step-growth reaction it is necessary to have at least bifunctional groups; if more than two reactive

sites are present on an oligomer, a network polymer rather than a linear one will be produced.

2.3.2 Addition polymerization

The addition polymerization is also called polyaddition or chain-growth polymerization. It involves monomers with double or triple bonds or, as an alternative, a monomer with double bonds and one with groups which can react with the double bond. This polymerization process is characterized by three main steps: (i) the initiation, (ii) propagation and (iii) termination.

During the initiation step, an initiator is added to the monomer blend with the aim to open the double bond and create an activated molecule, also known as reactive intermediate or active center. In the propagation step other monomers are bonded to the intermediate, the active center is moved to a chain extremity and the process goes on even up to the addition of tens of thousands of molecular units. Termination occurs when a chain-terminating reaction takes place. Propagation is often more probable than termination, so macromolecules composed by thousand units can grow.

Depending on the nature of the active center, two different reactions can be distinguished: radical or ionic polyaddition.

2.3.2.1   Ionic polyaddition

When the active center is an ion (positively or negatively charged), ionic polymerization occurs. It comes to cationic polyaddition if the ions are positively charged or anionic polymerization if negatively charged ions are considered as reactive intermediate.

The detailed mechanisms depend upon the type of initiator, monomer and solvent employed. When the chain carriers are ionic the addition reactions are often rapid, take place at low temperatures and are difficult to reproduce. Ionic polymerization systems have been developed because some monomers which contain double bonds cannot be polymerized using free-radical initiators; the chemical factors which control whether or not a particular monomer can be polymerized using cationic or anionic initiators are beyond the scope of this thesis. In general, ionic initiators are only able to polymerize certain monomers (e.g. olefins and heterocyclic monomers

for cationic polyaddiction and vinyl monomers for anionic polymerization), while free radicals are less selective and can polymerize most types of monomers.

2.3.2.2   Free radical polymerization

Free radicals are extremely reactive species with an unpaired electron able to react with monomers containing a double bond. This interaction leads to the creation of an active center which propagates by the addiction of other monomers until a macromolecular chain is grown.

Once the free radicals have been formed, the next stage of the initiation process is the formation of an active center or chain carrier. If the free radical is denoted by R· and the monomer molecule as M, then the reaction is simply, as visible in Equation 2.4

$$R \cdot + M \rightarrow RM_1 \cdot$$

<div align="right">**Equation 2.4**</div>

Chain propagation takes place by the rapid addition of monomer molecules to the growing chain (Equation 2.5):

$$RM_1 \cdot + M \rightarrow RM_2 \cdot$$

<div align="right">**Equation 2.5**</div>

and this can be written, in general as in Equation 2.6, ignoring the radical fragments as

$$M_i \cdot + M \rightarrow M_{i+1} \cdot$$

<div align="right">**Equation 2.6**</div>

Free radicals are particularly reactive species and there are several ways in which the growing chains can react to form inert covalently bonded polymer molecules. The most important mechanisms of termination are when two growing chains interact with each other and become mutually terminated by one of two specific reactions. One of these reactions is combination where the two growing chains join together to form a single polymer molecule (Equation 2.7).

$$\cdots CH_2 - CH \cdot \ + \ \cdot HC - CH_2 \cdots \ \rightarrow \ \cdots CH_2 - CH \ + \ HC - H_2 \cdots$$
$$\qquad\quad \overset{|}{X} \qquad\quad \overset{|}{X} \qquad\qquad\qquad\quad \overset{|}{X} \qquad\quad \overset{|}{X}$$
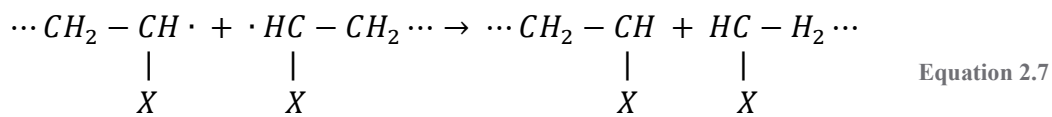
Equation 2.7

The reaction can be written in general as follows in Equation 2.8:

$$RM_i \cdot + \cdot M_n R \rightarrow RM_i M_n R$$

Equation 2.8

Alternatively, a hydrogen atom can be transferred from one chain to the other in a reaction known as disproportionation, visible in Equation 2.9.

$$\cdots CH_2 - CH \cdot \ + \ \cdot HC - CH_2 \cdots \ \rightarrow \ \cdots CH_2 - CH_2 \ + \ HC = CH \cdots$$
$$\qquad\quad \overset{|}{X} \qquad\quad \overset{|}{X} \qquad\qquad\qquad\quad \overset{|}{X} \qquad\quad \overset{|}{X}$$
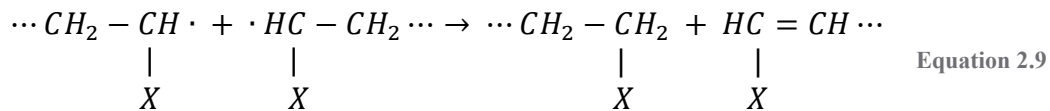
Equation 2.9

and the general form is written in Equation 2.10:

$$RM_i \cdot + \cdot M_n R \rightarrow RM_i + M_n R$$

Equation 2.10

A radical initiator is effective when it is able to break down into radicals which are stable long enough to react with a monomer molecule and form an active center. Initiators are normally required to form radicals in a controlled way usually by the application of heat or electromagnetic radiation or during a chemical reaction as described below. Free radicals may be readily produced by thermal decomposition, photolysis and in some cases by redox reactions. An example of thermal decomposition is the reaction of benzoyl peroxide ($C_{14}H_{10}O_4$) at 60°C in a benzene solution visible in Equation 2.11. $C_{14}H_{10}O_4$ breaks down into benzoyloxy radicals which in turn break down into phenyl radicals and carbon dioxide.

Equation 2.11
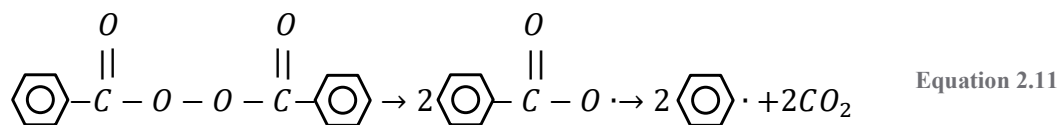
Photolysis gives better control over the production of radicals since the reaction can take place at relatively low temperatures and can be stopped by the removal of the light source. The initiator Azobisisobutyronitrile (AIBN) breaks down into

cyanopropyl radicals and nitrogen at ambient temperature under the action of ultraviolet radiation (Equation 2.12).

$$(CH_3)_2 - C - N = N - C - (CH_3)_2 \rightarrow 2(CH_3)_2 - C \cdot + N_2$$

$$\underset{CN}{|} \qquad \underset{CN}{|} \qquad \underset{CN}{|}$$

Equation 2.12
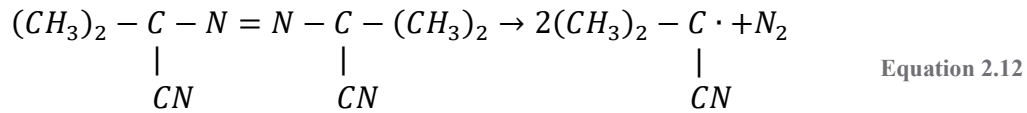
The reaction between hydrogen peroxide and the ferrous ion produces ferric ions and hydroxyl radicals in solution. Radicals produced by redox reaction are particularly useful for the initiation of polymerization at low temperatures or for emulsion polymerization.

$$F_e^{2+} + HOOH \rightarrow F_e^{3+} + HO \cdot + OH^-$$
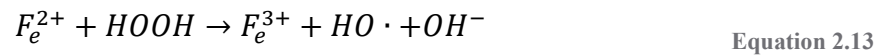
Equation 2.13

In Equation 2.13 the polymerization reactions just described.

2.4 Photopolymerization

Photopolymerization is a branch of photochemistry which deals with light absorption by matter or, more purposely, by molecules. In this field, light is considered not merely a catalyst but a reagent able to excite molecules and allow the crossing of the activation energy thresholds for chemical reactions to occur. Photopolymerization is a widely used technology, used in applications ranging from imaging to biomedical uses. Photoresists are often deposited on a surface and are designed to change properties upon irradiation of light, as visible in Figure 2.3. These changes either polymerize the liquid oligomers into insoluble cross-linked network polymers or decompose the already solid polymers into liquid products. Polymers that form networks during photopolymerization are referred to as negative resist. Conversely, polymers that decompose during photopolymerization are referred to as positive resists. Both positive and negative resists have found many applications including the design and production of micro fabricated chips. The ability to pattern the resist using a focused light source has driven the field of photolithography.
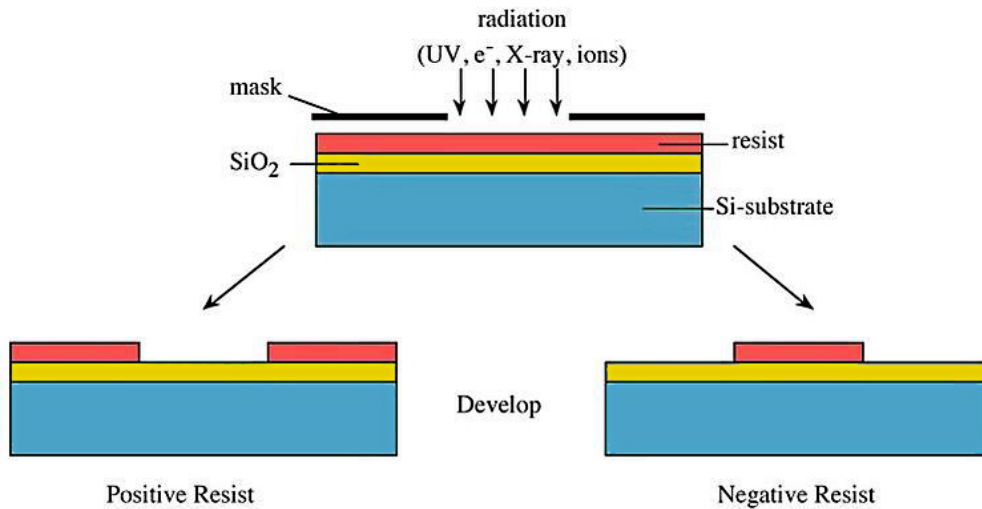
Figure 2.3 – A comparison of positive and negative photoresist

Many natural and synthetic processes such as photosynthesis, photography, and photopolymerization are examples of photochemistry in action [16]. A photopolymer, also called photo-resin, is a polymer that chemically reacts when exposed to ultraviolet of visible light (in most of the cases). Indeed, when oligomers or monomers are exposed to light, they cross-link growing a thermoset network polymer in a process commonly named 'curing'. To be precise, most monomers or oligomers are not directly activated by light; in this case, a photo initiator is required. Similar to the initiators reported in 2.4.2.1 and 2.4.2.2, photoinitiators are able to decompose into reactive species if exposed to light and, by consequence, begin polymerization with the oligomers. In this case, it is possible to have both free radical and ionic initiators which are added to the oligomer and monomer blend in small quantities. When speaking about ionic polymerization, the starting blend can be doped with either anionic or cationic photoinitiators that will initiate the reaction only when radiated by light [17], even if cationic initiators are more investigated than anionic ones. Examples of cationic initiators are: onium salts, organometallic compounds and pyridinium salts.

One of the drawbacks of the initiators used for photopolymerization is that they tend to absorb in the short UV region [18]. For this reason, photosensitizers, or chromophores, that absorb in a much longer wavelength region can be employed to excite the photoinitiators through an energy transfer.

In the free radical mechanism of radiation curable systems, light absorbed by a photoinitiator generates free-radicals which induce cross-linking reactions of a

mixture of functionalized oligomers and monomers to generate the cured film[19]. There are two types of free-radical photoinitiators: Type I and Type II photoinitiators. The first case is a one-component system where two radicals are generated by cleavage and the second one is a two-component system where the radical is generated through abstraction of a hydrogen atom from a donor compound (also called co-initiator),. Examples of each type of free-radical photoinitiator are shown in Figure 2.4 and Figure 2.5.
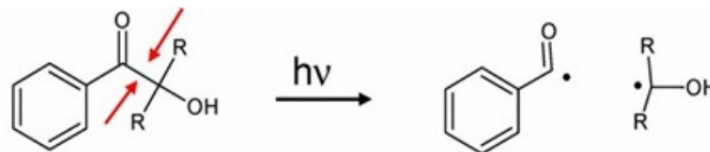
Figure 2.4 – Free radical generation with a Type I photoinitiator hydroxyacetophenone (HAP). The highlighted bond undergoes homolytic cleavage upon the absorption of UV light. HAP's usually absorb shorter wavelength UV-A radiation (300-350nm) [20]
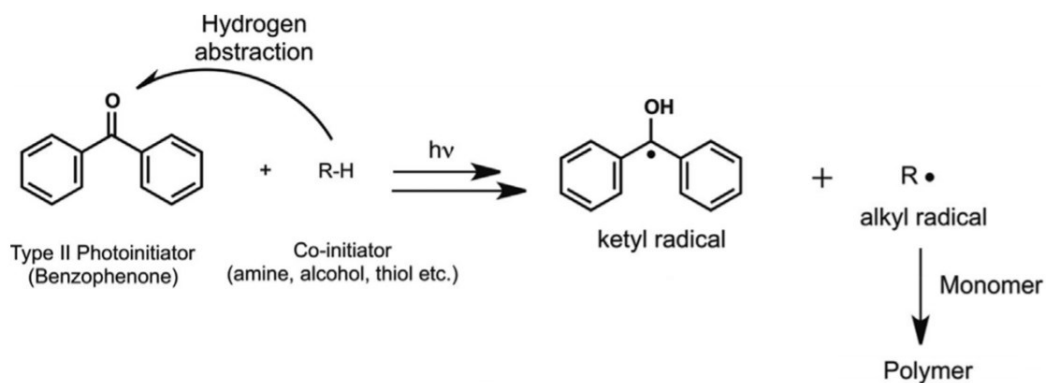
Figure 2.5 – Free radical generation with a Type II photoinitiator Benzophenone with a co-initiator and termination reactions of ketyl radicals [21]

Photocurable materials that form through the free-radical mechanism undergo chain-growth polymerization. In general only the initiation step differs from that of the ordinary thermal polymerization of the same monomer; subsequent propagation, termination and chain transfer steps are unchanged [22]. A scheme reassuming the process, explained in detail at point 2.4.2.2, is shown below in the equation sequence starting from Equation 2.14 to Equation 2.17.

Initiation

$$Initiator + h_v \rightarrow R \cdot$$
$$R \cdot + M \rightarrow RM \cdot$$

Propagation

$$RM \cdot + M_n \rightarrow RM_{n+1} \cdot$$

Termination

Combination

$$RM_n \cdot + \cdot M_m R \rightarrow RM_n M_m R$$

Disproportionation

$$RM_n \cdot + \cdot M_m R \rightarrow RM_n + M_m R$$
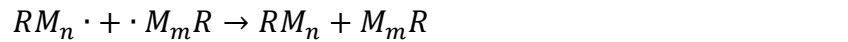
More attention was payed on photopolymerization since this thesis work deals with stereolithography (SL), a 3D printing technique strongly related to the behavior of polymers upon irradiation. Even if it will be discussed in the next chapter, SL can be briefly defined as a process for converting liquid blends (oligomers and monomers) into solid polymeric objects. Monomers commonly used include multifunctional acrylates and methacrylates and epoxies, which can also be used in combination. Free-radical and cationic polymerizations composed of both epoxide and acrylate monomers have been employed, gaining the high rate of polymerization from the acryilic monomer, and better mechanical properties from the epoxy matrix[23].

2.4.1 Two Photon Polymerization

The polymerization mechanisms described so far are the result of a material linear response to an applied optical field. But, if ultrafast laser systems are considered, more than one photon may interact with matter at one time, thus determining non-linear responses.
An attractive three-dimensional (3D) micro- and nanofabrication method using ultrafast laser pulses is the two-photon polymerization (2PP) technique of photosensitive materials. Since a proportional relationship between n-photon absorption and photon flux density exists, high-flux sources are required for 2PP to be performed. Multiphoton absorption was demonstrated with the help of lasers, since much higher intensities could be achieved if compared with other light sources. 2PP is strictly related to two-photon-absorption (2PA): when an atom absorbs two or more photons simultaneously, the electron transition to the states that can't be reached with a single photon absorption is allowed. Actually, two

photons are not absorbed by the atom exactly at the same time: the first one gives the energy to reach a virtual state with femtosecond lifetime (dotted in Figure 2.6) while the second one accomplishes the transition (energy level S2 is reached). The main advantages of multiphoton absorption are high spatial resolution and the ability to selectively excite specific molecules.
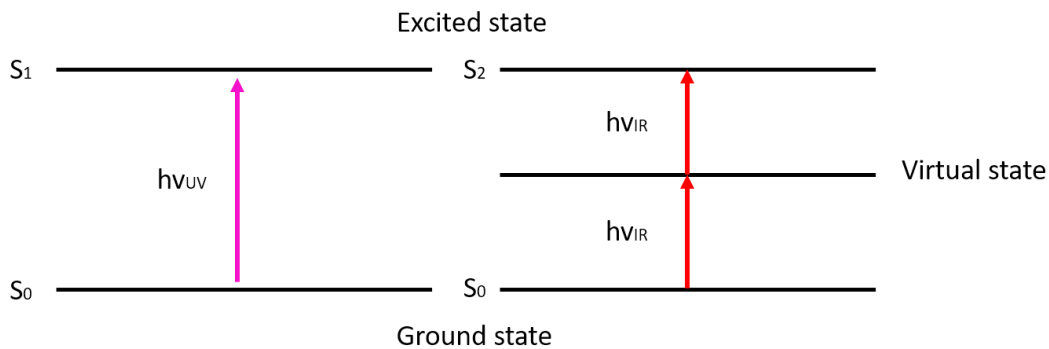
Figure 2.6 - Single photon absorption and two photon absorption

In the 2PA process applied on photopolymers, femtosecond (fs) laser pulses initiate 2PP polymerization in an extremely localized focal volume, as visible in Figure 2.7.This results in 3D micro and nanoscale structures [24] with current resolution down to 100 nm. In stereolithography instead, a UV laser, applied to scan the surface of the photosensitive material, builds 2D patterns of polymerized material. The UV laser radiation induces photopolymerization through single photon absorption at the surface of the material. Therefore, with stereolithography it is only possible to fabricate 3D structures using a layer by layer approach. Since photosensitive materials are usually transparent in the infrared and highly absorptive in the UV range, one can initiate two photon polymerization with IR laser pulses within the small volume of the material by precisely focused near infrared femtosecond laser pulses. Figure 2.7 illustrates the comparison between single photon and two photon activated processing. In the first case, the liquid blend sensitive to UV radiation (λ_{UV}) is polymerized on the previously solidified object where the laser spot interacts with the material. In the second case, a penetrating infrared light of approximately double wavelength (λ_{IR}) is employed to polymerize the material inside a volume with a tightly small focus. Precondition is that the laser source has a light intensity big enough to start 2PP.
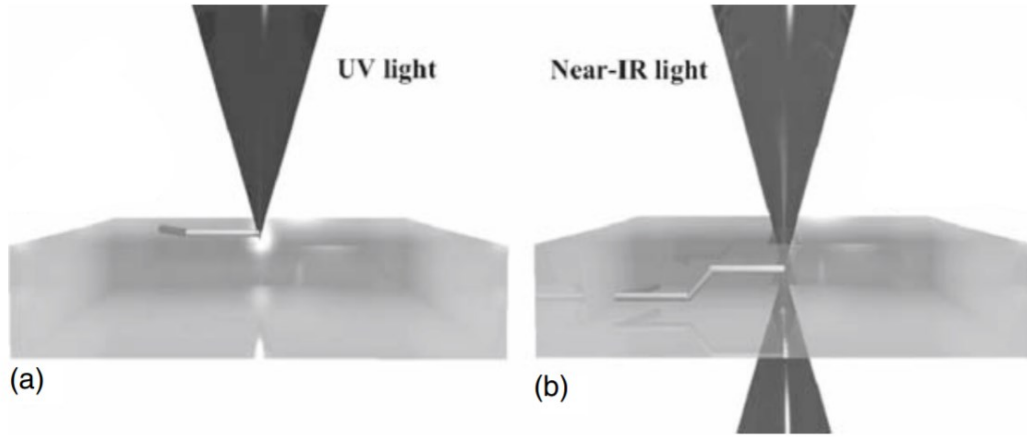
Figure 2.7 - Polymerization differences between single and two photon absorption. In the single photon absorption light is absorbed only on the surface of the photosensitive material allowing construction of two-dimensional patterns; (b) With two-photon absorption using near-infrared light all chemical reactions are confined in the focal volume, and the rest of the laser radiation passes through the material without interaction. [25]

In the 2PP, the resolution is determined by the size of a voxel (volumetric pixel) which is the minimum polymerizable feature. Voxel dimension is dependent on laser power and exposure time, and can be theoretically estimated as shown in Equation 2.18 and Equation 2.19 [26]

$$d(P_t, t, NA) = \frac{\lambda}{\pi\tan(\sin^{-1}(NA/n))}$$
$$\left[ln\left(\frac{4\pi^2 P_t^2 t[\tan(\sin^{-1}(NA/n)]^4}{E_{th}\lambda^4} \right) \right]^{1/2}$$

Equation 2.18

$$l(P_t, t, NA) = 2z = \frac{2\lambda}{\pi[\tan(\sin^{-1}(NA/n))]^2}$$
$$\left[\left(\frac{4\pi^2 P_t^2 t[\tan(\sin^{-1}(NA/n)]^4}{E_{th}\lambda^4} \right)^{1/2} - 1 \right]^{1/2}$$

Equation 2.19

where d, l, Eth, P, t, NA, and n represent the voxel diameter, voxel length, threshold energy for polymerization, laser power, exposure time, numerical aperture of an objective lens, and the refractive index, respectively.

From a 2PP process, three different regions are obtained: (i) a fully polymerized region with high molecular weight (solid state), (ii) a weakly polymerized region with low molecular weight (solid-liquid state), and (iii) an unpolymerized region (liquid state). Generally, regions (ii) and (iii) are removed by rinsing materials in a development process. However, region (ii) could be utilized to generate ultrafine

features that have less than 30nm in lateral size. Figure 2.8 shows different polymerized regions obtained during a 400um diameter filter building tests (performed with 2PP set-up at LZH, as reported in chapter 6.6). A weak developing process was intentionally used to remove unpolymerized region (iii) and leave region (i) and (ii) intact. Region (ii) could actually enhance the filtering power of each pore.
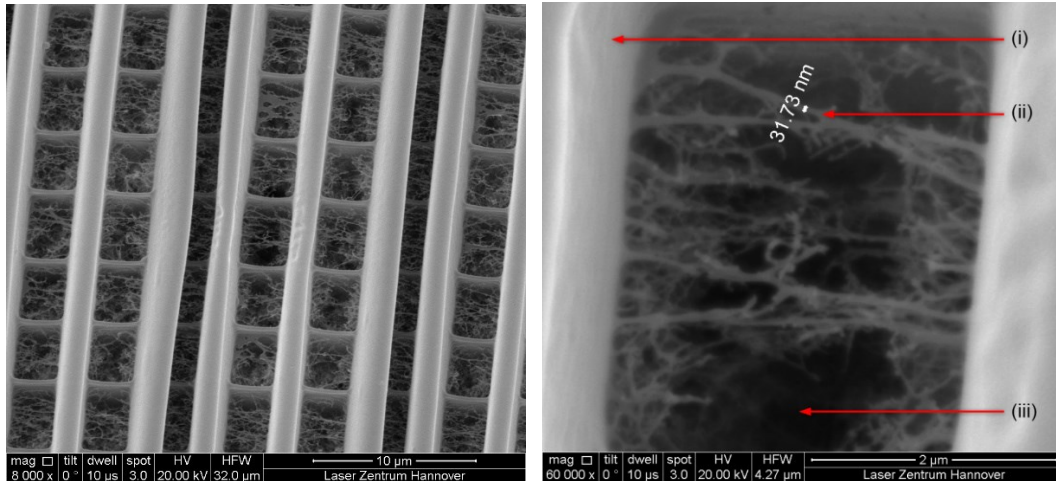
Figure 2.8 - (left) SEM images of fabricated voxels with the critical distance (5 um); dim nanofibers were generated near the voxels. (right) Well-generated nanofibers between polymer lines (printed at LZH Hannover).

When the interval between polymerized lines is significantly larger than a critical value, the coupling nanofibers did not appear since there is no overlap between voxels and lines in region (ii), as visible in Figure 2.9.
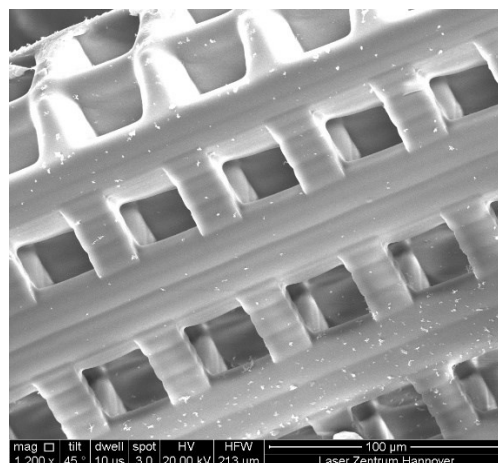
Figure 2.9 – Example of 2PP structure with absence of region (ii) due to distance between polymerized lines exceeding critical value (printed at LZH Hannover).

Chapter 3

3   Additive Manufacturing

3.1 Introduction

The advance of solid freeform fabrication techniques has significantly improved the ability to prepare structures with precise geometries, using computer-aided designs and data from imaging. These techniques include selective laser sintering, fused deposition modelling, 3D printing and stereolithography. Additive manufacturing is the formal term for rapid prototyping and is also popularly called 3D Printing. The term rapid prototyping (RP) is used to describe a process for rapidly creating a system or part representation before final release or commercialization. In other words, the emphasis is on creating something quickly and that the output is a prototype or basis model from which further models and eventually the final product will be derived [27]. The term rapid prototyping also overlooks the basic principle of these technologies since they all fabricate parts using an additive approach. A recently formed Technical Committee within ASTM International agreed that new terminology should be adopted. While this is still under debate, recently adopted ASTM consensus standards now use the term additive manufacturing [28]. Referred to in short as AM, the basic principle of this technology is that a model, initially generated using a three-dimensional Computer-Aided Design (3D CAD) system, can be fabricated directly without the need for process planning. Other manufacturing processes often require a careful and detailed analysis of the part geometry, to determine things like: the order in which different features are fabricated, tools and processes to be used, which additional fixtures may be required to complete the part. In contrast, AM needs only some basic dimensional details and a little bit of knowledge about AM machine working and employed materials. With AM, parts are made by adding material in layers; each layer is a thin cross-section of the part derived from the original CAD data which should be converted in the STL file format. Almost every AM technology uses the STL file format. The term STL was derived from STereoLithograhy, which was the first commercial AM technology from 3D Systems in the 1990s. STL files are an unordered collection of triangle vertices and surface normal vectors. Since

STL is essentially a surface description, the corresponding triangles in the files must point in the correct direction; in other words, the surface normal vector associated with the triangle should indicate which side of the triangle is outside vs. inside the part. As showed in Figure 3.1 the same CAD model(1) can be converted in a STL format with a different grade of accuracy (2,3) and the number of triangles define the resolution of the model.
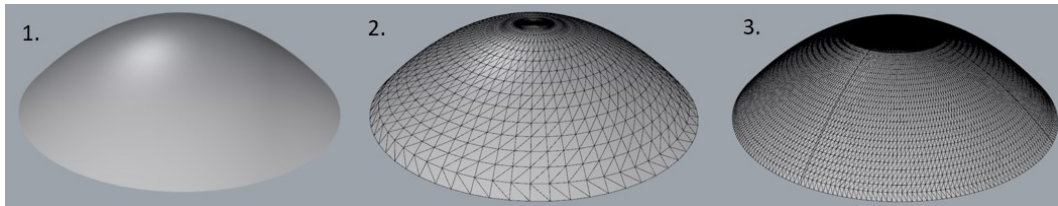
Figure 3.1 - STL file conversion. 1. NURBS model 2. Low accuracy meshing process 3. High accuracy meshing process

With a process called "slicing" the STL file is divided in a certain number of layers. The thinner each layer is, the closer the final part will be to the original as visible in Figure 3.2.
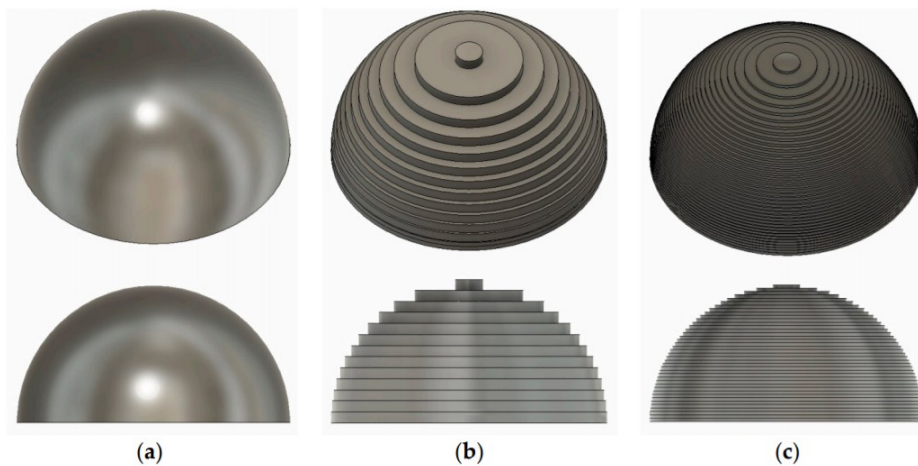
Figure 3.2 - Slicing process and relative accuracy. a) Ideal surface b) Slicing at 0.8mm layer height c) Slicing at 0.25mm layer height [29]

All commercialized AM machines to date use a layer-based approach; the major differences are in the materials they use, the way the layers are created, and how the layers are bonded to each other. Such differences will determine factors like the accuracy of the final part plus its material properties and mechanical properties. They will also determine factors like process time, how much post-processing is required, the size of the AM machine used, and the overall cost of the machine and

process. In Figure 3.3 all the technologies for Plastic AM are visible in correlation with durability, surface finish and details of printed parts.

Plastic 3D Printing

Polymerization process		Bonding agent	Melting process	
SL	PJ	BJ	FDM	LS
Stereolithograpy	Photopolymer Jetting	Binder Jetting	Fused Deposition Modeling	Laser Sintering

-	Durability	+
+	Surface Finish	-
+	Detail	-
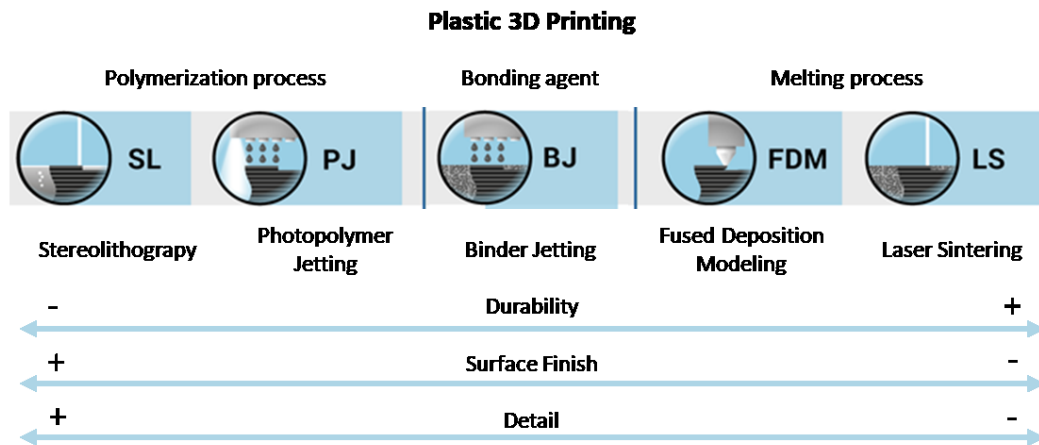
Figure 3.3 – Plastic 3D Printing available processes

Companies across the globe are using AM to reduce time-to-market, improve product quality, and reduce the cost to manufacture products. Polymers are attractive materials in this regard because they are economical, they provide for a broad range of properties and they are amenable to many low energy fabrication technologies. In the industrial sector, polymers are being used in a wide range of part applications including aerospace, defence, automotive, sports, telecommunications, and medical devices [30]. Therefore, this thesis will focus on the additive processes involved with the use of polymers with a mainly attention on stereolithography. In the next paragraphs, an overview on the additive manufacturing technologies object of this study is reported, with a particular attention on the employed materials.

3.2 Fused Deposition Modeling (FDM)

Fused Deposition Modelling (FDM), or Fused Filament Fabrication (FFF), is a technology based on the extrusion of a thermoplastic polymer in filament form following, layer by layer, a pre-determined geometry. Due to the relative ease of use and cost accessibility, FDM is one of the most widely used 3D printing technology.

Indeed, the system is often (with variations between the models) composed by an extrusion head with an output nozzle and a thermo-controlled printing bed. The extrusion head is attached to a 3-axes system, so that the deposition is tuned in the X, Y, Z space (Figure 3.4). When the nozzle has reached the correct temperature,

the polymeric filament is fed into the extrusion head and is melt. The deposition is performed in layer, each one formed by solidified polymeric strands. To make the polymer become solid, a decrease in the filament temperature is necessary when it is deposited: for this reason, often cooling fans are added after the extrusion head. When a layer is finished, the extrusion head is moved up until the pre-determined layer thickness is reached and a new layer is deposited. This process is repeated until the part is complete.

As regards printing strategy, often the objects realized with FDM are not compact and solid. Indeed, while the external portion, called shell, is built with several passes, the internal part is printed with lower density. The 'infill' parameter regulates the number and distance of polymer deposition to obtain a lighter internal structure. For desktop FDM printers, the default setting is 25% infill density and 1 mm shell thickness, which is a good compromise between strength and speed for quick prints [31].
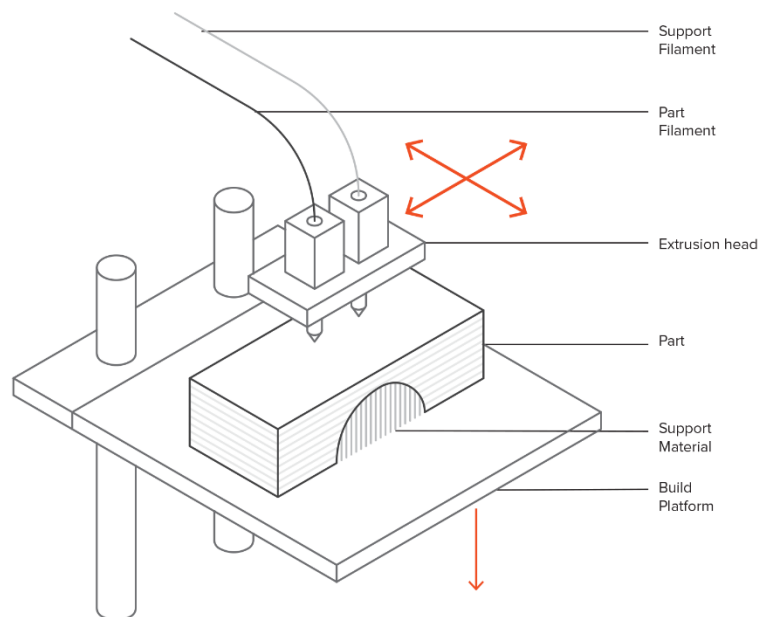
Figure 3.4 – Typical FDM machine set-up [31]

The process parameters typical for a FDM system are: (i) temperature of the nozzle, (ii) temperature of the building platform, (iii) head speed and (iv) speed of cooling fan. Then, there are other parameters which should be considered when designing: build volume and layer height.

Build volume is strictly related to the maximum size and object can have. Commonly on the market desktop printers with volume 200 x 200 x 200 mm^3 are found but, for industrial applications, also a 1000 x 1000 x 1000 mm^3 volume is available.

As regards layer height, also referred to as layer thickness, it is variable from 50 to 400 μm. As for slicing described earlier, the smaller the layer height, the smoother and more accurate the parts, at cost of higher printing times and costs. For this reason, commonly a 200 μm thick layer is used, even if the accuracy decreases.

Another drawback, with FDM technique, is warping as visible in Figure 3.5. Indeed, the cooling after deposition makes the melted material change its volume decreasing it. The rate of decrease mainly depends on the amount of deposited material and the distance from the building platform and, by consequence, could differ from section to section. A more precise control of the temperature and an enhanced adhesion to the platform and between the layers could avoid, or almost reduce, warping defects of the final object.

Figure 3.5 - A warped FDM part printed in ABS [31]

One of the adopted strategies to enhance layers adhesion is to set an extruder distance so that the polymer is pressed against the previous layer when deposited. Both the temperature of the melted and the pressure makes the superficial portion of the pre-printed layer melt again and bond with the newly extruded material. Surely, the bonding strength will be lower than the intrinsic strength of the raw material, thus leading to an anisotropy inside an FDM printed object. Moreover, since the melted filament is pressed, it will get an oval form giving to the whole object a "wavy" aspect (Figure 3.6). The part will be weaker along Z direction than on X,Y plane. This is surely of great importance when designing an item: for example, tensile test pieces printed horizontally in ULTEM® 9085 were compared to test pieces printed vertically and were found to have almost 84% greater tensile strength in the X,Y print direction compared to the Z direction (71.03 MPa compared to 38.48 MPa). [32]
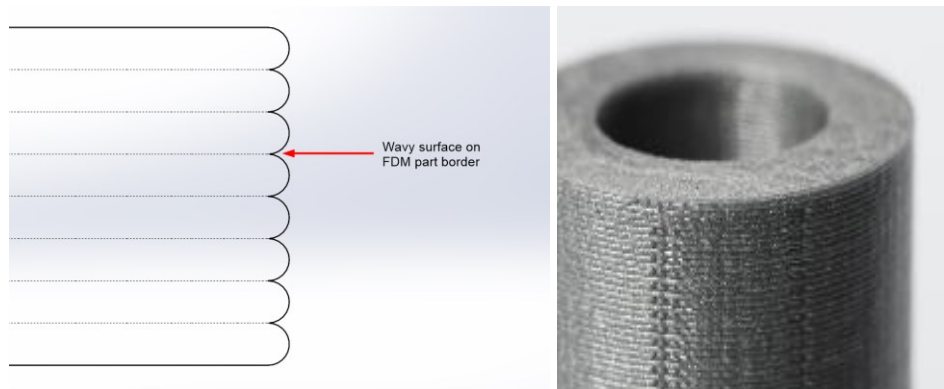
Figure 3.6 - The layer lines of an FDM part are generally visible [31]

From previous discussion it is evident that, without a supporting plane, no objects could be created. This is the reason why additional supports should be inserted if and object is characterized by overhangs. Overhangs are defined as suspended parts which hang out from an object. The general rule is that when an overhang angle exceeds 45°, supports are required (Figure 3.7).
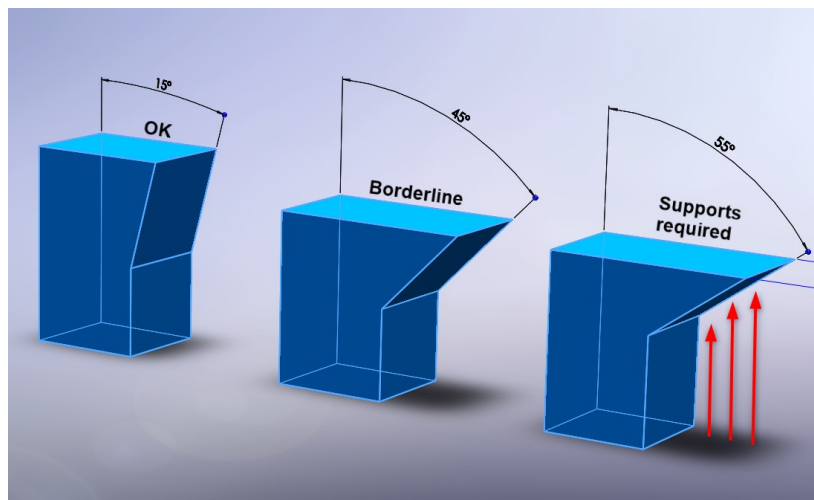
Figure 3.7 - Support options. For angle that not exceeds 45° no supports are required.

Surely, supports represent disturbing elements during a printing process. First, because they worsen the surface quality where they insert in the object; then, because they are often printed with the same material, thus leading to material waste. Some FDM printer developers have introduced two-heads printers: one head is devoted to the main material extrusion, the other to a lighter and water-soluble polymer to build the supports (MELFIL™). Obviously, the overall cost of a print is increased, making these printers suitable for high-end or industrial applications. Another aspect to be considered is the hatching strategy and consequently the infill

density (Figure 3.8). A correct strategy could improve total printing time without a significant impact on the part mechanical strength.
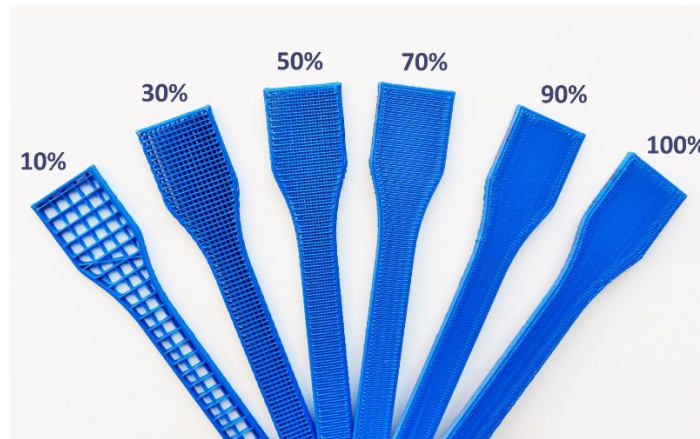
Figure 3.8 - The internal geometry of FDM prints with different infill density [33]

A wide range of materials is available for FDM printers: from common thermoplastics, such as Poly-Lactic Acid (PLA) and Acrylonitrile butadiene styrene (ABS), to engineering materials, such as Polyamide (PA), Thermoplastic Poly-Urethane (TPU) and Polyethylene Terephthalate Glycol (PETG) and high-performance thermoplastics, such as Polyether ether ketone (PEEK) and Polyetherimide (PEI). Figure 3.9 shows in a schematic way the available materials for FDM, divided by performance and internal structure.

Figure 3.9 - Printable material subdivided by performance

Going from bottom to the top of the pyramid, mechanical properties are enhanced, and costs are higher. Table 3.1 is reported to deepen the characteristics and highlight the differences among the cited FDM materials. Advantages are labelled with '+', disadvantages with '-'.

Table 3.1 - FDM materials

Material	Characteristics
PLA	+ Excellent visual quality + Easy to print - Impact strength: low
ABS	+ Good strength + Good temperature resistance - More susceptible to warping
Nylon (PA)	+ High strength + Excellent wear and chemical resistance - Humidity resistance: low
TPU	+ Very flexible - Difficult to print accurately
PETG	+ Food Safe + Good strength + Easy to print
PEEK	+ Mechanical strength + Visual quality - High melting temperature
PEI	+ Excellent strength to weight + Excellent fire and chemical resistance - Expensive

To resume, FDM has taken an important place in the field of additive manufacturing for its relative low-cost effectiveness in producing prototypes in short times. Moreover, it can process many different types of thermoplastic materials, ranging from high performance to common and economic polymers. Unfortunately, the comparison with other 3D printing technologies reveals its main disadvantage: resolution. Indeed, the FDM process itself is able to generate objects with visible layers which causes anisotropy and often requires a time-consuming post-processing if smooth finish is required.

3.3 Stereolithography

Stereolithography (SL) is an additive manufacturing technique which exploits polymerization induced by UV light to build 3D objects. A liquid resin, typically a blend of monomers, oligomers and initiator, is poured inside a vat where a platform can move up and down. The light source is focused on the liquid surface and when turned on, it reacts with the photoinitiator starting the polymerization process. If a laser beam is employed as light source, it comes to genuine stereolithography. Otherwise, if a light projector is used, it comes to DLP technique (Digital Light Processing), a derivative of SL. In the field of SL, is also possible to identify two different printing strategies as described in Figure 3.10: top-down and bottom-up approach.
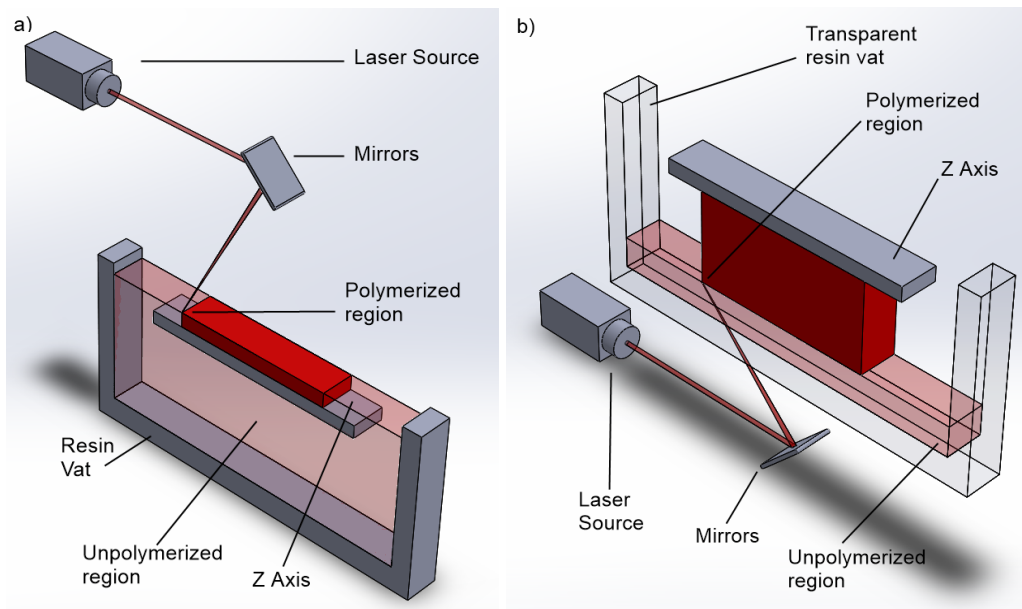
Figure 3.10 – a) Top-down and b) bottom-up SLA processes. a) The laser beam is deflected by mirrors on the surface of the photopolymer. The z axis moves down inside the vat to allow a layer by layer process. b) The laser beam, deflected by mirrors, pass through a transparent vat allowing polymerization while the z axis moves up.

In both strategies, objects are built layer by layer, but they differ for building orientation and UV source position. The first case (Figure 3.10) is commonly employed for industrial applications and is based on a platform moving down during printing and a UV source positioned above the resin vat. On the contrary, in the second case the configuration is reversed: the bottom-up strategy is frequently employed for desktop printers (e.g. Formlabs ®).

As described before, each additive process starts with the CAD design of the desired geometry, which can be modelled in a software, be described using mathematical equations [34], or derived from imaging technologies or tomography techniques [35].

The geometry file, converted in *.STL, is loaded in the stereolithography machine software, where a slicing programme divides the object in layer and creates the instruction for the machine (Figure 3.11). Typical parameters to be set for this technique are: (i) layer thickness, (ii) laser power density (mW/cm^2), (iii) laser scanning speed and (iv) hatch. Hatch involves the distance between two consecutive laser scans (called hatch distance) and the direction of each laser scan (called hatching strategy).
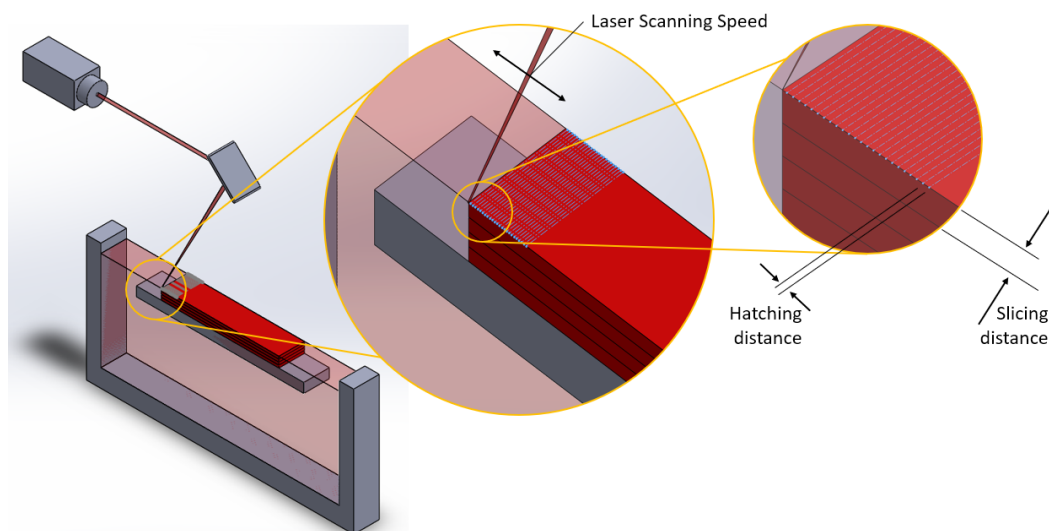
Figure 3.11 – Slicing and hatching parameters during a top-down building process.

For the first layer, the building platform moves down into the resin vat to obtain a liquid thickness equal to the layer thickness. In such way, the UV light will penetrate inside the resin for a defined depth (the layer thickness is chosen in accordance to the depth), making the first layer be polymerized and at the same time adhere to the platform surface. Layer thickness values range from 25 μm to 200 μm: even if lower thickness could enhance accuracy, it leads to longer printing times so, often best results are reached choosing 100 μm thickness. A good adhesion is fundamental for a printing process to be successful; indeed, if during the printing the growing object is kept fix, the polymerization and alignment of the layers is precise and allows for accurate results. However, it should be considered that a strong adhesion implies significant stress on the object during detachment from the

platform, causing permanent deformation or, in the worst case, break down. This is the reason why supports are introduced not only to hold overhangs but also to keep the object apart from the platform. The subsequent layers are built following the same procedure: a new layer of fresh resin is arranged, and the laser describes the geometry of each level. With top-down SLA printers, structures are built on a platform which is positioned below the resin surface at increasing depths with printing progress (Figure 3.10). The liquid resin thickness and homogeneity is managed by a moving blade which acts as a levelling recoater on the resin surface. In the bottom-up approach, light is projected from the bottom through the resin vat base (which must be transparent and non-adhering) and the platform is immersed into the resin downwards. In this case, each resin layer regularity is guaranteed by the distance from the resin vat base. Surely the latter strategy implies smaller amounts of resin than the first, lower oxygen inhibition (since the polymerized layer is dipped and not exposed to atmosphere) and a better control of layer thickness. But, being the polymerization confined to a tight volume between platform and vat surface, adhesion phenomena to the vat are frequent. For this reason, when the platform moves up to add layers during the printing process, a pulling force is applied to the growing object. To avoid process failure, the liquid resin is treated with higher energies to reach over-curing and make the object strong enough to detach without breaking. From literature, this over-curing causes decline of accuracy [36]. Table 3.2 summarizes the main characteristics of the cited strategies.

Table 3.2 -Top-down versus Bottom-up SLA processes

	Bottom-up (Desktop) SLA	Top-down (Industrial) SLA
Advantages	+ Lower cost + Widely available	+ Very large build size + Faster build times
Disadvantages	- Small build size - Smaller material range - Requires more post-processing, due to extensive use of support	- Higher cost - Require specialist operator - Changing material involves emptying the whole tank
Build size	Up to 145 x 145 x 175 mm	Up to 1500 x 750 x 500 mm
Typical layer height	25 to 100 microns	25 to 150 microns
Dimensional accuracy	± 0.5% (lower limit: ± 0.010 - 0.250 mm)	± 0.15% (lower limit ± 0.010 - 0.030 mm)

As regards supports, the same considerations discussed for FDM technique can be reported here. Support structures are printed in the same material as the part and must be manually removed after printing. As a consequence, the general rule is still valid: the least support, the better. An accurate positioning and orientation of the object on the printing platform is the best way to optimize the number and density of supports. However, it should be specified that the role of support is different when speaking about top-down or bottom-up SLA printers. In top-down SLA printers, supports are needed to hold overhangs and are suggested to reduce the influence of the adhesion between object and platform. On the contrary, in bottom-up SLA printers, supports are introduced for overhangs and bridges to be supported, but also to allow a proper orientation of the object. Indeed, as previously said, the growing part should be strong enough to withstand the pulling force exerted by the platform moving up. This force is directly proportional to the cross-sectional area of each layer. A good strategy (often implemented by the SL software itself) is to reduce each layer area by tilting the object with a proper angle: the resulting orientation could produce new overhangs, not directly connected to the object shape, which need to be supported. In order to clarify the role of supports for a bottom-up SLA printer, a bike bracket was built with the commercial Form1 and the resin Clear by Formlabs®. The result, before post processing and supports removal, is reported in Figure 3.12. More details about post processing are reported in the next paragraph.
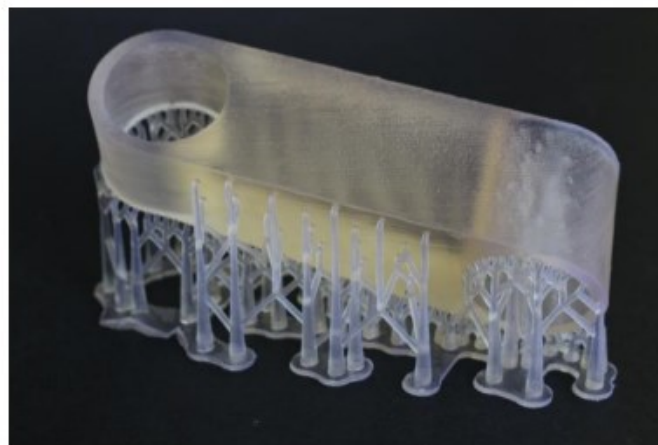
Figure 3.12 - Example of support generation for a bike bracket printing with bottom-up approach (Form1 3D printer by Formlabs®)

Differently from the materials described before for FDM printing, SL is based on thermoset polymers: they come in the form of a liquid resin which, when

polymerized, will burn instead of melting when heated. Moreover, since they are sensitive to light, they could degrade (both mechanically and visually) if exposed to sunlight for a long time.

Depending on the final finishing, the accuracy and the final mechanical properties, a great variety of SLA resins can be found in the market, ranging from about $50 for the standard material, upwards to $400 for special materials, such as the castable or dental resin. If compared to FDM or SLS thermoplastics, SLA materials are more brittle but have a smoother surface finish, thus they are usually used for visual prototypes rather than functional ones. Table 3.3 summarizes the advantages and disadvantages of the resins available from the market.

Table 3.3 - Resins comparison

Material	Characteristics
Standard resin	+ Smooth surface finish - Relatively brittle
High detail resin	+ Good dimensionally accuracy - Higher price
Clear resin	+ Transparent - Requires post-processing for a very clear finish
Castable resin	+ Used to create molds + Low ash percentage after burnout
Tough or Durable resin	+ ABS-like or PP-like mechanical properties - Low thermal resistance
High temperature resin	+ Temperature resistance
Dental resin	+ Biocompatible + High abrasion resistant - High cost
Flexible resin	+ Rubber-like material - Lower dimensional accuracy

3.3.1 Postcuring

At the end of a SL process, post processing consists of unpolymerized resin removal and cleaning of the built part. The solidified object is rinsed in a proper solvent

(frequently ethanol or 2-propanhol) and supports are gently removed. This part is often called "green", since it needs a further UV irradiation to conclude the polymerization process in a step called post-curing. It is important that, if present, supports are removed before UV final irradiation when the resin is not mechanically stable yet. Indeed, as the next paragraph will describe more in detail, the resin-laser interaction leads to the polymerization of strands, which cross-sectional area has a parabolic shape. The overlapping of these strands causes some liquid resin to be trapped inside the object, as schematically shown in Figure 3.13.
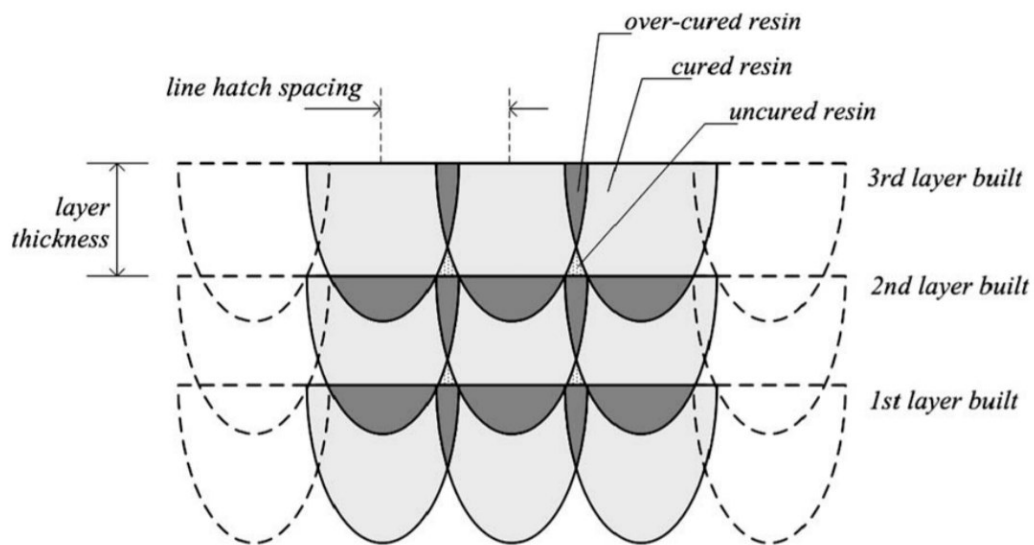
Figure 3.13 – Cured and uncured regions during SL process [37]

It is therefore important to finish the polymerization with a further and last step of UV irradiation. Completion of the polymerization can be observed by analysing the mechanical resistance, glass transition temperature, or density. It is also possible to use the infrared spectroscopy or differential scanning calorimetry.

3.3.2 Shrinkage

If warping is characteristic of FDM, shrinkage describes a similar behaviour of the printed object with SL technique. But it would be simplistic to define shrinkage as a deformation that occurs during printing, since the phenomenon is more complex and can result from specific printing steps. These steps have been identified aiming to reduce the influence of unwanted deformation on the accuracy of the final object and to indicate the printing phases which require a further care.

At first, shrinkage may occur during the building process: during polymerization upon exposure to the printer's light source, each layer is subjected to internal stresses. Unfortunately, these stresses have an impact not only on the single layer, but also on the interaction between subsequent layers, which results to curling of the part. As visible in Figure 3.14, the distortion can be evaluated by a "curl factor" defined in Equation 3.1.

$$curl\ factor = \frac{vertical\ distortion\ (h)}{total\ length\ of\ the\ free\ layer\ (L)} \qquad \text{Equation 3.1}$$
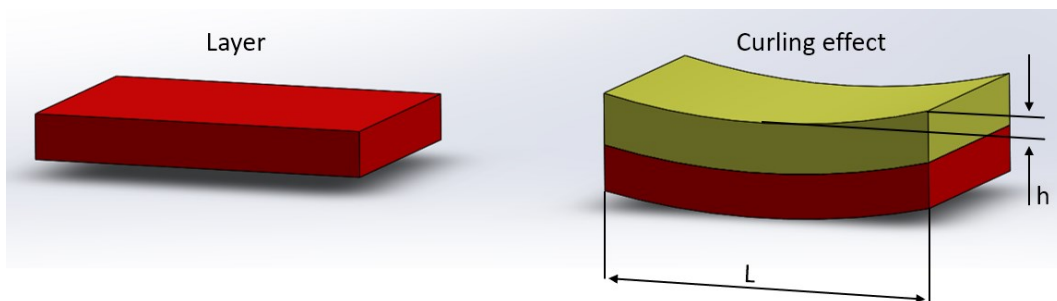
Figure 3.14 – Schematic of the curling effect on two polymerized layers

The supports removal is recognised as a further genesis of shrinkage. Indeed, during this phase, internal stresses of the object are released, and a new equilibrium is reached often causing curling of the part.

Finally, curl distortion can occur during post-curing. Indeed, as described before, post-curing is the step which aims to finish the curing of the unpolymerized resin trapped inside the polymerized matrix of the object. So, the remaining liquid resin becomes solid generating stresses which are difficult to be dissipated by the surrounding solid structure, thus causing shrinkage.

3.3.3 Laser interactions during stereolithography

The behaviour of resin upon irradiation described in paragraph 3.3.1 "postcuring" will be deepen in this section about the interaction between laser and liquid blend.

When a laser beam is scanned on the surface of the resin inside the printer vat, a strand is polymerized with a transverse area strictly dependent on: (i) resin characteristics, (ii) laser beam characteristics and (iii) scan speed.

Consider a 3D space, where the scan velocity is oriented along the x axis, the xy plane represents the resin surface and the z axis the direction of increasing depth inside the resin (Figure 3.15)
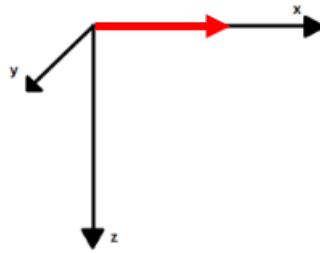
Figure 3.15 - Vs vector along x-axis

As the laser hits the resin surface, it transmits energy to the liquid mass; Considering the coordinate system reported in Figure 3.15, and supposing that the resin absorbs the laser light according to the Lambert-Beer Law, the irradiance at any point is connected to the irradiance at the free surface following the law reported in Equation 3.2.

$$H(x, y, z) = H(x, y, 0) * e^{-z/D_p}$$

Equation 3.2

H(x,y,z) is the irradiance, which can be defined as the radiant power of the laser per unit area. The area is the planar region hit by the beam, which has a non-infinitesimal spot. The parameter D_p (expressed in millimetres) is the penetration depth of the light into the liquid resin, defined as the distance at which the irradiance is 37% (1/e) of the irradiance at the surface. D_p is dependent on the resin optical properties.

Considering the laser beam intensity like a gaussian distribution (Figure 3.16), it is possible to write the irradiance in function of the beam radius as described in Equation 3.3

$$H(x, y, 0) = H(r, 0) = H_0 * e^{-\frac{2*r^2}{w_0^2}}$$

Equation 3.3
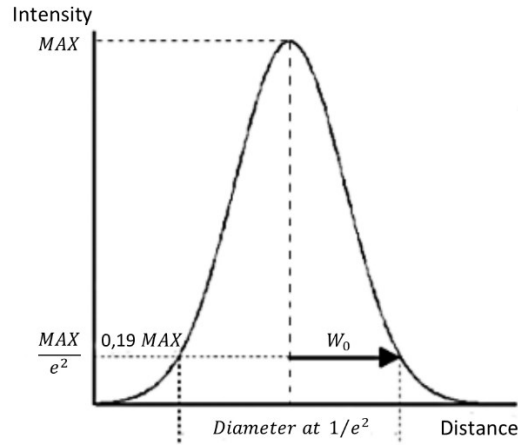
Figure 3.16 - Gaussian beam spot intensity distribution

According to Equation 3.3 and Figure 3.16, w_0 can be defined as the beam radius. The maximum irradiance, H_0, occurs at the center of the beam spot. It can be determined from the laser power formula. Laser power can be expressed as the integration of the irradiance over the spot area, as reported in Equation 3.4.

$$P_L = \int_{r=0}^{r=\infty} H(r,0)dA = \int_0^\infty H(r,0) * 2\pi r \, dr \qquad \text{Equation 3.4}$$

The integral solution can be expressed in terms of H_0 (Equation 3.5)

$$H_0 = \frac{2 * P_L}{\pi * w_0^2} \qquad \text{Equation 3.5}$$

So, the irradiance can be written in cylindrical coordinates as in Equation 3.6.

$$H(r,z) = \frac{2 * P_L}{\pi * w_0^2} * e^{-\frac{z}{D_p} - \frac{2*r^2}{w_0^2}} \qquad \text{Equation 3.6}$$

From the irradiance expression, it is possible to deduce the exposure at any point. Indeed, since the focus of this work in on stereolithography, exposure is a fundamental parameter which controls the curing degree of the liquid resin. E_c, or

critical exposure, is a typical value for stereolithography blends, since it indicates the exposure threshold above which the resin cures.

Considering a laser spot on a pre-determined scan line, exposure at any point can be determined by integrating Equation 3.6 along the path. Thus, the exposure equation can be expressed as in Equation 3.7.

$$E(x, y, z) = \sqrt{\frac{2}{\pi}} * \frac{P_L}{w_0 * v_s} * e^{-\frac{z}{D_p} - \frac{2*y^2}{w_0^2}} \qquad \text{Equation 3.7}$$

v_s is the scan speed for laser and is generally expressed in mm/s. The maximum value for exposure is along the scan line when y and z are equal to 0 (Equation 3.8)

$$E_{max} = \sqrt{\frac{2}{\pi}} * \frac{P_L}{w_0 * v_s} \qquad \text{Equation 3.8}$$

Starting from the irradiance and exposure expressions, it is possible to give more details about the resin strand polymerized by the laser. As seen in Paragraph 3.3.1, the cross-sectional shape of a polymerized line is very similar to a parabola, mainly characterized by a maximum width and a maximum depth, as schematically reported in Figure 3.17.
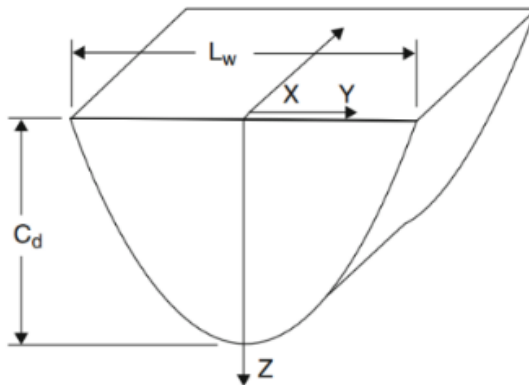
Figure 3.17 - A simplification of a cured line

Considering always the same coordinate system (Figure 3.17), if the scan line is along x axis and the laser spot centred in the origin (y=0), the maximum depth at which the resin polymerizes, also known as curing depth C_d, can be determined

solving Equation 3.7 by substituting $E(x,y,z) = E_c$, $y=0$ and $z=C_d$. Thus, cure depth is given by Equation 3.9.

$$C_d = D_p \ln\left[\frac{E_{max}}{E_C}\right]$$ Equation 3.9

This last equation (Equation 3.9) describes also the so-called "resin working curve". An example is given in Figure 3.18.
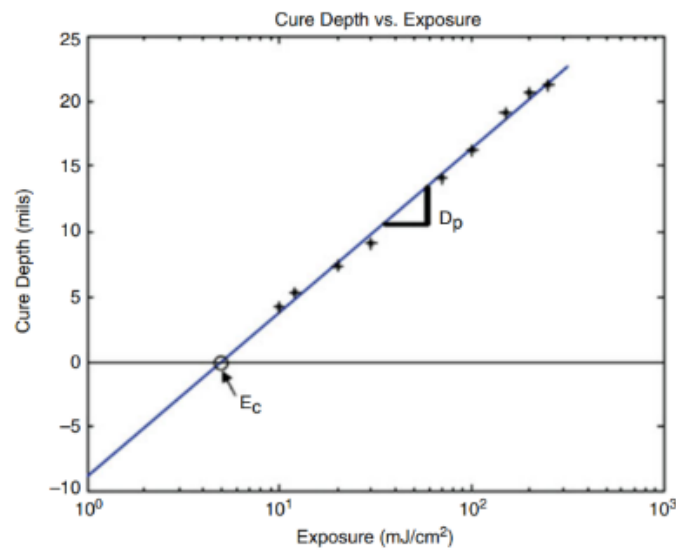
Figure 3.18 - Cure Depth in function of Exposure

Each resin can be characterized with this semilogarithmic plot reporting both the penetration depth (curve slope) and the critical exposure for a specific wavelength. Since both these parameters are strictly dependent from the resin, they are independent from laser power.

As for the cure depth, the width of the polymerized strand L_w can be found by substituting $E(x,y,z) = E_c$, $y = L_w/2$ and $z=0$; the result is reported in Equation 3.10.

$$L_W = W_0\sqrt{2 * C_d/D_p}$$ Equation 3.10

It can be concluded that a polymerized line has a width proportional to the laser spot radius and is a quantity which should be considered for compensation during printing process planning. Moreover, it doesn't only depend on the laser source, but

also on the intrinsic characteristics of the resin, which determine penetration depth and, by consequence, cure depth. Thus, each time a new material is studied to be used in a stereolithography process, a process characterization must be planned since, with the same light source, qualitatively similar materials could return completely different results.

Chapter 4

4   High Performance & Smart Manufacturing

4.1 Why HPM and SM?

The Ph.D. research activity on Smart & High Performance Manufacturing has been held in collaboration with the Materials and Micro Systems Laboratory of Politecnico di Torino (ChiLab) and Microla Optoelectronics Srl. The goal of this research was the analysis of the state of the art related to polymers employed for 3D printing, in order to promote a new approach using this technology to fabricate devices at micro- and nano-scale.

Considering the well extended research group active at DISAT (Department of Applied Science and Technologies) at Politecnico di Torino, in this work the candidate's contribution to the group research activity will be described. The research main topic is addressed to the additive techniques for smart device and Lab-On-Chip manufacturing. The main contribution was the design, realization and tuning of the optical path of a SLA printer (currently used at ChiLab Laboratory) with related software and electronic control unit as well as the writing of the SLA GUI Interface in C#. Some mechanical improvements, as the optical enclosure and recoating blade, were introduced. The SLA printer project was born with the aim to produce a completely customizable machine. Usually commercial 3D printers are not fully process tuneable and also require the same brand polymers to work properly or to obtain full building performance. In this SLA project the philosophy is to have a machine able to print new polymers prepared for research purposes at Politecnico di Torino. A completely tuneable firmware, software and optics parameters are available to adapt the building process to various physical propriety of each resin produced. Subsequently, considering the fully tuneable process philosophy, conductive polymers [38] could be printed. The main focus was on building parameters optimization to obtain a solid structure while object characterization tests were performed by other research members. At the end the

integration of SLA and 2PP technologies was applied in order to obtain the first Lab-On-Chip (LOC), as it will be described in the chapter 5. To guarantee the requirements for LOC it is necessary to test technology capability in terms of both performances and accuracy. Thus, SLA technology was chosen as the most accurate 3D printer machine at the micrometric scale which can be integrated with 2PP machine at the sub-micrometre scale. Moreover, these 3D printing fabrication procedures allow for the integration of sensors inside the 3D printed object. These technologies promote the fabrication of new high-performance devices based on smart polymers, able to measure and communicate data to the control unit.

4.2 First steps in Additive Manufacturing

First steps have been moved in the study of the Additive Manufacturing methodologies and techniques already present on the market. The first available 3D printer was an FDM machine (Velleman K8200) (Figure 4.1), which was used to become familiar with this kind of manufacturing.

Figure 4.1 - FDM printer

A 1:1 human hand reproduction (Figure 4.2), was chosen as first printing test. It is complete of all the joints (controllable by a series of wires hidden inside the object) and sensors and actuators can be integrated by means of a fully automated system. The connecting wires could be pulled and released by stepper motor in order to mimic movements of a real hand with the aid of integrated pressure sensors which close the control loop of the motors driver.

Figure 4.2 - FDM printed hand prothesis

By running different printing tests, it was possible to observe the relevance of correct building orientation to obtain satisfying results, both in terms of building accuracy and mechanical resistance. For this reason, part of the work was devoted to the study and evaluation of the *slicing* and *supports generation* methods. Among the most common software, the used ones were: RepetierHost, Slic3r, KissSlicer, Cura, Creation Workshop, Simplify3D and Magics.

Then, since the building accuracy was not suitable for the micrometric structures which were intended to be built (as previously stated), the attention was focused on a more precise technology. Thus, a customized SLA printer was designed and assembled (more details in Paragraph 4.3). Once the most important parameters for the 3D printing technology were identified from literature, some experimental tests were run to better understand the relationship between printing parameters and final object accuracy. Optical microscopy and profilometry were employed to determine the parts accuracy. This activity was fundamental to reveal the real performances of the available system and point out the lack of some features that can be implemented by the research team. Also, for SLA printing, aiming to enhance control over the design of the product, a study on the optimization of CAD geometries was performed. The Grasshopper plugin for Rhino was used to draw trabecular structures and generate fully modifiable complex patterns to proper hold the growing object. Once models and geometries were completed and converted in *.STL format, mesh analysis and correction were performed in AutoCAD Netfabb software: this phase is fundamental for this kind of manufacturing processes.

At the end, two main objectives were reached: a high level of knowledge relatively to additive manufacturing of 3D polymeric objects and a complete control of the fabrication processes.

4.3 Stereolithography Printing Machine Design

This section describes the design and assembly of a new, open source, stereolithography machine (Figure 4.3 shows the in-construction prototype) with variable printing area, high resolution, and all optics and electronics parameters controllable by the operator. Furthermore, the laser beam power can be modulated to polymerize different photocurable polymers and polymers doped by different functional fillers, such as conductive materials like metals.

Figure 4.3 - Developed SLA Printing Machine

4.3.1 Optical Design

The SLA machine optical path is composed by a laser source, a beam expansion section, a galvanometric scanner and a theta-lens. Both laser source characteristics and optical path elements influence the overall quality of a SLA machine building process. The candidate's contribution was to select and integrate both a laser source according with photopolymers characteristics and the series of optical elements that form the optical path.

Accordingly on section 2.4, most of the photo-initiators, used for stereolithography processes, have a peak of absorbance in the UV region (Figure 4.4). Thus, a laser source with a wavelength in this region is adequate for SLA application.
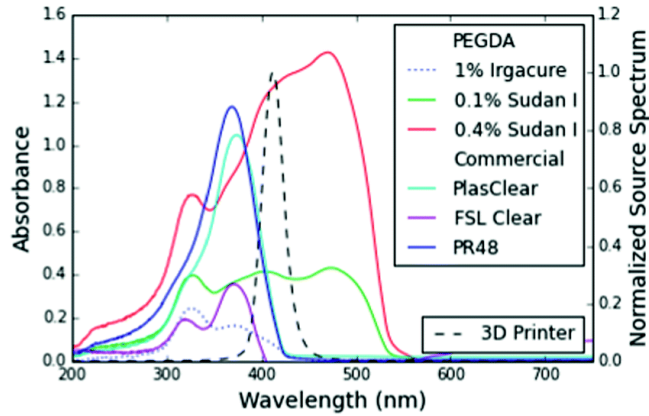
Figure 4.4 - Common SLA photo-initiators absorbance [39]

Based on this evidence, a 405nm laser source with a maximum power of 120mW was chosen. In Figure 4.5a some technical data and the drawings of this 405nm module are reported.
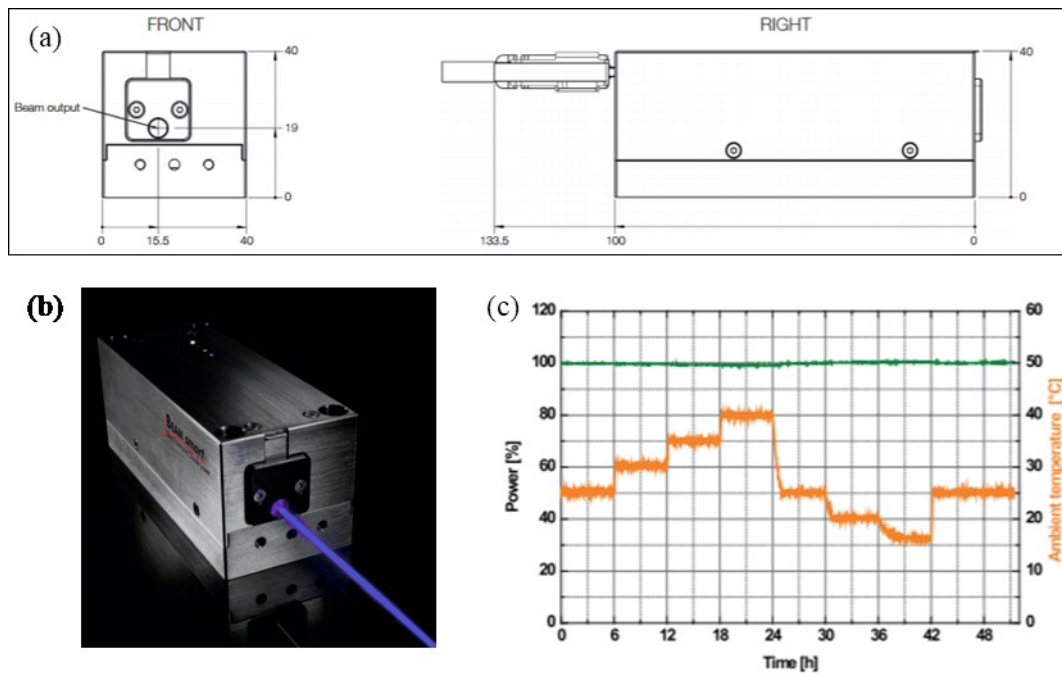
Figure 4.5 – 405nm Laser Module used in SLA Printing Machine. (a) module size; (b) commercial image and (c) output power stability tested during a period of 48 hours varying ambient temperature between 30°C and 80°C.

The graph (Figure 4.5c) shows its high power stability with a drift <0.5% during over 48 h. Another relevant aspect is the very low divergence of the beam, which is < 0.6 mrad and a $M^2 < 1.2$. The value of M^2 will be useful when the theoretical dimension of the focused spot size, at the F-theta corresponding working distance, will be calculated. This procedure will be reported at the end of this section, since other optical haven't been described yet.

Once the laser source was chosen, its output beam was characterized before proceeding with subsequent optical path components definition. As first, beam quality measurements were performed by evaluating the diameter of the spot with the Beam Profiler Ophir Spiricon SP503U by varying the output power and the distance between the source and the Charged Coupled Device (CCD) sensor inside the beam profiler. The active sensor area is 6.3 mm W x 4.7 mm H and the pixel dimension is 9.9 μm x 9.9 μm. The snapshot of each measurement is visible in Figure 4.6 while width and height values of the beam area are reported in Table 4.1 for each case.
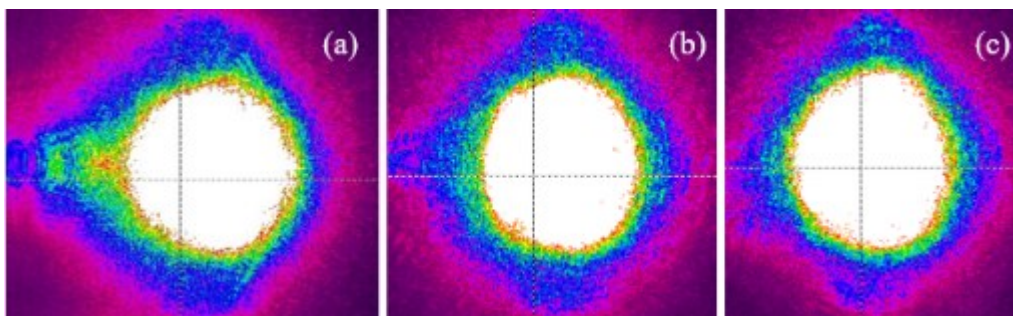
Figure 4.6 - 10 mW laser beam measured at various distance from CCD sensor: a) 0 mm; b) 100 mm; c) 200 mm

Table 4.1 - Spot dimension depending on power and distance from CCD sensor

Power [MW]

		10	20	30
Distance from CCD sensor [mm]	**0**	1.43 mm W x 1.4 mm H	1.47 mm W x 1.48 mm H	1.57 mm W x 1.55 mm H
	100	1.26 mm W x 1.4 mm H	1.41 mm W x 1.48 mm H	1.49 mm W x 1.56 mm H
	200	1.24 mm W x 1.41 mm H	1.39 mm W x 4.48 mm H	1.47 mm W x 1.58 mm H

The output beam diameter increases slowly and proportionally with the increase of the distance from the CCD sensor. Beam quality measurements confirm that the output of the laser is quite collimated with a diameter of about 1.5mm.

In the designed optical path, an optical expansion is required through the use of a Beam expander (BE). It is placed after the laser source and its function will be described later. As the name says, it is able to expand an input light beam depending on its expansion factor driven by the characteristics of the two constituting lenses. Figure 4.7 schematically describes how a BE works: in input a laser with a certain beam diameter is expanded of a multiplication factor depending on first lens physical characteristic. This expansion causes an increase of beam divergence. The last lens is used to collimate again the beam.
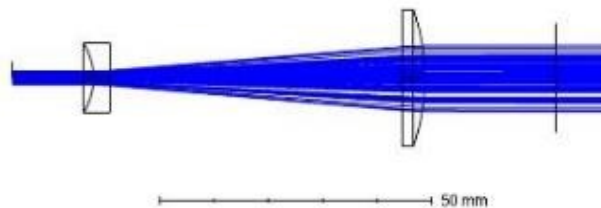
Figure 4.7 - Ray-tracing example of a BE.

To define the appropriate expansion value, the laser source beam diameter and Galvanometric scanner maximum input should be previously defined.

Most laser scanners use moveable mirrors to steer the laser beam. Usually, two closely spaced mirrors, which are mounted on orthogonal axes, are used to position a laser beam on a 2D plane. Each of the two flat or polygonal mirrors is then driven by a galvanometer obtaining what is called a galvanometric laser scanner. To

control the scanning motion, scanners need a rotary encoder and control electronics. The latter provide the suitable current to the galvanometer in order to rotate the mirrors of a desired angle value. A software usually controls the scanning motion, translating 2D information (ex. *.DWG or *.DXF files) in motion coordinates. The overall scan field depends on the F-theta lens used to focalize the laser beam.

In Figure 4.8 the deflecting mechanism of the laser by the galvanometer scanner is depicted.
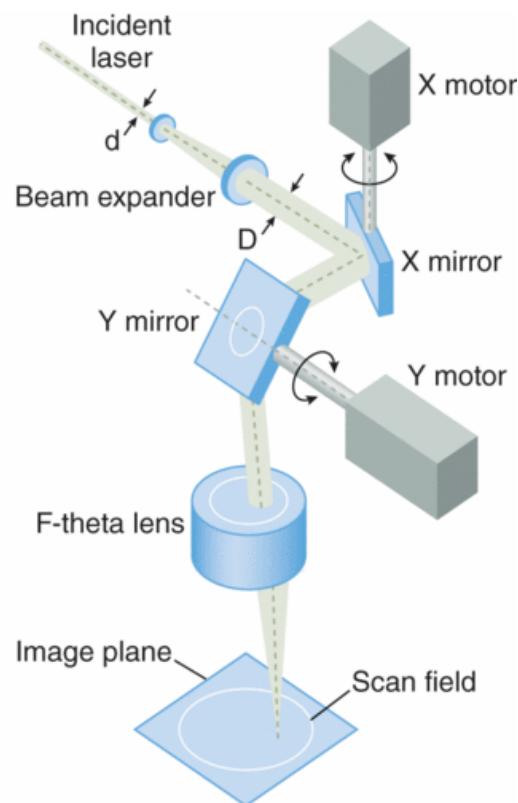
Figure 4.8 - A galvanometer laser scanner uses a couple of mirrors to deflect the beam over the required scan field. The F-Theta lens is a key element, able to focalize the beam at a certain distance depending on its focal length. Larger beam diameters can be focused to smaller spot sizes, but large mirrors can inhibit scan speed. [40]

The size of the mirrors that deflect the laser could be variable to fit different input beam size. Accordingly, the maximum input laser beam diameter is a Galvanometric scanner parameter that should be considered. In Figure 4.9 a galvanometric scanner with 9 mm maximum input diameter is reported.
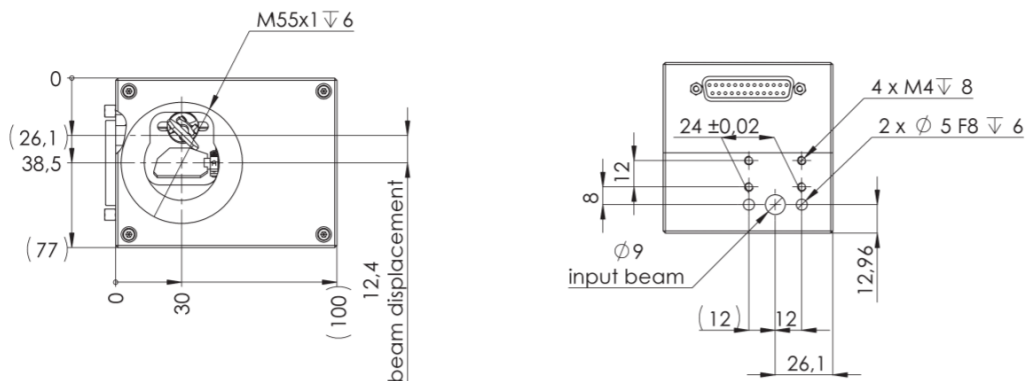
Figure 4.9 - Mechanical data of Galvanometric Scanner used in the SLA Printing Machine

In Table 4.2 relevant optical characteristics of the selected galvanometric scanner are reported.

Table 4.2 - Optical characteristics of selected Galvanometric Scanner

Mechanical data:

Max. input beam diameter (mm)	9.0
Beam displacement (mm)	12.4
Weight (without objective) (kg)	Approx. 0.8
Dimension (L × W × H) (mm)	100.0 x 77.0 x 77.5
Dynamic data:	
Acceleration time (ms)	0.23
Writing speed (cps)[1,2]	500
Positioning speed (m/s)[1]	7

[1]With F-Theta Lens f = 163 mm / field size 120 mm x 120 mm.
[2]Single-stroke font with 1 mm height.

The beam expansion is generally used to decrease the focused spot diameter in output from the overall optical path, when a F-theta lens is required. According to the Galvanometric scanner maximum input beam diameter, a 5× expansion was chosen to obtain an about 7.5 mm diameter spot size at the galvanometric head input. The BE is placed between the laser source output and the Galvanometric scanner input. BE main axis must be coincident with the ideally laser propagation axis to obtain what is considered a "perfect optical alignment". The same alignment is required for the Galvanometric scanner input hole.

To complete the SLA machine optical path, also a F-theta lens should be selected. It is used to focalize the laser beam on the free surface of the liquid photopolymer. F-theta lens were engineered to provide the highest performance in laser scanning or engraving systems. These lenses are mainly used for engraving and labelling systems, image transfer, and material processing. If a spherical lens can only focus an input laser beam along a curved plane (see Figure 4.10a), the flat-field scanning lens solves this problem (Figure 4.10b). In this case, the displacement 'd' of the beam has a non-linear relationship with the effective focal length (f) and the deflection angle θ (Equation 4.1).

$$d = f * tan\theta$$
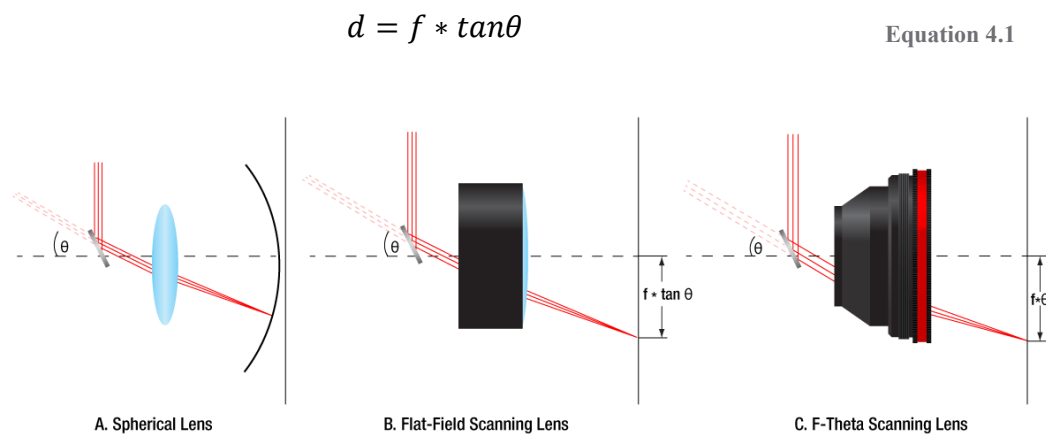
Figure 4.10 - Differences between simple lenses and F-Theta lenses

While this nonlinear displacement can be corrected with the proper software algorithm, the ideal solution is to obtain a linear displacement. F-theta lenses are designed with a barrel distortion that yields a displacement that is linear with θ (Equation 4.2).

$$d = f * \theta$$

Equation 4.2

This simple response avoids the need for complicated electronic correction and allows for a fast, relatively inexpensive, and compact scanning system. F-theta are usually screwed on Galvanometric scanner. Some of the most important factors to be considered are the operating wavelength, the working distance and the working area. The operating wavelength (405 nm in this case) is related to the galvanometric mirror coating. The working distance is the distance between the housing of the lens

and the paraxial focus point, as visible in Figure 4.11. The working area is an imaginary square with a certain width and height that represents physical limits of beam deflection through the F-theta lens. Thus, the beam will describe figures only inside this defined area that must be large enough to cover all the working plane.
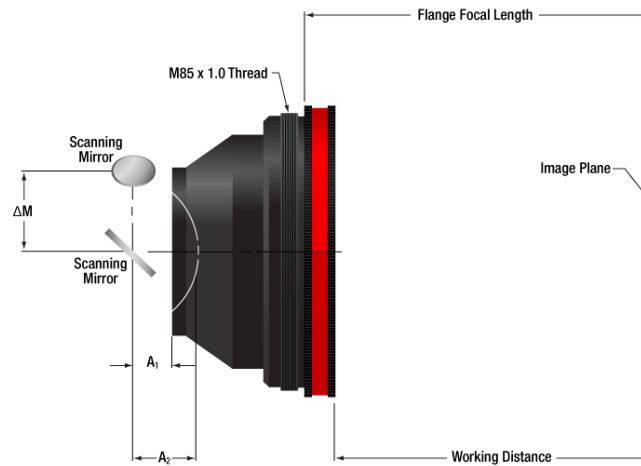
Figure 4.11 - F-Theta lens relevant mechanical and optical data

Considering the formula used to calculate the output radius from a lens (Equation 1.14), the output beam diameter of the F-theta is calculated as in Equation 4.3.

$$D_{foc} = \frac{4f\lambda\, M^2}{D_0\pi}$$

Equation 4.3

From Equation 4.3, it is clear that the spot diameter in output from the overall optical path depends on multiple factors. D_0 is the F-theta lens input diameter and depends on the expansion factor. A higher value of D_0, thus a higher expansion factor, will lower the final spot diameter. M^2 should be the lowest possible. Usually, the lower M^2 value, the higher the laser source cost. Therefore, the beam quality must be chosen after a cost/benefit analysis. The focal length f is also relevant. Higher values allow higher scanning field and working distance but higher spot diameter. Considering the designed optical path, a beam diameter of 1.5 mm with an M^2 of about 1.2 was expanded five times obtaining a 7.5 mm spot in input on the galvanometric scanner. A theta lens focal of 260 mm was used to focalize the spot on the resin. Using these optical components, a nominal diameter value of about 21 µm is obtained using Equation 4.3. Measuring the real output beam with the Beam Profiler SP503U, we obtained a diameter measurement of about 80 µm W x 80 µm

H. This difference from the theoretical value is quite normal; it lies in both the formula approximations and the difficulty to achieve a perfect optical alignment between the optical components. As visible in Figure 4.12 the laser spot shape can be considered as gaussian in the XYZ space.
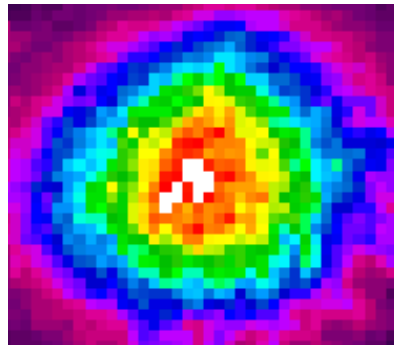
Figure 4.12 - Spot measurement after the BE 5x and F-theta lens with 10mW laser output power. Due to the characteristic of the CCD is not possible to achieve a higher resolution image. Each pixel on sensor is about 9 μm x 9 μum. The highest laser power density is marked with red or white pixel (sensor clipping) and it extends for a radius of 4-5 pixels, thus a spot of about 80um diameter can be considered.

Mechanical parts with micrometric tolerances were designed and realized to assembly the overall optical path. According with the chassis design, a solid base was designed to accommodate the source and the beam expander. Also, a special fixing part was designed to support the galvanometric scanner in place allowing the collinear alignment of the source with the beam input entrance. The ideal optical axis was placed at 35 mm height from the lodging base top surface. A 3D-image of the optical set-up is visible in Figure 4.13a. The top view drawing shows the position of each component and the optical path of the laser beam starting from the source until the theta lens (Figure 4.13b).
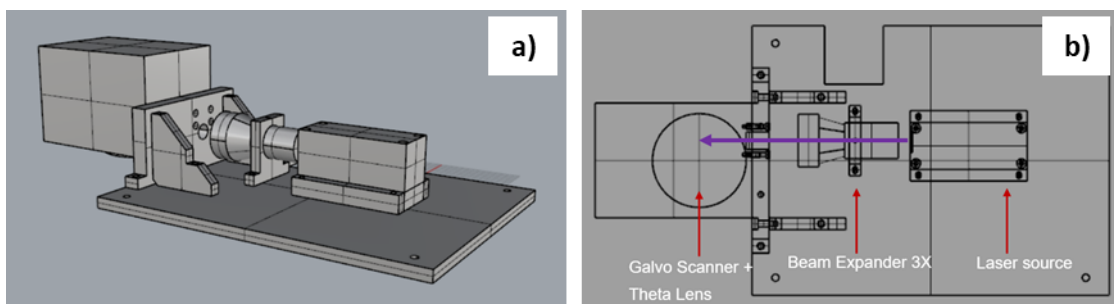
Figure 4.13 - Optical set-up designed with Rhinoceros. a) Isometric view b) top-view in which the laser propagation in indicated with a purple arrow.

4.3.2 Laser Scanner Hardware

After the design of the optical set-up, a scanner controller board was selected. Different galvanometric scanners are available on the market but all of them use the same protocol to communicate with the scan head. This protocol is called XY2/100 and allows for distinct brand components integration without compatibility problems. Usually, every brand sells his galvanometric scanners together with an electronic controller board and a related software. Buying from the same producer is advisable but not mandatory. The chosen scanner controller board (E1701) has been designed for controlling galvanometric scanner systems with two or three axes. Depending on the extension boards used, which are optional, they also supply extensive signals for laser and external control (Figure 4.14). The communication between the host system and the controller boards is provided via Ethernet or USB. This baseboard can be used to control 2D or 3D scan-heads that come with a XY2-100 or XY2-100-E interface. The baseboard can be combined with extension boards without any restrictions. E1701D offers the following features:

- XY2-100 interface to scan-head with X, Y and Z channel;
- XY2-100-E interface to scan-head with X and Y channel;
- 100 Mbit Ethernet connection;
- USB 2.0 connection;
- Online XYZ grid correction with support for several correction table file formats (like SCAPS® *.ucf, Scanlab® *.ctb and *.ct5, Raylase® *.gcd);
- Fast switching between up to 16 preloaded grid correction tables;
- Command execution time down to 0,5 microseconds;
- Real-time processing of laser and scanner signals;
- 26-bit internal resolution (for better quality also with 16 or 18 bit hardware output);
- Can control nearly every laser type (this may require extension boards as described below);
- Two laser CMOS digital outputs for usage with YAG, CO_2, IPG® and compatible laser types (outputs can provide PWM frequency, Q-Switch, FPK-pulse, CW/continuously running frequency, stand-by frequency) running with frequencies of up to 20 MHz;
- BeamConstruct PRO license included;
- Open source compatibility library that emulates existing programming interface for fast and easy usage with existing software (contains e.g. Scanlab® RTC4®, SCAPS®, USC®/SCI and other.

Among the features, full compatibility with the XY2/100 protocol is available, a full support for different producer correction table, a very fast command execution, CMOS digital outputs for Continuous Wave laser sources and also the BeamConstruct Pro licence included.

Figure 4.14 - E1701 laser scanner controller

The software included is one of the most important aspect of this board. It is able to manage *.stl files and perform the slicing and hatching processes directly inside the interface. When this board was chosen, it was the best price/feature solution mainly because not many software for the direct managing of *.stl files were available on the market. The E1701D is also based on a BeagleBone board which is fully compatible with the printing machine core board (a BeagleBone too). Figure 4.15 reports an easy block diagram showing the hardware architecture of the whole system.
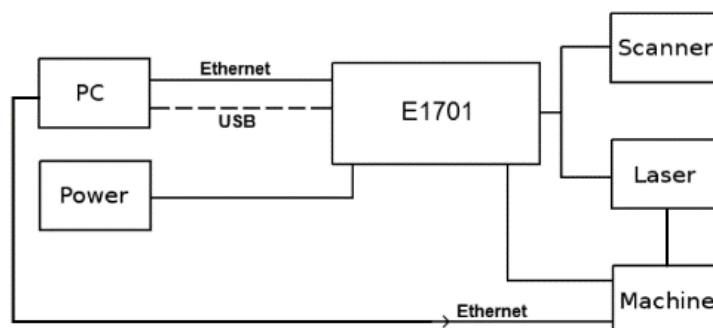
Figure 4.15 - SLA Printer Machine Block-Diagram

The BeagleBone core, based on Linux Debian distribution, houses the python code used to manage the Z stage positioning and the stepper motor used for the recoating process. The BeamConstruct software, after the *.stl file processing, is pulled in a stand-by process waiting for the "laser on" signal coming from the E1701. After receiving this signal, one layer of the *.stl file is processed. After each layer, the software turns again in a stand-by status waiting for a new trigger coming from the E1701; the python core manages the movement of the Z stage. The sequence, in accordance to the standard SL procedure as described in 3.3, is:

- Z stage movement down for the immersion inside the photopolymer;
- Z stage movement pause until the recoating is completed;
- Z stage movement up until the recoater positioning;
- Y stepper motor movement to allow the recoater to remove the excess material on the top of the recoated part.
- Z stage movement down until the new layer position is reached.

In this way the layer-by-layer process could be completed.

The python core firmware has a series of functions. The most relevant are reported as follows:

- 3D – Start the printing process, synchronizing stages and laser signals.
- Go_0 – Move the Z stage in home position, allowing the easy remove of the printed object or for tuning the alignment of the working plane.
- Go_racla – Move the Z stage to set the delta between the "racla" and the working plane.
- Go_start – Move the Z stage to a distance equal to the working distance of the theta lens.
- Minicom – Special command to manage the laser source, change power and set the external triggers.

4.3.3 Graphical User Interface (GUI)

As visible in Figure 4.15, the connection between PC and the BeagleBone (Machine) is through Ethernet cable. A Secure Shell (SSH) protocol connection is established with the BeagleBone and the execution of the various functions can be enabled with easy Linux bash commands. A C# GUI was designed to make the printer user friendly, avoiding the use of SSH client and bash coding. The software screenshot is reported in Figure 4.16 and Figure 4.17.
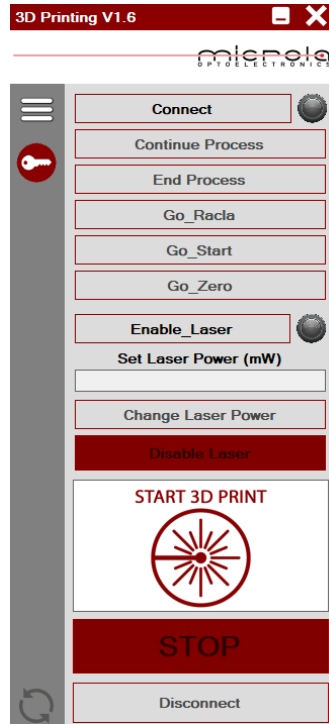
Figure 4.16 - .NET Framework based GUI written in C#
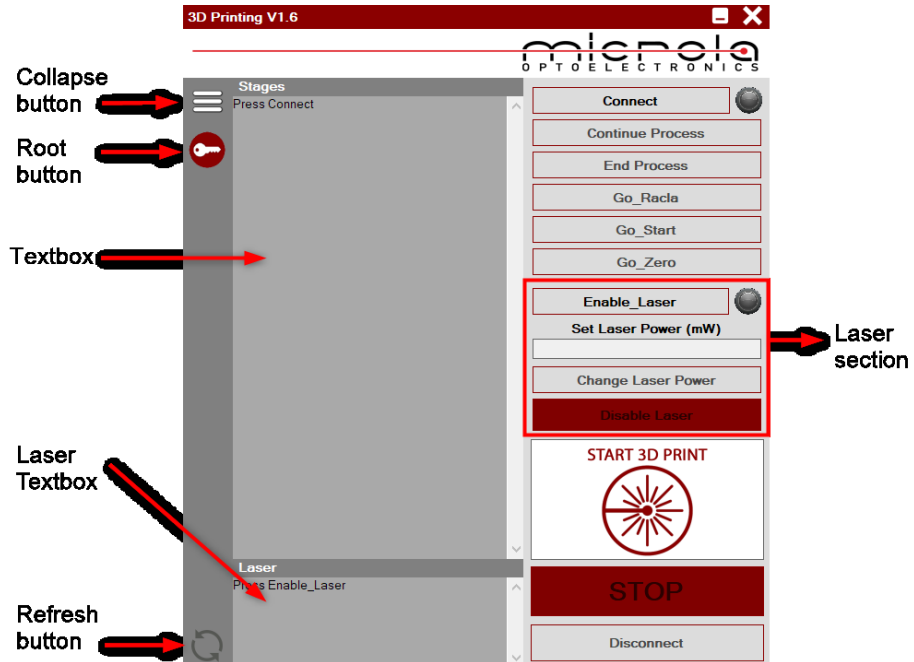
Figure 4.17 - .NET Framework based GUI written in C# with expanded control status window

The software has a collapsible window (Figure 4.17) which allows to hide the text box panels used to retrieve a real-time output from the bash and manage the status of the printing process or possible errors. The pseudo-code is reported below while the complete C# code script is reported in the Annex 1.

CONNECT SECTION

IF *Connect* button is clicked //Open a SSH Connection with the Beaglebone
      Create new ssh connection "client" (IP ; Port ; User ; Password)
      Connect client
      Create ShellStream
      Read ShellStream
            //The software checks when the SSH client is ready to retrieve commands
            IF ShellStrem text is equal to "[$>]"
                  Update Textbox content with new Shellstream data
                  //Firmware script are stored in a certain folder inside the Beaglebone system
                  Send to ShellStream bash command to browse firmware folder
                  Update Textbox content with new Shellstream data
                  Disable connect button
                  Enable *Root* button
                  Enable *Disconnect* button
            ELSE
                  Manage connection error

IF *Root* button is clicked //Get root privilege, required to launch the firmware python scripts
      Send to ShellStream bash command to get root privilege
      Wait 1 second
      Send to ShellStream password to get root privilege
      Read Shellstream
      Update Textbox content with new Shellstream data
      Disable *Root* button
      Enable *End Process, Go Racla, Go Start, Go Zero, Enable_Laser, START 3D PRINT* buttons

LASER SECTION

Connect to Laser Client //Open a separate SSH Connection with the Beaglebone to manage the laser
      IF *Enable_Laser* button is clicked
            Create new ssh connection "Laser_client" (IP ; Port ; User ; Password)
            Connect Laser_client
            Create Laser_ShellStream
            Read Laser_ShellStream
                 //The software check when the SSH client is ready to retrieve commands
                 IF Laser_ShellStream text is equal to "[$>]"
                     Update Laser_Textbox content with new Shellstream data
                     Send to Laser_ShellStream bash command "minicom" to open Laser control

//The software check when the Laser client is ready to retrieve commands
Read Laser_ShellStream text untill is equal to "\s"
Update Laser_Textbox content with new Shellstream data
Send to ShellStream bash command sequence to enable laser
Enable buttons and textbox related to laser section

ELSE

Manage laser connection error

IF *Change Laser Power* is clicked //Set laser power function
retrieve data from Power_Textbox
IF text is a string
Manage format exception error
ELSE
Send Laser_ShellStream bash command to set laser power
Update Laser_Textbox content with new Shellstream data

IF *Disable_Laser* button is clicked //Disable Laser function
Send to ShellStream bash command sequence to disable laser
Update Laser_Textbox content with new Shellstream data
Disable buttons and textbox related to laser section

PRINT SECTION

IF *Go_Racla* button is clicked //Go racla movement function
Send to ShellStream bash command to start firmware python script "go racla"
Update Textbox content with new Shellstream data

IF *Go_Start* button is clicked //Go start movement function
Send to ShellStream bash command to start firmware python script "go start"
Update Textbox content with new Shellstream data

IF *Go_Zero* button is clicked //Go zero movement function
Send to ShellStream bash command to start firmware python script "go zero"
Update Textbox content with new Shellstream data

IF *START 3D PRINT* button is clicked //3D Print function
Send to ShellStream bash command to start firmware python script "3d print"
Update Textbox content with new Shellstream data
Start Timer1
Start Timer2
Enable STOP button

Timer1 will execute commands every 2 second
//Timer1 is used to read the ShellStream and update Textbox each two second
Update Textbox content with new Shellstream data

Timer2 will execute commands every 1 second
//Timer2 is used to manage the firmware Continue/End process request. The firmware asks for a Continue Process confirm, at the end of the first built layer. The firmware also asks for a Continue/End Process when laser results as inactive (caused by incorrect settings / building process end)
IF *Continue process* button is clicked
       Send to ShellStream bash command to continue process
       Update Textbox content with new Shellstream data
IF *End process* button is clicked
       Send to ShellStream bash command to End process
       Update Textbox content with new Shellstream data
       Stop Timer1
       Stop Timer2

IF *STOP* button is clicked //STOP function
       //In Linux the bash command CTRL+C stops immediately each command previously launched. STOP button acts as emergency button.
       Send to ShellStream bash command [CTRL+C]
       Update Textbox content with new Shellstream data
       Stop Timer1
       Stop Timer2

GUI INTERFACE SECTION

IF *Refresh* button is clicked //Refresh function
       Update Textbox content with new Shellstream data

IF *Collapse* button is clicked //Hide Textboxes
       Change Windows Form Width
       Hide Textboxes visibilities

DISCONNECT SECTION

IF *Disconnect* button is clicked //Disconnect to SSH Client
       Disconnect client
       Disconnect Laser_client
       Disable buttons
       Enable connect button
ELSE
       Manage disconnection error

4.3.4 Machine Enclosure and Optical Safety

Once the optical path, electronics and software were ready, it was possible to design and add some aluminium profiles on the chassis. These were used to sustain the outside cover panels and to realize two doors on the front panel: one on the top, to access directly the working area, and one on the bottom to allow the maintenance and the resin storage. In Figure 4.18 the design steps performed to obtain the enclosure of the printing machine are depicted.
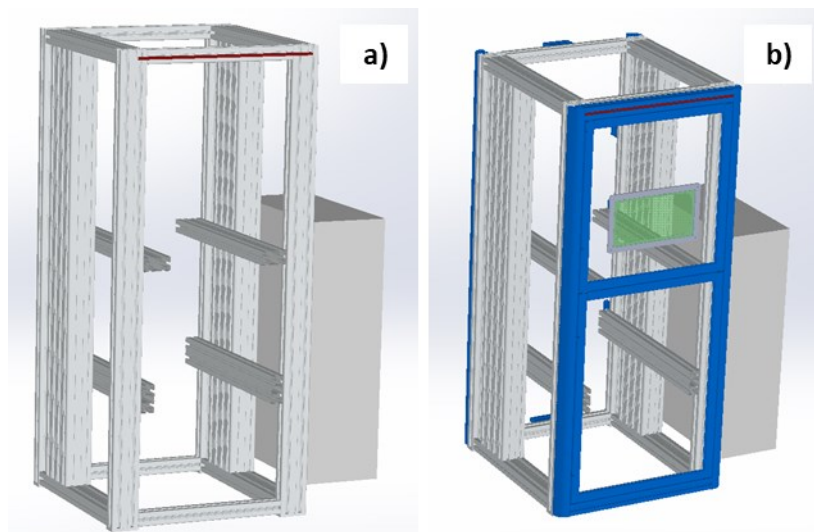
Figure 4.18 - SLA 3D printing machine design of enclosure's chassis and panelling. a) Main chassis without panelling. b) Profiles, visible in blue, designed to carry Peralluman panels for optical safety. An optical window, able to filter 405nm wavelength, is present to make visible the laser working area when doors are closed.
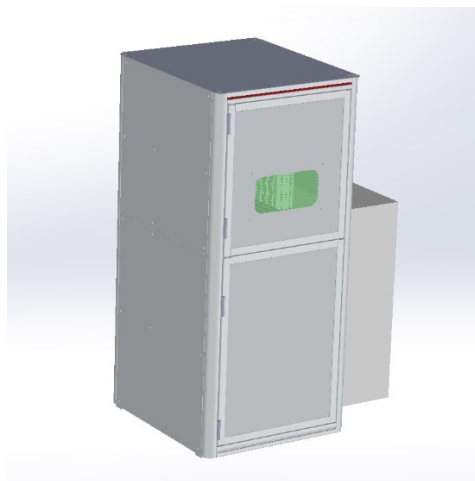
Figure 4.19 - Complete CAD model of the SLA chassis

The design of the panelling follows the normative IEC 60825-1:2014 "Safety of laser products" – (*Part 1: Equipment classification and requirements*). IEC 60825-1:2014 is applicable to laser products emitting laser radiation in the wavelength range 180 nm to 1 mm. Attention was given also to the IEC TR 60825-5:2003 "Safety of laser products" – (*Part 5: Manufacturer's checklist for IEC 60825-1*). The laser installed in the prototype is classified as Class 4. This class of lasers are hazardous for eye exposure. They also can burn skin and especially dark and/or lightweight materials at close range. Visible-light Class 4 lasers have an output power 500 milliwatts and above. The optical safety is one of the most important aspect when lasers are used. For this reason, laser-cut Peralluman panels were designed, realized and installed as optical protection following properly the above reported *IEC 60825-1*. An optical safety glass for 405nm laser source was installed on the top door, allowing the user to see inside the machine during the printing process without any optical risk. An interlock and relative safety relay were added to the machine. Whenever the user opens the main door, laser supply and axes movement are suppressed to avoid any kind of risk. The figures below show a sequence of building steps starting from the open chassis in Figure 4.20 a) to optical path assembly in Figure 4.20 b) until the complete enclosure in Figure 4.21.
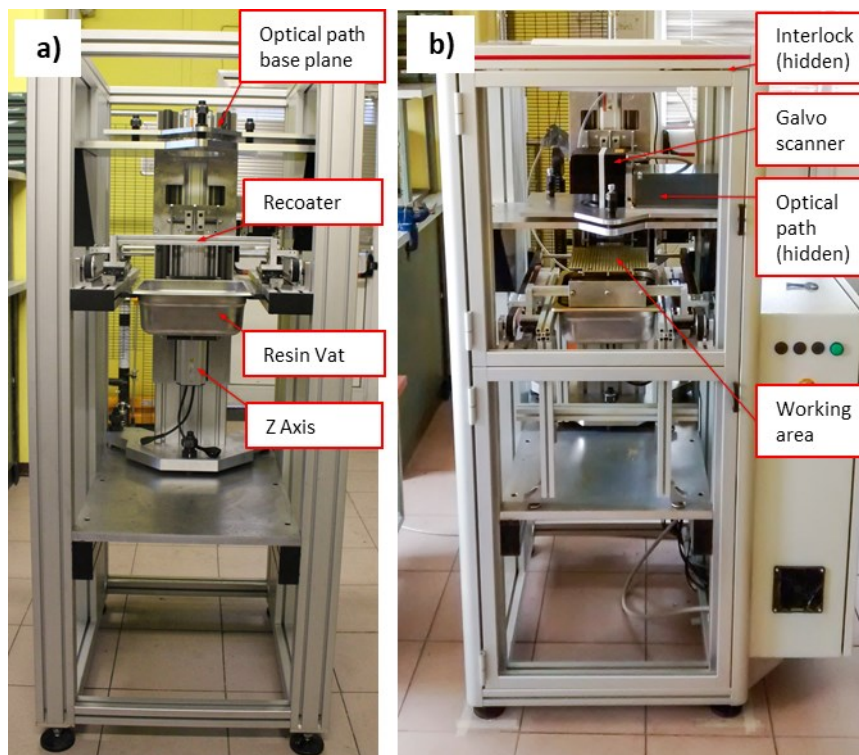
Figure 4.20 - Assembly of enclosure's chassis and panelling.

Figure 4.21 – SLA Printer completed enclosure.

Chapter 5

5   Experimental activity

5.1   Polymerization tests

This section is dedicated to the experimental work performed with the built SL machine. Attention was given to the laser processes to carry out a relationship between the obtained voxel dimensions and the known laser spot size. The voxel dimension is not equal to the spot diameter in XY plane. Light radiation is mainly absorbed by the photopolymer and the power density, assumed to have a gaussian shape, is higher in the centre of the spot and lower on the side areas. This will cause a high conversion in the centre, but also a diffusion of the polymerization process, with a low conversion rate, on the side areas. This will increase the final voxel dimension. The difference between the spot size and voxel dimension depends on laser power and spot size, the amount of photo-initiator inside the resin and the numeric aperture of the F-theta lens. A series of points and lines were polymerized to define the voxel dimension and analysed with the microscope and profilometer to evaluate the effective difference between the spot size and the real polymerized volume. The test pattern for the Design Of Experiment (DOE) includes 12 dots as visible in Figure 5.1 on line 1 and 12 lines visible on lines 2,3,4,5.
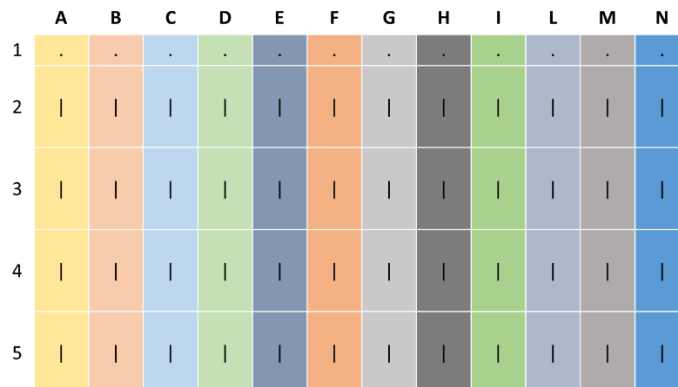
Figure 5.1 - Polymerization test pattern

The same power (10 mW) was used for each dot and line polymerization. Excluding the dots that can be considered as a punctual process, not influenced by marking speed, each row was written with a decreasing speed. Respectively, line 2,3,4 and 5 were polymerized with a speed of 2 m/s, 1.5 m/s, 1 m/s e 0.5 m/s.

The minimum measured voxel size was 200 μm W x 200 μm H (Figure 5.2) with a thickness of 60 μm (Figure 5.3). As visible in Figure 5.3, the polymerized voxel has been captured by the profilometer KLA Tencor P10; the shape is similar to a truncated pyramid so the size both on the top and at the bottom of the structure should be evaluated. On the top, the size is reduced and is about 100 μm W x 150 μm H (Figure 5.2a), while on the bottom is about 220 μm W x 200 μm H (Figure 5.2b).
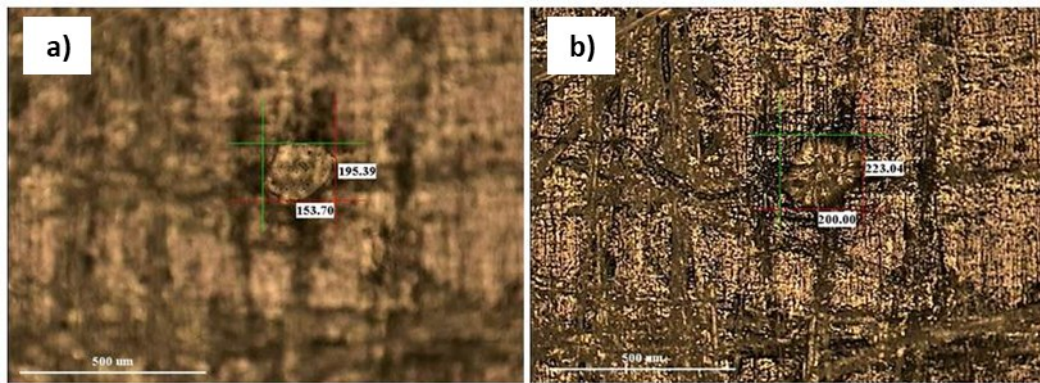
Figure 5.2 - Microscope dimensional spot analysis a) top-zone b) bottom-zone
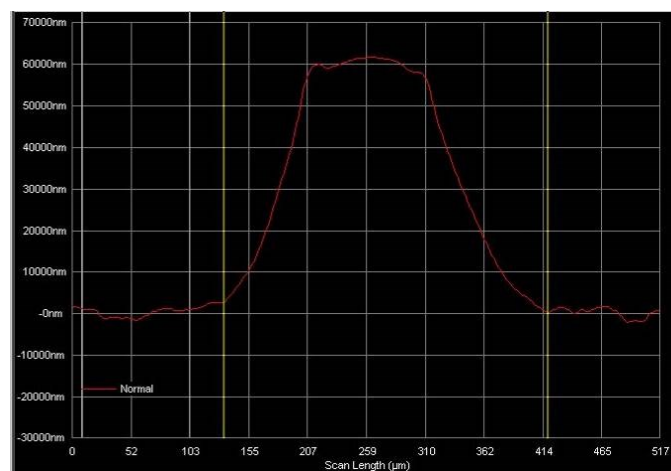
Figure 5.3 - Polymerized section profile analysed by profilometer

Polymerized lines maintain a shape similar to the dots. The average width and height values obtained are reported in Table 5.1, and distinguished between top and bottom zone. While the lines width is almost the same in each test, the total thickness increases in a non-linear way with the speed, passing from 80 μm at 2 m/s to about 100 μm at 0.5m/s.

Table 5.1 - Polymerized line test measurements

	Width and height average values		
	width up-zone [um]	width bottom-zone [um]	height [um]
Line 2	106	305	82
Line 3	99	276	86
Line 4	91	292	88
Line 5	84	271	96

Subsequently, the laser parameters were evaluated and tuned in order to avoid over-polymerization and under-polymerization areas and to ensure product homogeneity during all the printing phases.

5.2 Recoating process and blade optimization

As previously stated, in a SL apparatus the homogeneity and thickness of each liquid resin layer should be regulated with a moving blade, commonly called 'recoater'. Moreover, considering the photopolymer viscosity, it is not possible to guarantee a proper printing process without the use of a recoating system. Preliminary tests showed that during the printing process the resin flows above the previously printed layers creating a non-controlled coating with an uncertain thickness. In addition, considering the chemical-physical proprieties of the material which determine surface tension a convex meniscus is present on the solid printed structure. When irradiated by the laser source, the latter polymerizes maintaining its typical shape. This leads to a growth of the object with unwanted chamfers near the edges. Such a manufactured object couldn't be considered acceptable within a context such as mechanically assembled parts or any set of connectable components, as it has different dimensional tolerances from those defined during the design process. For those reasons, a blade was designed, fabricated and installed

on the system to accomplish the correct recoating. According with Renap and Kruth [41], a blade of 10 mm thickness was designed as visible in Figure 5.4.
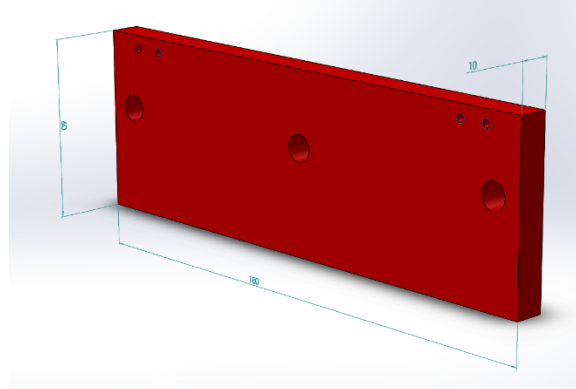
Figure 5.4 - Design of recoating blade according with Renap and Kruth, 1995

A blade width of 180 mm was established to cover almost all the working area width (192 mm). This size allows the resin to be removed during the blade action, assisting the flowing of the liquid towards the outer edges. This will be helped also by the holes on the working area, which are designed to allow the outflow of exceeding resin. A recoater height of 60 mm was used to make fixing on the support profile. In Figure 5.5 the final design of the recoating blade and relative support/movement mechanical parts are depicted.
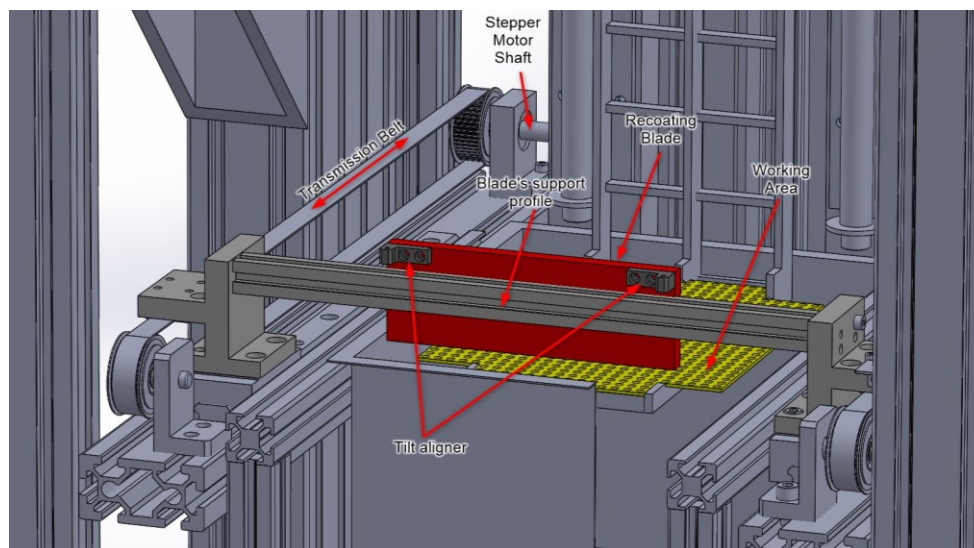
Figure 5.5 – Recoating blade design directly inside SLA CAD model. Z-axis moves the working area until in contact with the blade (0 position). Tilt alignment could be corrected through the use of two screws. Once this tuning is performed, a negative z displacement of 200 μm from the 0 position is set inside the software.

Figure 5.6 shows the different steps in a common recoating process.
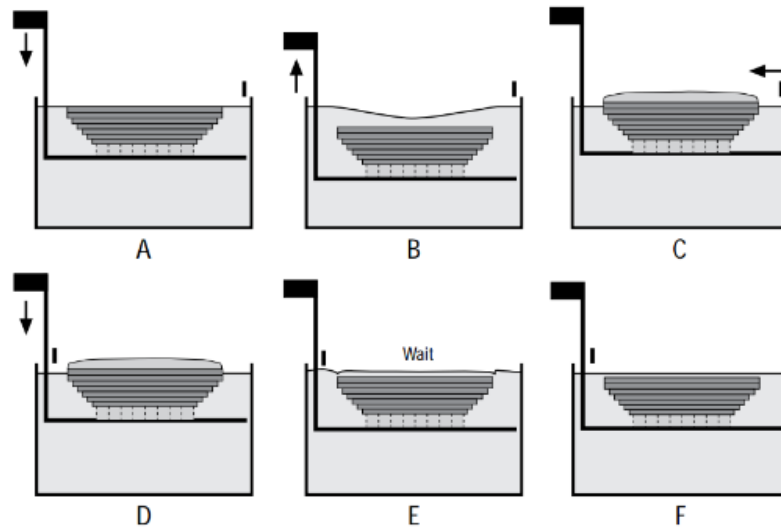
Figure 5.6 - Recoating phases

Figure 5.6 A shows the situation immediately after the polymerization of a layer. The upper surface is at the same height as the free resin surface. The goal is to reach the situation in Figure 5.6 F, in which the upper surface is covered with a liquid resin layer equal to the desired layer thickness. Considering the surface tension of the liquid resin, z-axis is moved downwards at more than one-layer thickness depth to make the resin flow over the part (Figure 5.6 B). Then, the z-axis moves up to bring the part slightly out of the resin (Figure 5.6 C). The recoating blade moves on the liquid layer with a certain gap from the top surface to remove all the excess resin and leave exactly one-layer thickness of resin on top of the part (Figure 5.6 D). Finally, a waiting time is imposed to make the resin settle before proceeding with layer polymerization.

In the process reported in Figure 5.6, the most important and determining step is surely the recoater movement. Indeed, if it results in an inaccurate liquid layer thickness, it will have consequences on the accuracy and quality of the entire part. The initial distance between the blade and the part was set as the double of the thickness of the desired layer following literature data [41], which affirms that to obtain a certain layer thickness the blade should be placed at the double of this value (Figure 5.7). Considering this data, a distance of 200 μm (Figure 5.5) was chosen to obtain a final layer thickness of 100 μm.
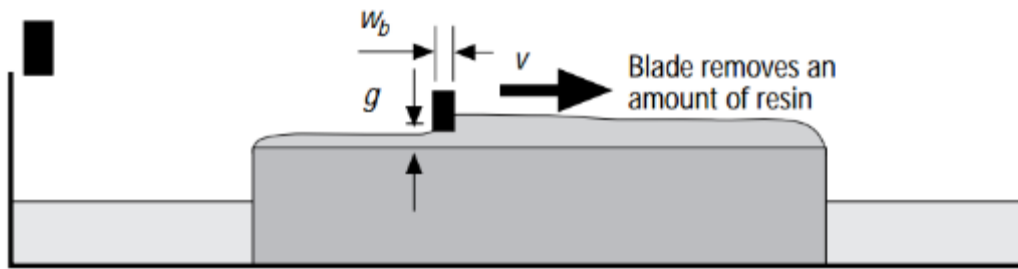
Figure 5.7 - Blade movement among resin

Unfortunately, as often happens, theory differs from reality. Indeed, some tests were performed following the previously mentioned rule with bad building results. For this reason, as visible in Figure 5.8 and Figure 5.9 a matrix of pads with increasing thickness was designed to investigate the effect of initial blade distance value on polymerized specimens.
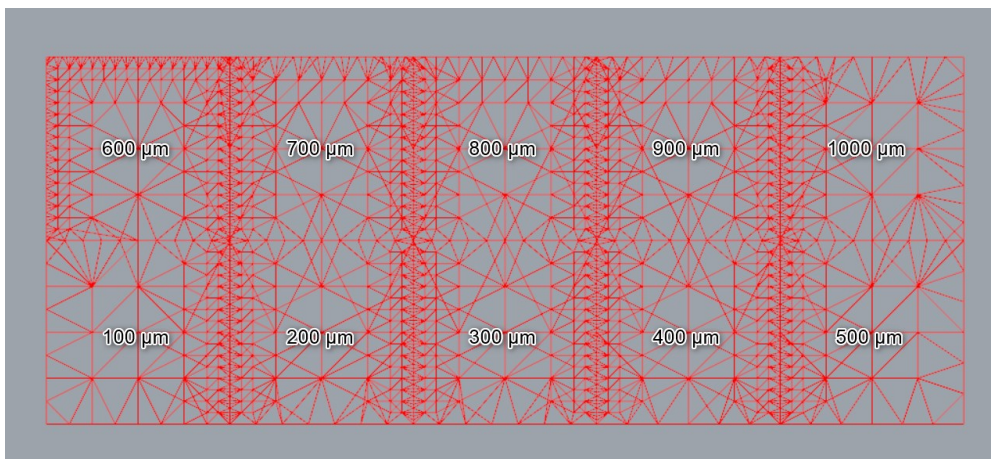
Figure 5.8 - Top view of the pads mesh with increasing thickness used for building tests. Each pad is 20 mm x 20 mm and thickness varies starting from 100 μm to 1000 μm.

Figure 5.9 - CAD model rendering with increasing thickness values

Different matrix structures were printed varying the blade distance at 200 μm, 180 μm and 100 μm. Once completed, each pad thickness was measured with a

Mitutoyo ID-C112CB (resolution 0.001 mm). As visible in Figure 5.10 decreasing the blade-part distance, there is an improvement of the layer thickness. The most interesting result is obtained when the blade distance is 100 μm. For this reason, the initial distance between the blade and the part was modified not in accordance with literature data and set to 100 μm.
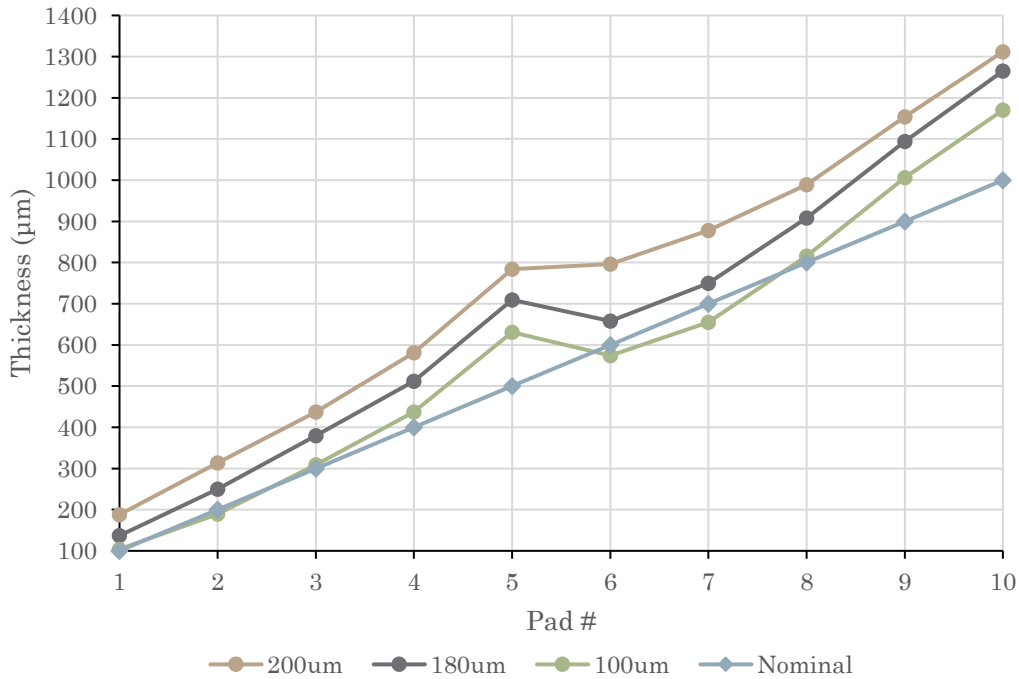
Figure 5.10 – Influence of various blade distance values on specimen pad thickness. The Nominal line represent the thickness value that each pad should have. Other lines represent the measured thickness of each pad obtained with blade distance values of 100 μm, 180 μm and 200 μm.

Comparing the thickness values obtained and the pads position in Line 1 and Line 2 in Figure 5.9, an increasing offset tendency starting from pad with the lower thickness (for each line) to the higher one is visible. Multiple factors should be considered to explain this trend. Starting from the *.stl model, adjacency of each pad to each other can influence the resin flow movements during the recoating and subsequent blade scraping processes. Moreover, exceeding or missing amount of resin could affect the total thickness of each pad. The building strategy should also be considered. The building process can be influenced printing the specimen perpendicularly or parallelly to the blade direction. Also hatching strategy could have an influence. Laser hatching direction can increase or decrease surface tension effects as it acts like a moving dike during the scanning process. After this test, an object with a much higher thickness was printed: a cube with 7.5 mm height. Setting

the blade distance value at 100 μm we obtained a small offset of 550 μm from the nominal value at the end of the building process.

At the end it is possible to state that, with SL technology, an error on nominal thickness is always present. Unfortunately, a general rule cannot be defined, since the error depends not only on the printing parameters, but also on the object geometry, orientation and the material used. Moreover, also the printing area could affect the behaviour of the liquid resin and settling, thus generating a further source of inaccuracy and error.

5.3 Resin level sensor

Along with a recoating system during printing phase, a resin level control system was also included, integrating a Keyence Proximity Sensor model FU-93 (Figure 5.11).
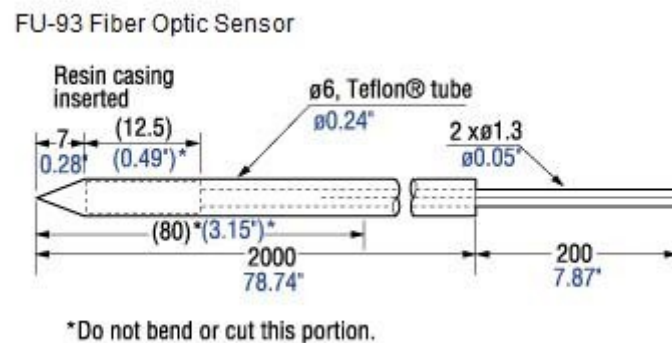
Figure 5.11 - Fiber Optic sensor mechanical data

The Keyence sensor is based on refractive index measurement by means of an optical fibre. The tip, which is the sensing probe, is installed vertically inside the vat; depending on the amount of tip dipped inside the resin, the sensor returns a value on a small alphanumeric screen. Once the resin level is appropriate to establish the desired layer thickness on the printing platform, the sensor value is set as reference. Each time the vat needs to be refilled, an amount of resin should be added so that the same reference value is red on the sensor screen. Indeed, the component printing by additive manufacturing results in a reduction of liquid inside the vat, in amount equal to the total volume of the component built. The introduced control system allows to restart a new printing process with a desired volume of

resin, accordingly with the machine prototype characteristics. In Figure 5.12 the optical sensor integration inside the SLA machine is depicted.
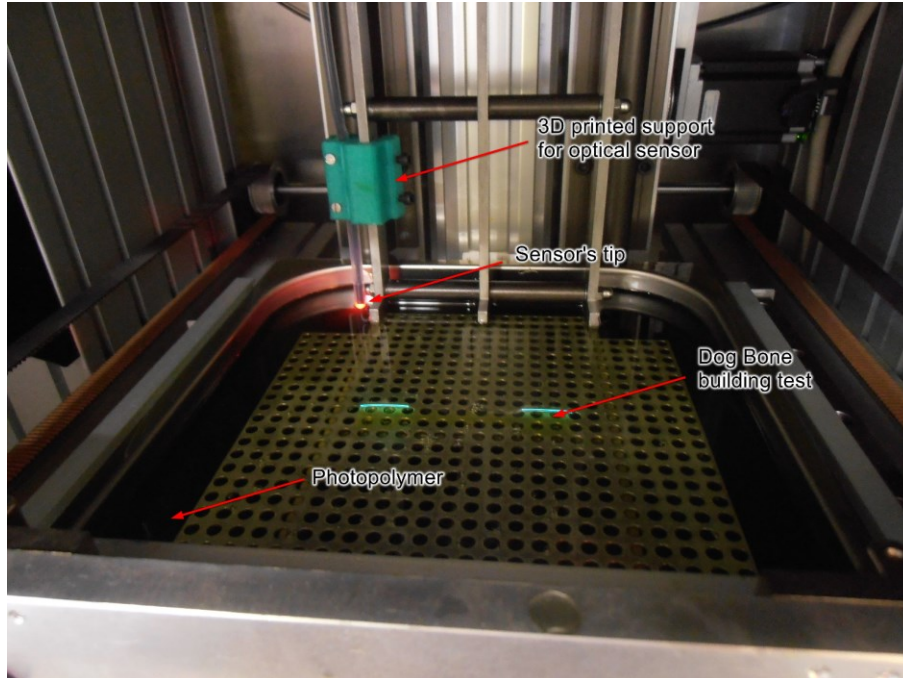
**Figure 5.12 - Resin level sensor installed inside SLA Machine. Each time a new building process is started, z stages move the working area at the focusing point.
In this condition resin level is evaluated by sensor.**

5.4 Repeatability tests

Several components were printed with the aim to analyse the resin intrinsic characteristic influence and to evaluate the printing machine working behaviour. A classic dog bone shape *.stl model was designed (Figure 5.13).
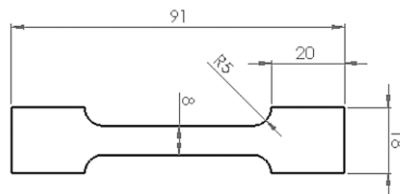
Figure 5.13 - Dog bone nominal values. Total thickness is equal to 4 mm.

The printing process was carried out using the same parameters for each printed object, evaluating the repeatability of the process. In Figure 5.14 the printed geometry.

Figure 5.14 – Dog bone top and bottom view after printing process

Each dog bone was printed directly on the working area, without the use of building support. The bottom view (Figure 5.14) shows the defects due to this building strategy. Indeed, when the building process starts, the laser polymerizes correctly the first layer. Partially also the photopolymer volume present inside the platform holes, innerly the object scanning perimeter, will be polymerized. A fixed laser power of 30 mW was set for each sample. Regarding hatch spacing and layer thickness, the work of Cho et al. [42] was considered. In Figure 5.15 is visible that error increase proportionally with the increasing of layer thickness and decreasing of hatch spacing.
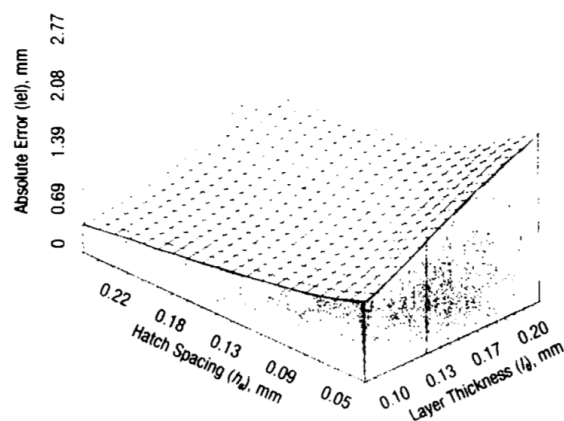
Figure 5.15 - Error estimation with respect to process parameters [42]

A layer thickness of 0.1 mm and a hatch spacing of 0.05 mm was set to minimize the error and give a mechanical consistency to each dog bone. This will compensate

the error introduced by the hatch spacing value chosen to give mechanical strength to the specimen. Table 5.2 reports all the parameters set for each sample.

Table 5.2- Dog Bone building parameters

Parameter	Value
Layer Thickness	0.1 mm
Hatch Spacing	0.05 mm
Laser Power	30 mW
Outline Marking Speed	1000 mm/s
Hatching Marking Speed	2000 mm/s

The photopolymer is an acrylate compound identified with the commercial name 'Standard Blend-Black' (Fun to Do). Only viscosity and density values are available from the producer as visible in Table 5.3.

Table 5.3 - Standard Blend-Black Properties

Property	Value
Viscosity [cP]	100
Density [g/dm³]	1016

In Figure 5.16, the flowchart presents the building of a single layer, starting from the marking process (1), the recoating phase (2), the action of the blade (3,4), the resin levelling (5) and again the printing process.
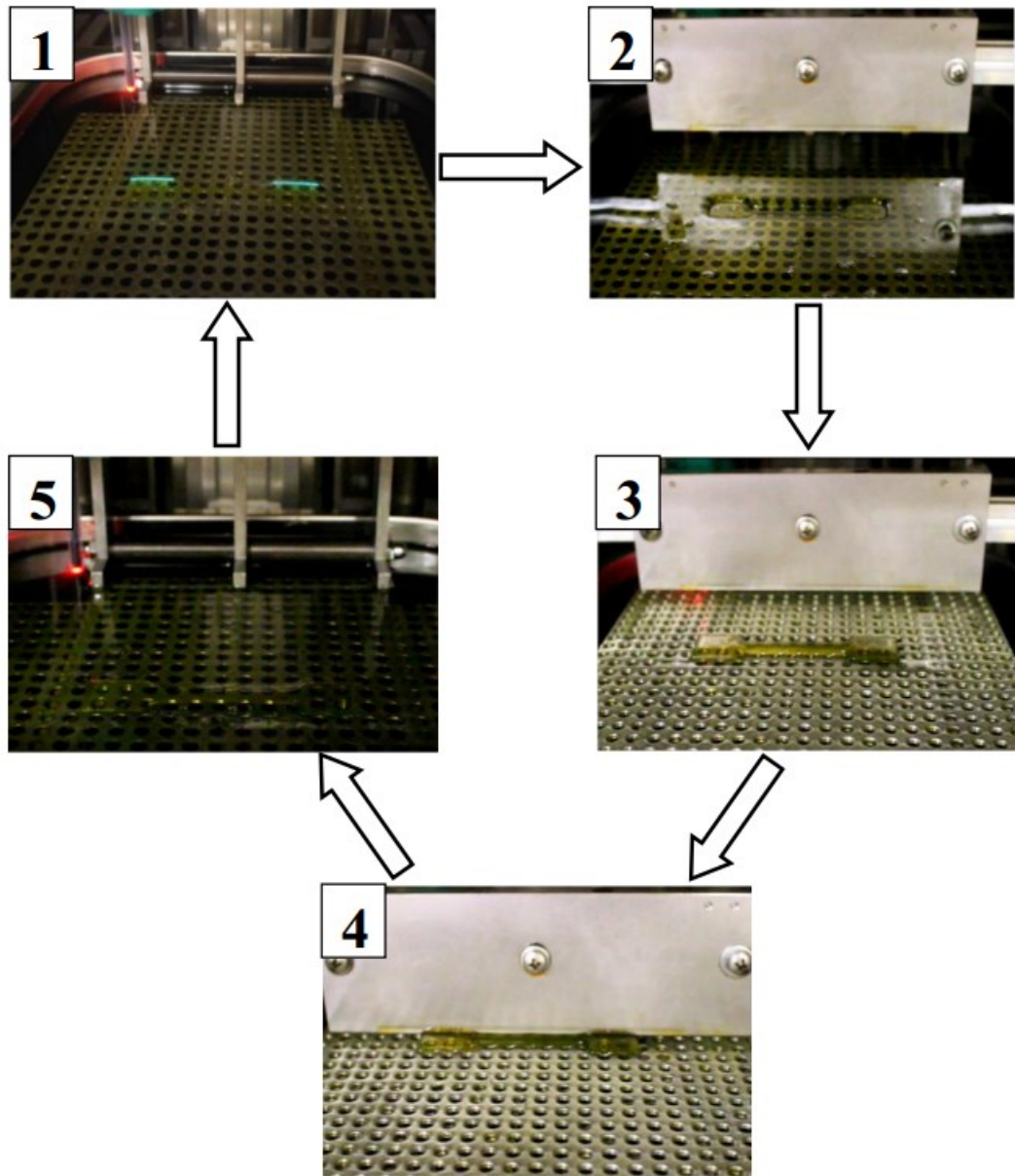
Figure 5.16 – Dog bone layer building sequence

Different measurements were evaluated during the dog bone printing tests, comparing them with CAD reference values. As visible in Figure 5.17 a series of defects are present on specimens. Considering that each sample is printed and then manually detached from the working area, some layers on the bottom could be damaged or lost. These traces could be present in the specimen bottom surface (Figure 5.17a). Shrinkage effect could be present causing the components bending along the x and y direction (Figure 5.17b). Furthermore, surface tension during the

building process could cause a convex top surface (Figure 5.17c). Each of these factors could affect sample measurements.
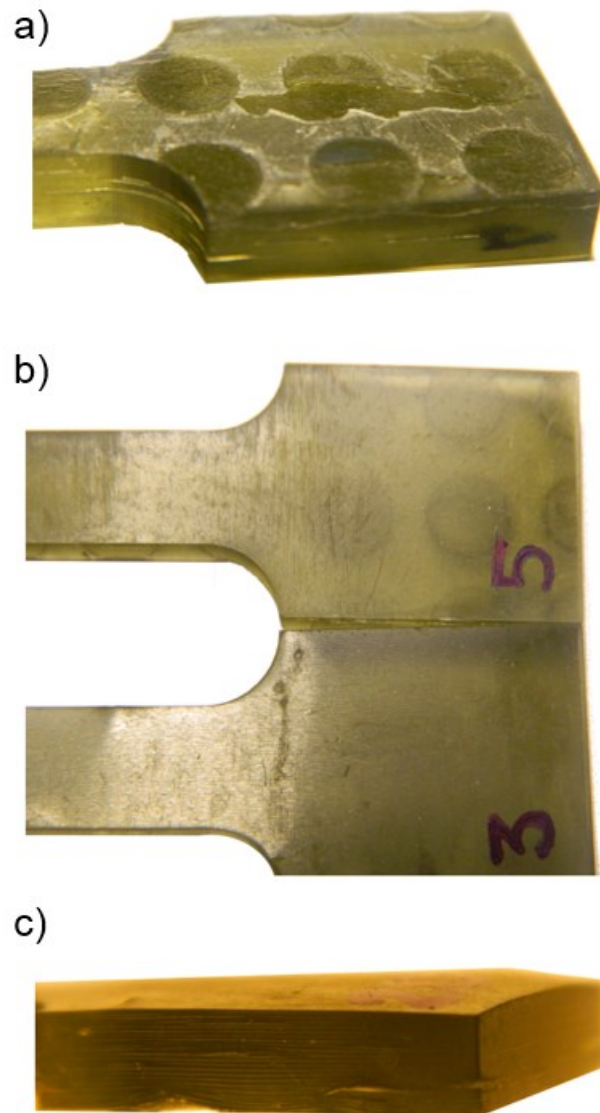
Figure 5.17 - Printing defects of specimens a) residues on the specimen bottom part b) deflection due to shrinkage c) convex surface due to surface tension effects

The Mitutoyo ID-C112CB (resolution of 0.01mm) was used to analyse the produced samples. Five different thickness and width measurements was performed on each sample and are depicted in Figure 5.18.
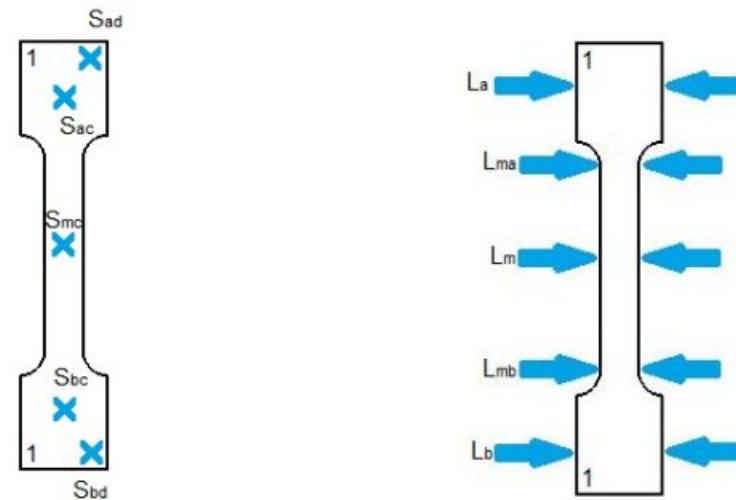
Figure 5.18 – Dog bone measurement points

Sad = Top Right Thickness;   La = Top Width;
Sac = Top Centre Thickness;   Lma = Top Curvature Width;
Smc = Sample Centre Thickness;   Lm = Centre Width;
Sbc = Bottom Centre Thickness;   Lmb = Bottom Curvature Width;
Sbd = Bottom Right Thickness;   Lb = Bottom Width.

All the measurements performed are reported in Table 5.4 and are expressed in mm.

Table 5.4- Dog bone measurement values

sample #	S_{ad}	S_{ac}	S_{mc}	S_{bc}	S_{bd}	L_a	L_{ma}	L_m	L_{mb}	L_b
1	4.40	4.46	3.84	3.95	4.02	17.56	7.94	8.02	7.92	17.57
2	4.46	4.35	4.32	4.67	4.59	17.52	7.89	7.95	7.91	17.55
3	4.29	4.39	4.17	4.26	4.37	17.61	7.92	7.94	7.94	17.57
4	4.45	4.68	4.35	4.45	4.29	17.54	8.00	7.93	7.89	17.56
5	4.14	4.40	4.17	4.27	3.96	17.59	7.94	7.97	7.99	17.66
6	4.35	4.46	4.31	4.66	4.56	17.61	7.95	7.94	7.91	17.61
7	4.16	4.33	4.17	4.71	4.36	17.73	8.00	8.00	7.97	17.67
8	4.53	4.77	4.31	4.61	4.35	17.63	7.95	7.95	7.93	17.61
9	4.40	4.30	4.32	4.69	4.59	17.62	7.93	7.93	7.93	17.63
10	4.11	4.60	4.23	4.41	4.06	17.63	7.93	7.92	7.93	17.62
11	4.78	4.72	4.61	4.67	4.45	17.47	7.78	7.87	7.88	17.57
12	4.48	4.64	4.67	4.70	4.72	17.55	7.82	7.86	7.90	17.57

13	4.28	4.60	4.53	4.70	4.77	17.66	7.83	7.96	7.95	17.66
14	4.28	4.59	4.54	4.74	4.77	17.55	7.90	7.92	7.91	17.57
15	4.77	4.67	4.37	4.50	4.35	17.68	7.96	7.97	7.84	17.66
16	4.41	4.59	4.52	4.67	4.66	17.57	7.92	7.93	7.94	17.56
17	4.60	4.75	4.36	4.52	4.30	17.64	7.97	7.95	7.84	17.64
18	4.68	4.85	4.48	4.58	4.32	17.51	7.86	7.86	7.90	17.59
19	4.83	4.67	4.98	4.52	4.34	17.52	7.91	7.92	7.79	17.52
20	4.46	4.88	4.86	5.10	4.96	17.57	7.89	7.88	7.90	17.52

Table 5.4 shows that samples measurements are quite different from nominal dimension but building errors are of micrometric entity. Three types of histograms are reported: Histogram 5.1 related to all the thickness measurements, Histogram 5.2 including La and Lb measurements and Histogram 5.3 related to Lma, Lm and Lmb measurements.
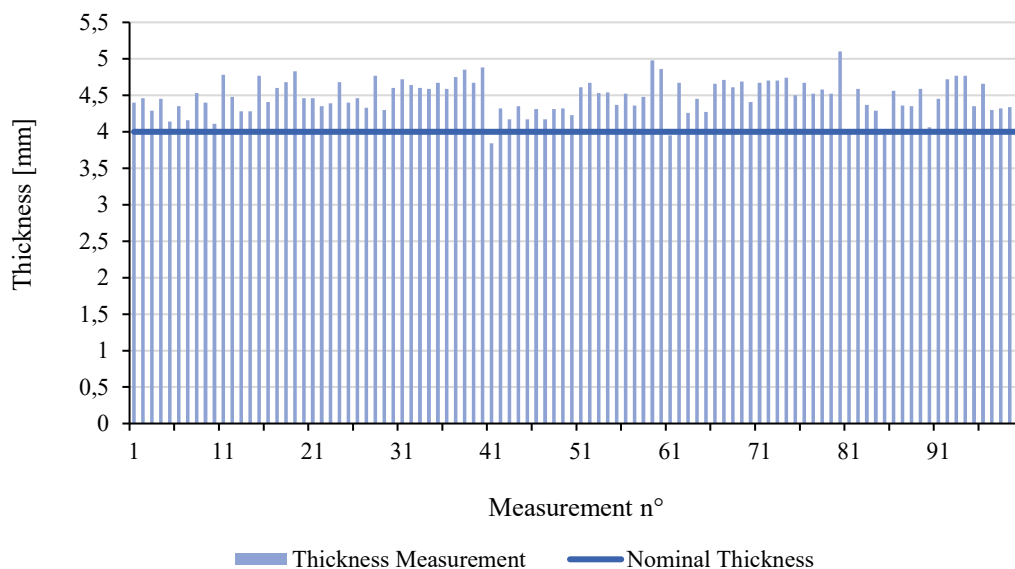
Histogram 5.1 – 100 thickness measurement performed on 20 dog bone specimens.
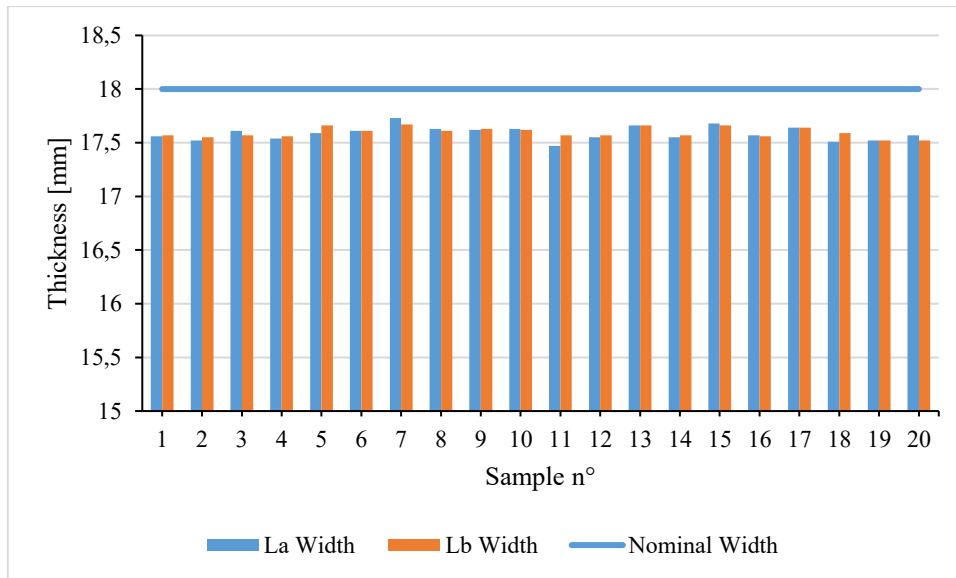
Histogram 5.2 - La and Lb Width measurement performed on 20 printed Dog bone

Histogram 5.3 - Lma, Lm and Lmb Width measurement performed on 20 printed Dog bone

From Histogram 5.1, Histogram 5.2 and Histogram 5.3, the detected thickness values are subject to greater variability then the width values: the thickness values variability can be caused by phenomena that influence the accuracy in the vertical

direction [43], by building and hatching strategy and also by polymerization residues presence on the bottom specimens surface, due to working area holes.

5.5 Automatic support generation

During the 3D fabrication process, object with complex shapes needs to be printed with some supporting structures. Differently from other additive techniques, in which the material itself acts as a support (ex. Selective Laser Sintering), in the SLA process the polymer is not able to support structures during the printing phase. Depending on the object geometry, support might be added to avoid printing failure. First, support generation was performed automatically through the use of commercial software, varying the type, shape, and size, and evaluating their behaviour during the printing process. Subsequently, for a greater process control, supports were manually created or modified to reduce their invasiveness and to simplify the detachment from the printed object. In detail, a plug-in was developed in Grasshopper, a McNeel Rhinoceros add-on for parametric CAD designing (Figure 5.19 depicts the visual-code of the support creation plug-in).
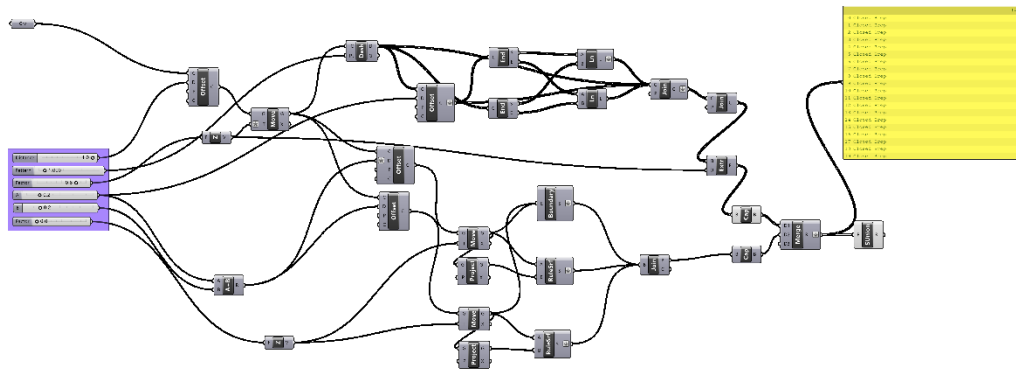
Figure 5.19 - Grasshopper parametric and automatic support generation visual-code.

The plug-in, starting from a CAD model, allows the automatic generation of support structures along a curve that follows the object perimeter. A NURBS (Non-Uniform Rational Basis-Splines) model of the geometry to be supported is required, and the user has to select an outline or a surface border to make the plug-in work properly. It is well visible in Figure 5.20 the ability of the plug-in to create both the base and the support structures accordingly with CAD shape and inclination.
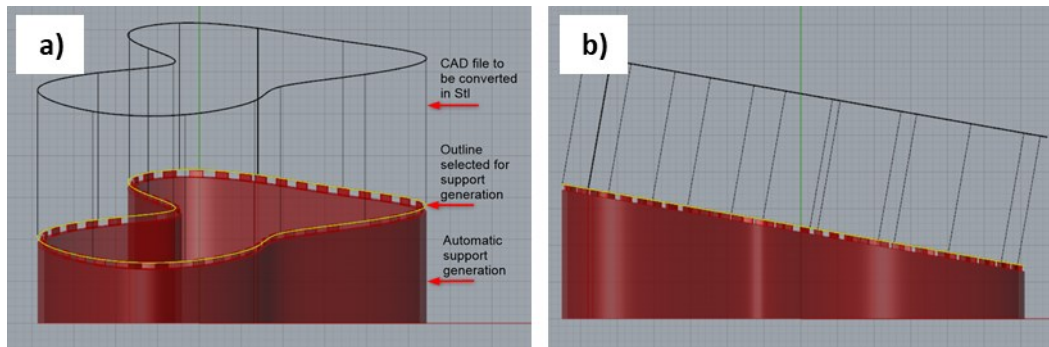
Figure 5.20 - Automatic adaptive support generation following user outline selection. a) front view evidencing the selected outline. B) Right view evidencing CAD inclination.

The number of contact points could be increased or decreased as well as the overall offset from the selected outline. Multiple lines could be selected to have more support structures which are available in two different shapes, as visible in Figure 5.21.
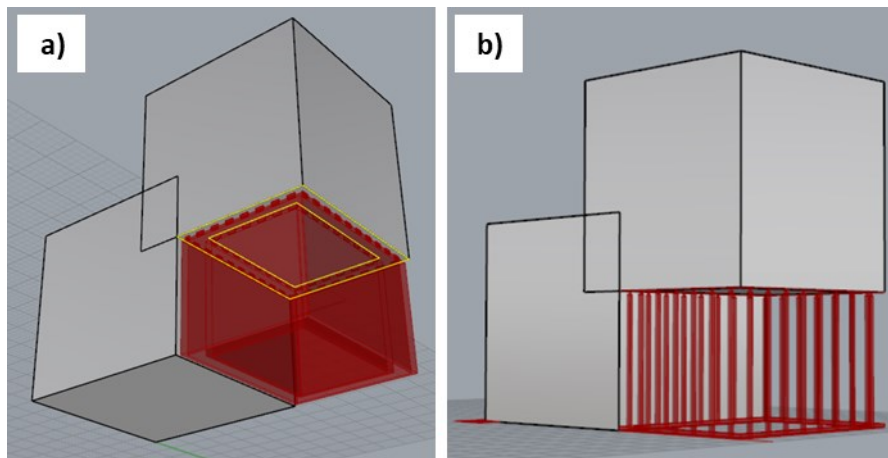
Figure 5.21 - a) multiple lines selection for support generation b) example of pillars automatically generated

In addition, a component like in Figure 5.22 was built to validate the correct support generation and printing process. As visible, the object was correctly build and is properly anchored to the building platform.
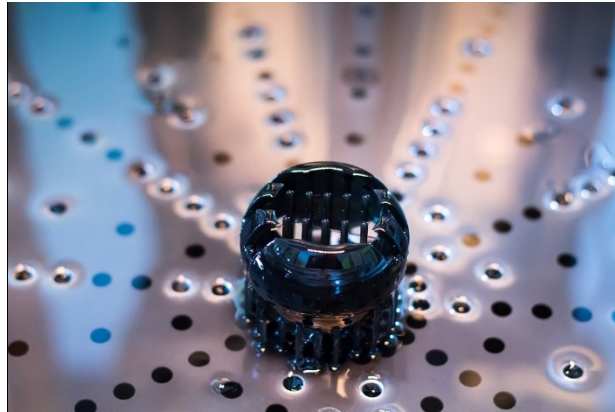
Figure 5.22 - Stereolithography printed samples

5.6 SLA Application activities

With High Performance Manufacturing as keyword of PhD activity, the printing process optimization was only one of the considered aspects. Indeed, since the additive manufacturing future development relies on the research of new smart materials, part of the work was devoted to the study of resins with intrinsic features that can give a concrete function to the printed objects.

5.6.1 Conductive Polymers building tests

A study about material functionalisation was led on commercial polymers trying to make them "active" and suitable for current routing. Polymers are by nature insulators and can be converted in conductors by, for example, adding a filler. When using a filler, percolation threshold (p_c) is a fundamental aspect for the polymer composites to be conductive. The percolation threshold is reached when the filler amount is enough to create a conductive path through the polymer (Figure 5.23). With a so-functionalised resin, miniaturized printed circuits could be embedded within the three-dimensional printed object, thus obtaining a non-removable and durable active circuit. Carbon Nano Tubes (CNTs) are a variety of conductive fillers which can be used in a polymer matrix.
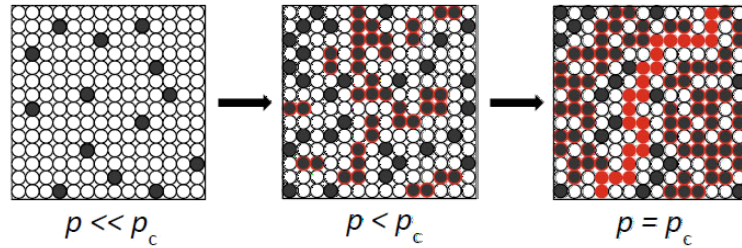
Figure 5.23 - Polymer functionalization. When filler concentration (p) is lower than percolation threshold (p_c), the polymer matrix is not conductive. When p reaches the p_c a conductive polymer matrix is obtained.

Various printing tests, in collaboration with Polytechnic of Turin, were performed to print CNTs resins with the SLA printing machine. Candidate's contribution to the research activity, performed by Gonzales et al. [38], was to verify the printability of CNTs polymer matrices created at Polytechnic of Turin. The following monomers were used: poly(-ethylene glycol) diacrylate (PEGDA, average Mn = 500 g/mol) and poly(ethylene glycol) methyl ether methacrylate (PEGMEMA, average Mn ¼ 500 g/mol). The photoinitiator used was bis(2,4,6-trimethylbenzoyl)-phosphineoxide (BAPO) and the carbonaceous filler used was Multi-Walled Carbon Nanotubes (CNTs) NC3100.

The available photocurable formulations were evaluated in terms of light power, CNTs and photo-initiator quantity, formulation shelf-stability and printability. As visible in Table 5.5, the viscosity increases with increasing CNTs content (expressed in wt% on the matrix mass) due to CNTs interaction with polymeric chains. Unfortunately, an excessive viscosity could lead to printing failure with SLA technology. For this reason, the viscosity was decreased by adding reactive diluents (PEGMEMA).

Table 5.5 - Viscosity values at 25°C for pristine PEGDA printable formulations and for PEG-DA_PEGMEMA 1:1.5 printable formulations at a shear rate of 1 s^{-1}

	Viscosity (Pa·s)	
Formulations	Pristine PEGDA	PEGDA:PEGMEMA 1:1.5
0.0 wt % CNTs	0.031	0.015
0.1 wt % CNTs	2.770	0.773
0.3 wt % CNTs	25.300	11.500
0.5 wt % CNTs	84.600	36.600
1.0 wt % CNTs	1189.000	609.000
1.5 wt % CNTs	2010.000	1370.000

Real-Time FT-IR analyses were performed in transmission mode using the spectrophotometer from Thermo Electron Corporation. The conversion of acrylate double bonds was calculated by following the decrease of the peak area of C=C group at 1640 cm^{-1} and normalized with the peak area of C=O group at 1730 cm^{-1}, during irradiation with a portable laser at 405 nm and at light power of 45 mW/cm^2. Results are visible in Figure 5.24. Unfortunately, it is evident that by increasing the CNTs content there is an important decrease on both acrylic double bond conversion and rate of photopolymerization.
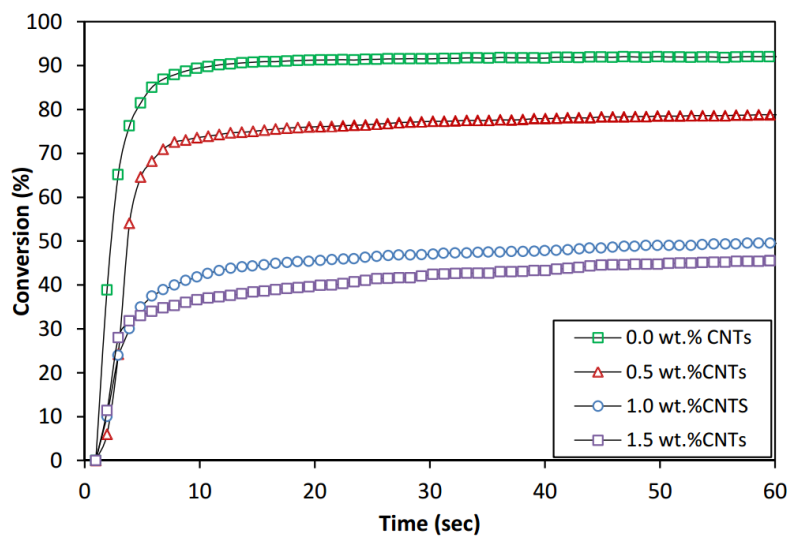
Figure 5.24 - Conversion curves as a function of irradiation time for PEGDA:PEGMEMA 1:1.5 wt/wt containing 0, 0.5, 1 and 1.5 wt% of CNTs. BAPO content 3 wt %, film thickness 50 mm, irradiation power 45 mW/cm2 (405 nm).

As predictable from FT-IR analysis, the SLA printing tests provide adequate results only for 0.1 wt% CNTs polymer matrix. As visible in Figure 5.25 the compound printability decreases proportionally with the increase of CNTs concentration.
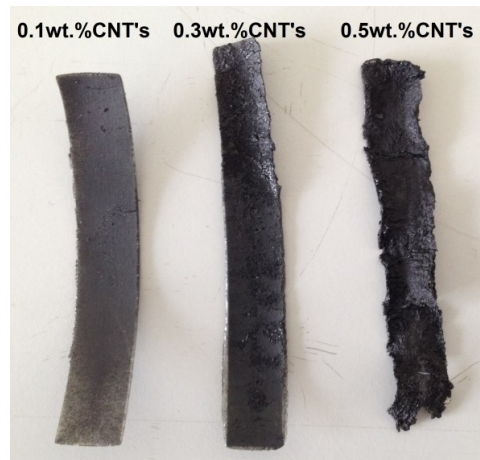
Figure 5.25 - Different CNTs concentration building test performed with SLA printing machine. PEGDA:PEGMEMA 1:1.5 wt/wt containing 0.1, 0.3 and 0.5 wt% of CNTs. BAPO content 3 wt %, film thickness 100 μm, laser power 120mW and scanning speed of 1mm/s.

For this reason, complex conductive structures were printed only with the 0.1% CNTs filled photopolymer, as visible in Figure 5.26. Conductivity/resistivity test were performed by other research members and are reported in the paper by Gonzales et al. [38].
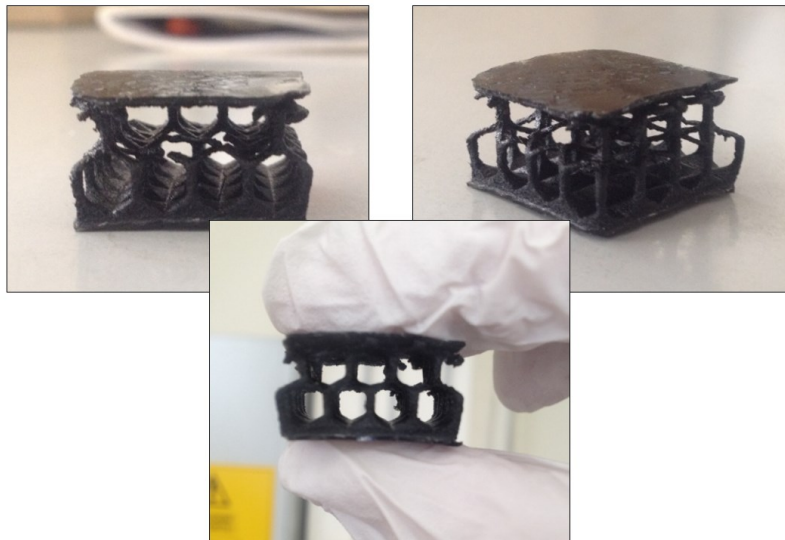
Figure 5.26 - 3D printed object made with 0.1 wt.% CNTs filled polymer. BAPO content 3 wt.%, layer thickness 100 μm, laser power 120 mW and scanning speed of 1 mm/s.

Chapter 6

6 Additive Manufacturing at the sub-micrometric scale

6.1 Two Photon Polymerization for μ-Filtering devices

In this PhD thesis, the manufacturing at the sub-micron scale and the integration of Nano&Micro Additive Manufacturing processes were studied. This research activity was made possible thanks to the precious scientific collaboration with Laser Zentrum Hannover (LZH) – Germany. In detail, the integration of micro-/nano-filtering structures in a fully 3D printed microfluidic channel, which is still a challenging topic in the field of Lab-on-a-Chip for diagnostics, was carried out with the aid of Two Photon Polymerization (2PP) technique.

As for bigger prototypes, 3D printing represents a powerful tool to obtain complete devices ready to be tested also in the world of milli-/micro- fluidics. The relative AM low cost processes, compared to injection molding processes or clean room replica molds, define this technique a valid alternative for microfluidic research activity and R&D applications. In the last years the resolution drawbacks related to AM processes were considerably improved thanks to the next generation of two photons 3D printers. 2PP is today employed as additive manufacturing technique for micro-/nano- engineering. Unfortunately, due to its high resolution, the printing volume is limited to few mm^3 and printing times are not negligible. For this reason, 2PP technique needs to be integrated with other technologies to build bigger objects that requires embedded micro-/nano- features.

In this work, different suspended filtering structures were directly 2PP printed inside SLA printed microchannels. The assemblies were also tested with a particle track experiment to verify the efficiency of the printed filtering structures.

The microchannels were fabricated by the SLA printer described in Section 4.3 using a commercial resin, while the suspended filter was obtained with the LZH 2PP Micro-3-Dimensional Structuring System (M3D) (Figure 6.1) using a drop of Femtobond D resin.
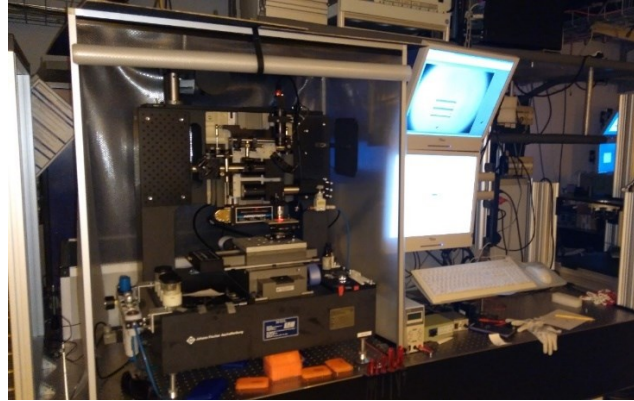
Figure 6.1 - 2PP Micro-3-Dimensional Structuring System (M3D)

The 2PP system laser source was a TOPAG Flint laser with a wavelength of 518 nm, a pulse width of 150 fs and a repetition rate of 75.6 MHz. A Zeiss 50x 0.75 NA, EC Epiplan Objective was used. The optical path simplified scheme is reported in Figure 6.2, where also the XY polymerized voxel dimension, for each objective available, is visible.

Objective	Voxel size (um)
20x	0.5
50x	0.3
100x	0.1
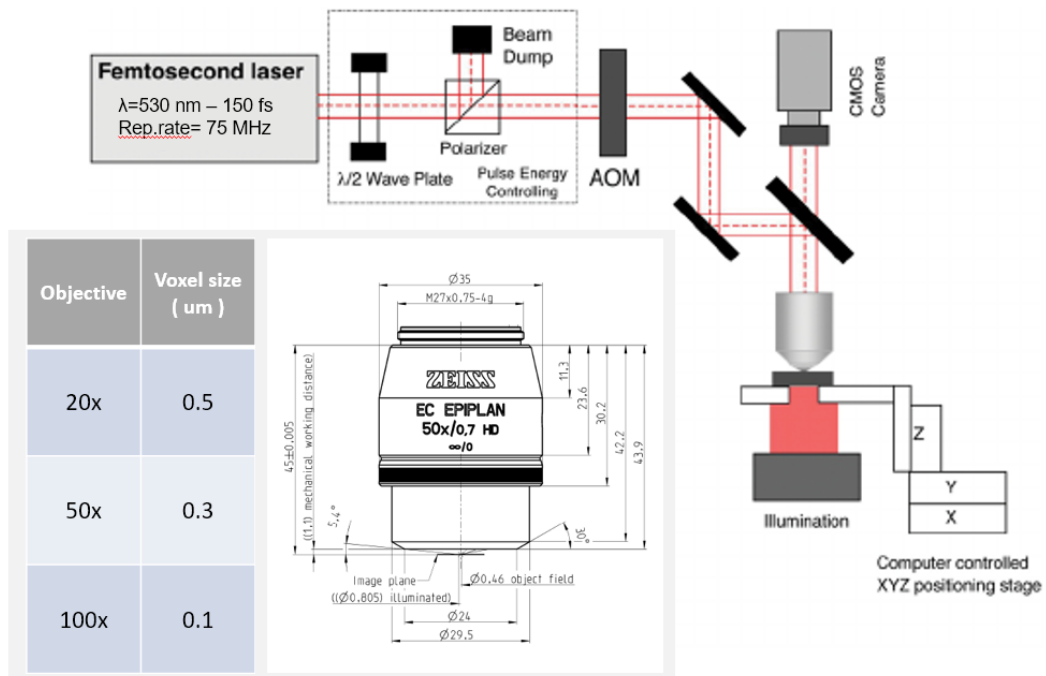
Figure 6.2 - 2PP simplified optical path and objective mechanical data. Polymerizable voxel size dimension in XY are visible in correspondence of each available objective.

Initially, the Proof of Concept (PoC) was similar to a sandwich-like device composed by a SLA 3D printed microfluidic chamber enclosed by two sheets of PMMA. Two holes were used as inlet and outlet, in accordance with microchannel geometry. The filtering structure should have been built with 2PP directly in the middle of the chamber (Figure 6.3).
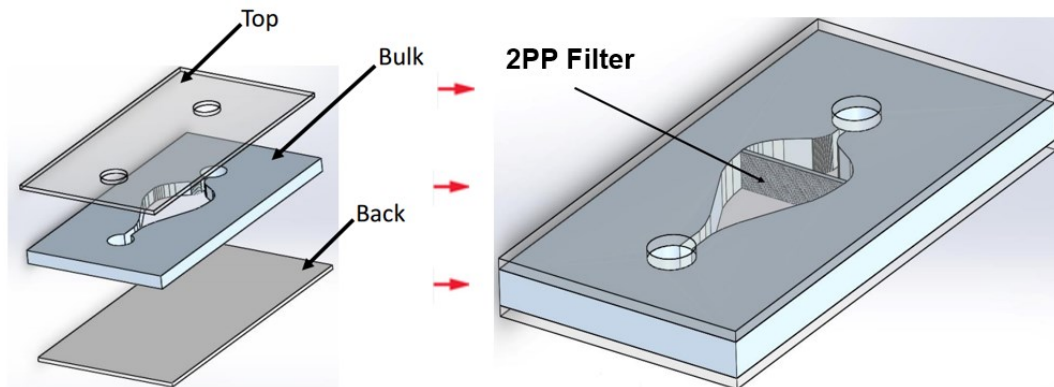
Figure 6.3 - Filtering device Proof of Concept

6.2 Process Introduction

As previously stated, the work on 2PP printing was devoted to the integration of a filter, composed by nanometric structures, inside an existing microfluidic device. So, the presented filters were designed not only respecting the 2PP technology limits, but also the SLA microfluidic channels constraints.

As for each Additive Manufacturing process, an *.stl file of the filter was generated after the CAD design with a proper software. The geometry was then sliced and finally printed. For each printing process, the SLA printed microchannels were taped on a glass substrate and a single 1.5 mm diameter resin compound drop, optimized for 2PP processes (FemtoBond), was used (Figure 6.4).
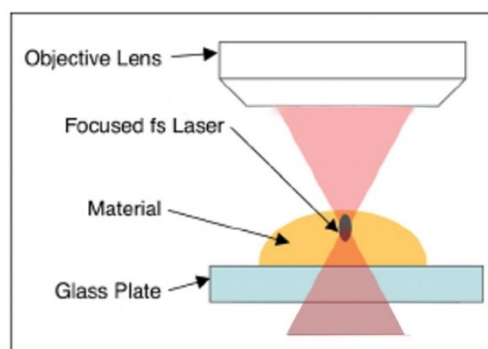
Figure 6.4 - Focused beam on Femtobond resin drop

Once the printing process was completed, the sample followed a "developing" process. This step requires the sample to be dipped in 1-Propanol for a period between 30 minutes to 24 hours, depending on the overall filter printed pores dimension, allowing the pores cleaning from the unpolymerized resin residues. A fast-further cleaning process in Ethanol is performed to introduce the sample to the drying process. Two drying procedures are available depending on the printed structure. If filter includes geometries in the order of tens of microns, the air drying could be performed. Otherwise, when the porosity size is of few microns, the critical point drying (CPD) is required.

The procedure of critical point drying is an efficient method for drying delicate samples from water and ethanol, that may collapse due to the presence of high surface tension during solvent evaporation. Moreover, the presence of water and ethanol molecules at the same time in the sample disturbs the vacuum process affecting the overall SEM image quality. Crossing the interfaces from liquid to gaseous phase during evaporation (air drying) the tangential forces caused by the surface tension can influence the nano- and micro- structures of the specimen. To preserve sample morphology, CPD is the state of the art method. At the critical point, physical characteristics of liquid and gases are not distinguishable. Compounds which are in the critical point can be converted into the liquid or gaseous phase without crossing the interfaces between liquid and gaseous, avoiding the damaging effects. The dehydration of the samples using the critical point of water is not feasible since it lies at 374 °C and 229 bar where any sample would be destroyed. To overcome this problem, water can be replaced against liquid carbon dioxide (CO_2), whose critical point lies at 31 °C and 74 bar and is more appropriate for all biological applications and technically relative easy to maintain. However, CO_2 has one serious disadvantage as transitional fluid: it is not miscible with water. Therefore, water must be replaced by exchange fluids like ethanol or acetone which are miscible in both water and liquid CO_2. Both exchange fluids cannot be used for critical point drying due to their high critical point temperatures (Ethanol critical pressure (P_c) = 60 bar, critical temperature (T_c) = 241 °C; Acetone P_c = 46 bar, T_c = 235 °C). After replacing water with an exchange fluid in a pre-critical point drying step, and in turn replacing this exchange fluid with liquid CO_2, the liquid CO_2 is brought to its critical point and then converted to the gaseous phase by decreasing the pressure at constant critical point temperature. For CPD processing a LEICA EM CPD300 was used.

Once the sample is dry, a gold sputtering process could be performed to improve SEM analysis results (FEI Quanta 400 FEG). A scheme reassuming the developing process is visible in Figure 6.5.
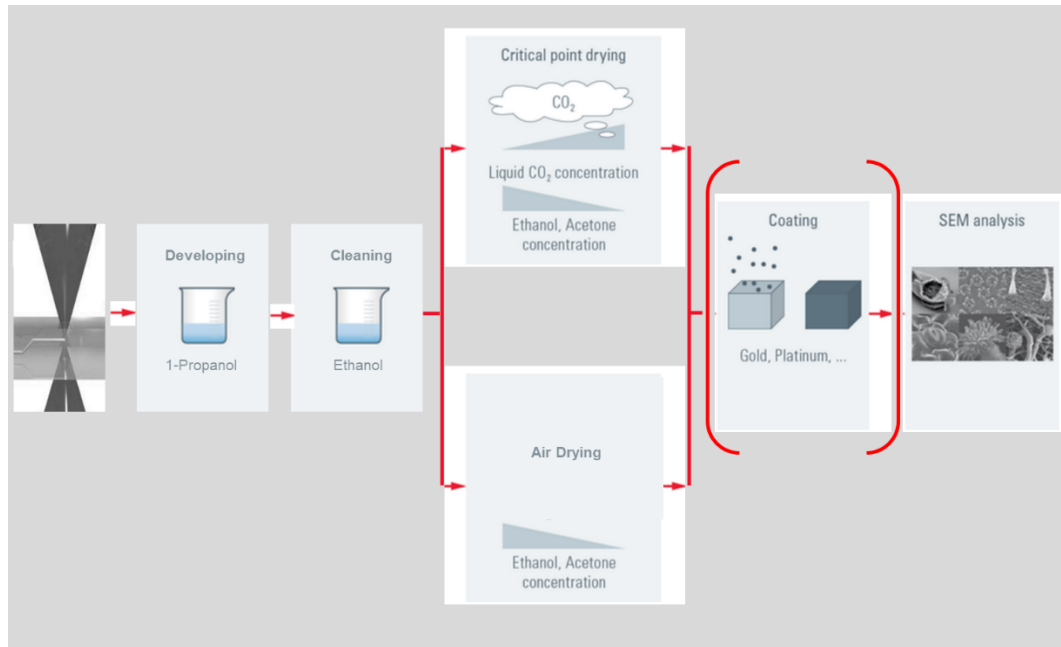
Figure 6.5 - 2PP printing, developing and analysis sequence.

The gold sputtering was performed during all the printing parameters research activity to increase the imaging resolution and retrieve better information. Unfortunately, the gold sputtering process could be considered as a disruptive process when a functional filtering device is required. The evaporated gold reaches and obstructs all the pores, making the filtering unit inoperative for further tests. Otherwise, if a sample needs to be preserved for subsequent tests, low vacuum SEM analysis can be performed on specimens, since it doesn't require sputtering pre-processing. So, a ZEISS Axiotech Vario microscope was used for a visive pre-analysis: if the 2PP structure was acceptable and well-integrated inside the microchannel, the sputtering process was avoided to preserve the sample as functional for future fluidic tests.

6.3 Building Parameters

A series of tests, using various kinds of photopolymers, were performed to obtain the correct building parameters. A small box, useful to simulate 4 filtering pores, was designed (Figure 6.6) and realized recursively, varying the marking speed and the laser power.
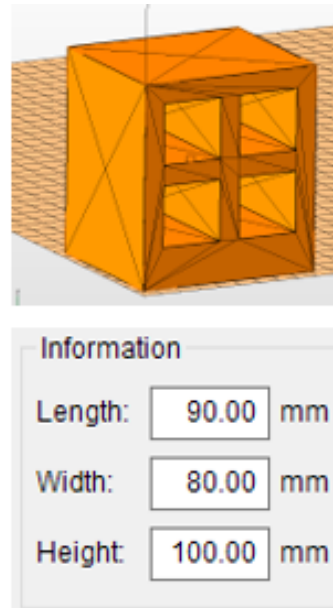
Figure 6.6 - CAD design to find 2PP parameters.
(Information are reported in mm because the printing software automatically converts stl models in µm)

The influence of printing parameters on the final pores neatness was investigated. As declared before, the cleanliness is influenced by the developing and drying process. Nevertheless, incorrect printing parameters could cause over-polymerization effects until the pores clogging. These effects are visible in Figure 6.7 in which pores are almost closed. Figure 6.7 shows also that over-polymerization effects, due to incorrect parameters, are mainly along z direction. As visible in Figure 3.17, a cured line is assimilable to a parabola in which the x and y dimensions are influenced mainly by the laser spot diameter. The spot depends on the optical proprieties of each component used to build the optical path (e.g. objective focal length and numerical aperture). The curing depth C_d, instead, depends mainly on laser power and scanning speed as visible in Equation 3.9. For these reasons, wrong laser parameters introduce a lack of resolution mainly along the z direction while x and y directions are less influenced.
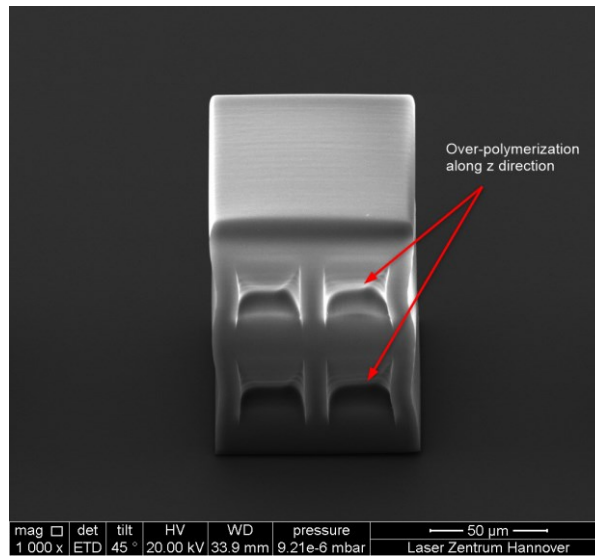
Figure 6.7 – Over-polymerization effects due to wrong speed/laser settings

The best result was obtained with 2 mm/s scanning speed and a power between 35 mW and 45 mW. A slicing of 3, 5, and 7 µm was tested (Figure 6.8) and finally the 5 µm thickness was chosen for printing the first filtering unit.
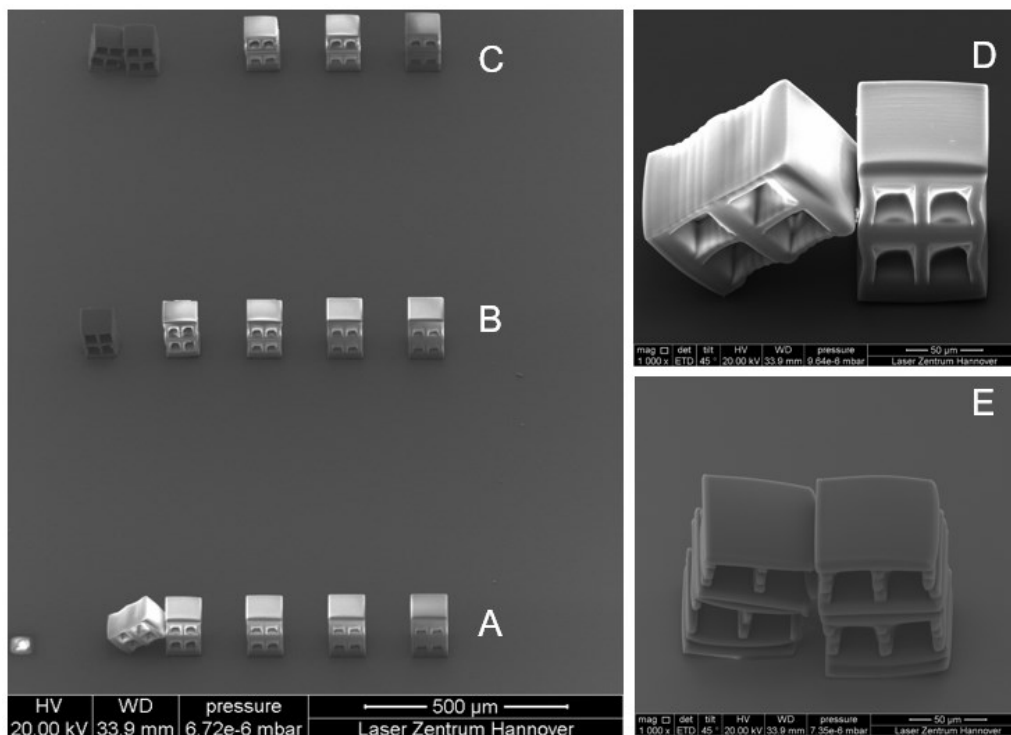
Figure 6.8 - Recursive polymerization test. Layer thickness of A) 3um B) 5um C) 7um D) Over-polymerization effects due to the lower layer thickness E) Under-polymerization effects due to higher layer thickness.

In Table 6.1, all the parameters used for the recursive tests, visible in Figure 6.8, are summarized.

Table 6.1 - Matrix Slicing and laser parameters

Line	Slicing (um)	Scanning Speed (mm/s)	Power(mW)				
A	3	2					
B	5	2	35	40	45	50	55
C	7	2					

In Table 6.2, the commercial material names used to perform various building test are reported.

Table 6.2 - Photocurable resin used for 2PP printing process

Material	Power
OrmoCore 1.8% Irgacure 369 XP	No results
OrmoCore Hybridpolymer	No results
Femtobond© Acrylate + Irgacure 4bis	40/45 mW
Femtobond© Acrylate + Irgacure 369	20/25 mW
Femtobond© 4b	40/45 mW
SPOT HT	No results

Ormocore compounds were commercial 2PP Hybridpolymer available at LZH. Femtobond© are photopolymers especially designed and produced by LZH for 2PP applications. Potentially interesting was also the SPOT HT material: the commercial acrylate compound used to print the microchannel with the SLA printing machine. The intent was to test the 2PP printing feasibility using the same material used for microchannel building. This would totally improve the compatibility and improve the 2PP building integration inside the microchannel. Unfortunately, it didn't work as expected and no optimal parameters were found to obtain adequate results (Figure 6.9). The main problem was the viscosity, too low to support the suspended structures generated by the 2PP process.
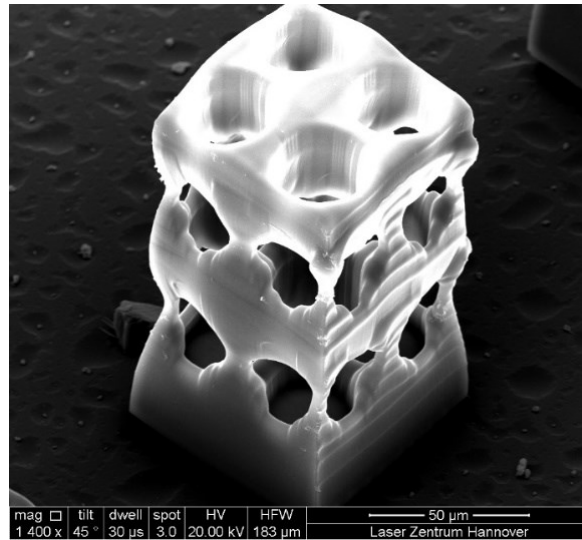
Figure 6.9 - Spot HT 2PP failed building test

Finally, the Femtobond© 4b was chosen for printing at 2 mm/s with a layer thickness of 5um and a laser power of 45mW.

6.4 Filtering Wall

Considering unsatisfactory first tests results, the PoC was modified. To make the printing process easier and faster, the SLA printed microchannel shape and size was modified to allow a smaller filtering unit fabrication, as visible in Figure 6.10. Indeed, 2PP printing time increases with a cubic factor with the total printed object dimension. Thus, the filter design becomes a relevant aspect to optimize the overall printing process without reducing filter functionality.
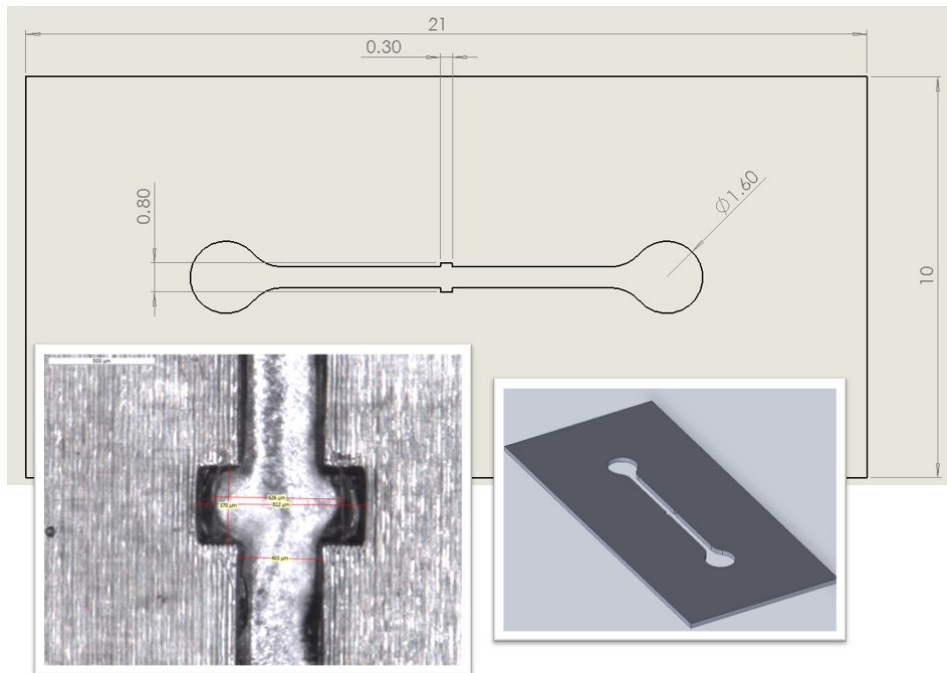
Figure 6.10 - New SLA channel design for improved building performance.

The channel dimension was reduced and a small hollow, in the centre, was designed to sustain the 2PP filtering unit. The inlet and outlet diameters were not modified. This special shape is able to improve both the adhesion of the 3D structure during the printing process and the mechanical resistance during flowing tests. All the SLA printing parameters are reported in Table 6.3.

Table 6.3 - SL parameters for microfluidic chip printing

Parameter	Value
Power	10 mW
Layer Thickness	100 µm
Hatching scan velocity	1000 mm/s
Contour scan velocity	1800 mm/s

After the microfluidic chips were printed, post-curing was performed, for 10 minutes under a 24 W UV lamp, to ensure all the resin to be fully polymerized. A single filtering wall of 900 µm width, 300 µm height and 300 µm thick, with 30 µm pores, was designed to be 2PP printed. As visible in Figure 6.11, Figure 6.12 and

Figure 6.14, the wall design was gradually modified trying to solve a series of issues that emerged from building tests.

Indeed, Figure 6.11 shows the correctly printed wall. Unfortunately, the overall printing time was over 8 hours. Furthermore, considering the total width of 300 µm, it was not well-defined if the "developing" process was able to completely clear inner structure porosities. The imaging by SEM did not allow to observe in depth inside the filtering structure.

Figure 6.11 - 2nd Wall filtering design and SEM analysis of a completed printing process and channel integration.

The wall was modified designing a tunnel inside the filtering structure (Figure 6.12). Thus, the developing fluid would have the capability to permeate inside the whole structure. Regrettably, this design was not so robust, and the structure collapsed on itself.
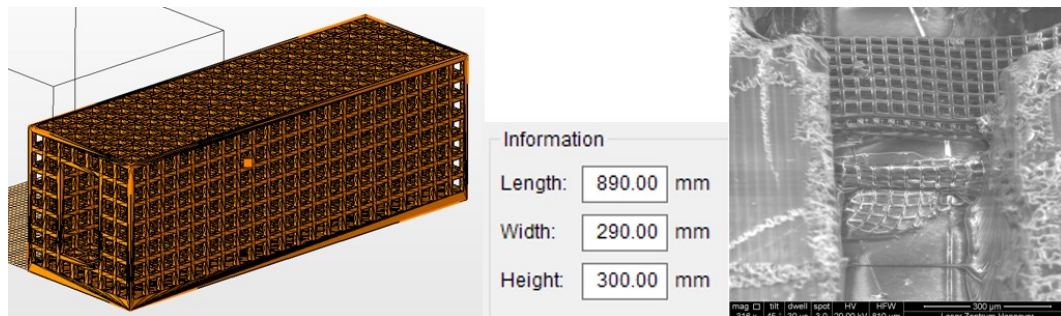
Figure 6.12 – 3rd Wall filtering design and SEM analysis of a completed printing process and channel integration.

The final design was a double wall filtering structure reinforced both by an external frame and with rhomboidal shape section pillars in the middle (Figure 6.13).
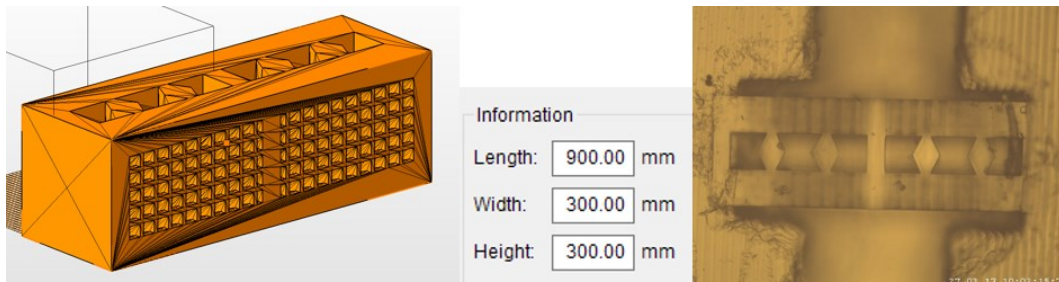
Figure 6.13 - 4th and final Wall filtering design and microscope image proving the completed printing process and channel integration.

This shape will aid the particles movement inside structure during the flowing tests. In Figure 6.14 a SEM image is reported and shows the final wall filter. Each pore is of 30 μm and the total building time is of about 8 hours. It is visible that the filter is correctly integrated with the SLA printed microchannel.
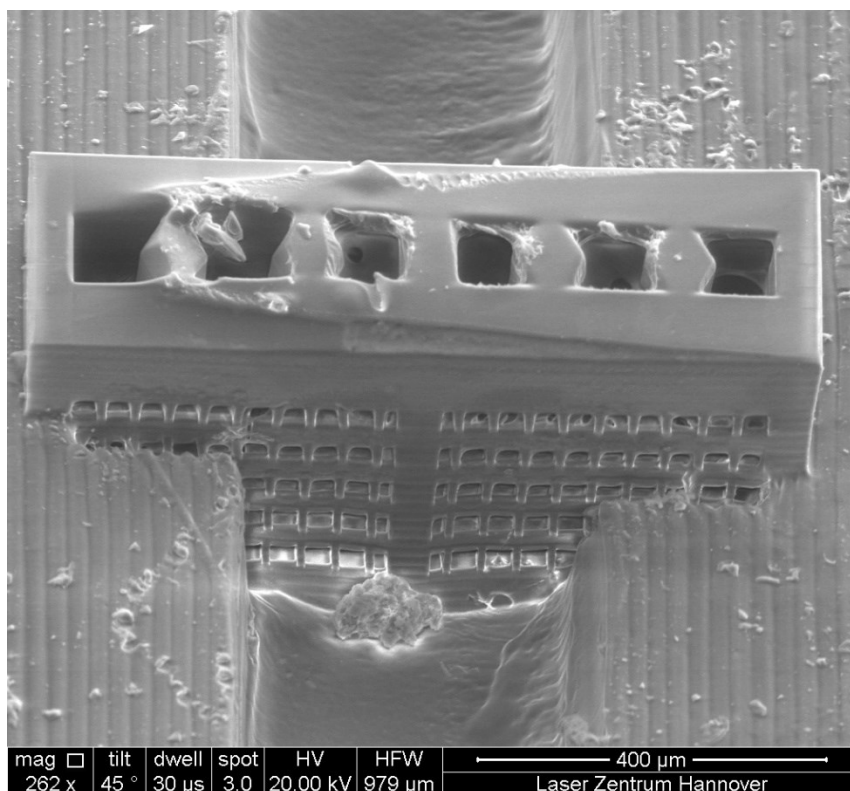
Figure 6.14 - 4th and final Wall filter unit channel integration analysed by SEM.

The drawbacks of building the structures in the z direction are both the high printing time and the loss of resolution. The latter is caused by the laser gaussian power distribution and the consequent lower polymerization control among the XY

direction. Aiming to overcome these drawbacks, a filtering unit with lower thickness was recommended and a new microchannel design was realized to allow an easier integration process.

6.5 800 μm Inlet Filter

The new device geometry presents a single-channel chip with one inlet and one outlet, as reported in Figure 6.15. The channel is designed to be 300 μm wide and 300 μm deep. Inlet and outlet have different dimensions: while the outlet is a 450 μm diameter hole the inlet is a 650 μm diameter hole, with a 200 μm high step-like feature built inside. The diameter reduction inside the inlet works like a construction base allowing the filter outer borders to be supported during the printing process, as visible in Figure 6.15.
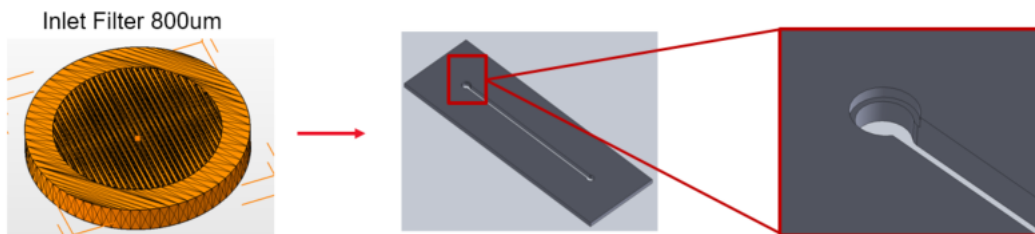
Figure 6.15 - First ring filter design to be printed inside the channel's inlet. Inside the inlet is visible also the step-like feature which act as building support.

The microfilter consisted in a 50 μm thick circular structure with 800 μm diameter. The structure was designed to have two main parts, highlighted in Figure 6.16. A solid full ring (grey) and a filtering grid (blue and cyan). A solid external ring was designed to mechanically strengthen the whole structure and improve the integration inside the SLA printed channel 650 μm inlet. Indeed, during the 2PP printing step, the laser would describe the ring path inside the SLA microfluidic chip walls allowing a better cohesion at the interface between the two structures (microfluidics and filter). The second part, enclosed by the outer ring, was composed by two grids. The first grid, in which 20 μm wide rods, extending for the whole microfilter height, formed a frame of 60 μm wide squared holes. The second grid, composed by 4 μm wide and 5 μm deep small rods, orientated alternatively along x and y direction between subsequent layers, which formed a 4 μm pores that constitute the real filtering structure. The first grid (cyan color in Figure 6.16) improve the mechanical resistance of both the whole filter and the secondary grid (blue color in Figure 6.16), which represented the real filtering unit. This geometry was generated to combine high filtering surfaces and mechanical stability at the same time.
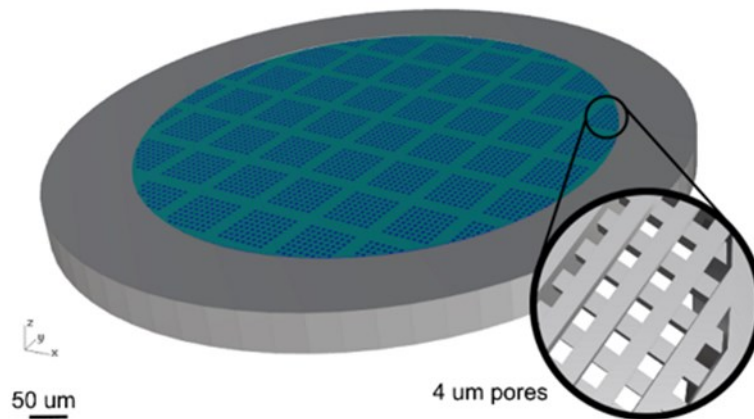
Figure 6.16 - 800um Ring filter design

As visible in Figure 6.17, the filtering structure of 800um diameter is perfectly integrated into the channel inlet. The total printing time, in this case, is reduced to 30 minutes and each pore is about 4 µm. This is a huge improvement in comparison with the filtering wall building time of 8 hours and with the wall maximum porosity size of 30 µm.
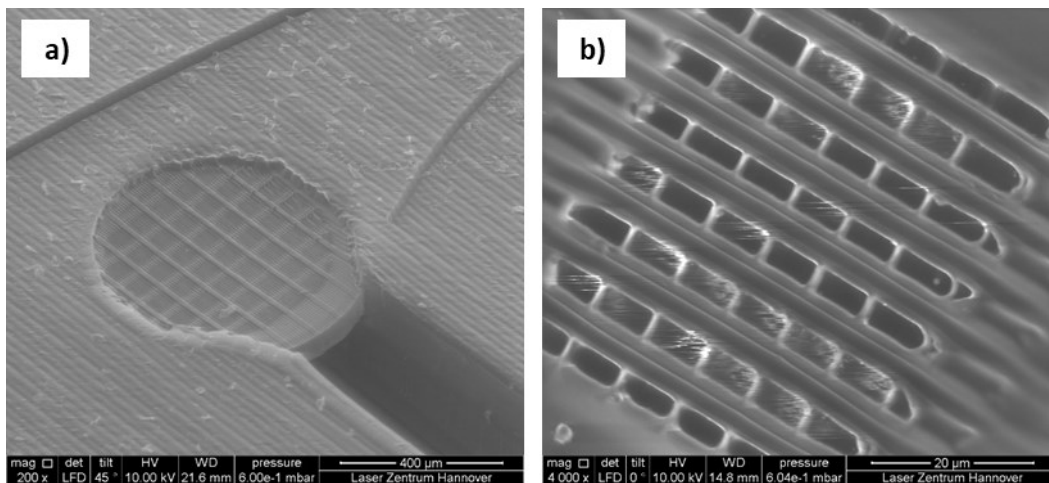
Figure 6.17 - SEM analysis of 2PP printed 800 µm ring filter SLA channel integration. a) The filter outer ring is completely integrated inside the SLA channel. b) 4 µm pores detail.

6.6 400 µm Inlet Filter

Considering the satisfactory results achieved with the 800 µm filter, a new kind of process was developed trying to improve the overall resolution of the filtering unit. A smaller channel was built using a 2PP printed object, acting as a master for a replica moulding process. It was designed with a total length of 3 mm, a depth of 150 µm and with an outlet and inlet diameter of 400 µm (exactly half of the previously SLA printed channel inlet)(Figure 6.18).
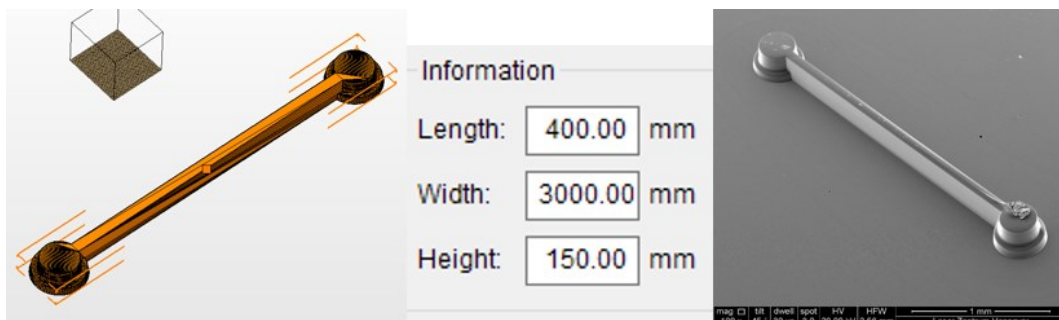
Figure 6.18 - 2PP channel design and relative printed master SEM analysis.

As visible in Figure 6.19 the inlet was designed exactly as the SLA printed cannel negative, including the step like feature.
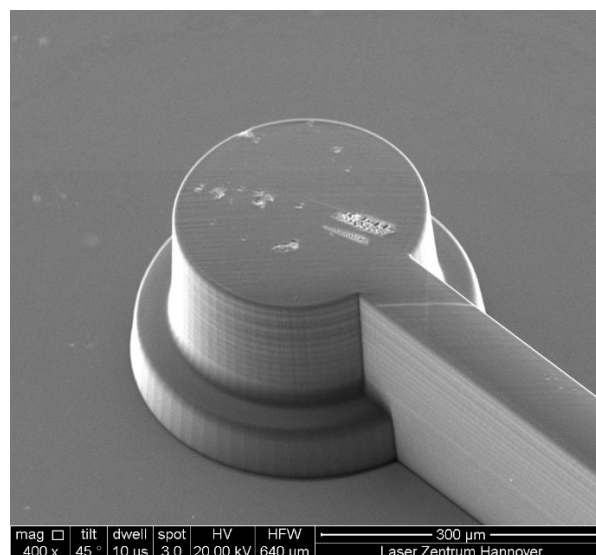
Figure 6.19 - Negative inlet of 2PP printed channel master with the step-like feature

The 2PP printed channel was then covered by thin gold layer and used as a master for replica moulding, as reported in Figure 6.20. PDMS was used to create a

transition master and then, at the end of the process, the final channel was realized with the same photopolymer used for the filtering structure.

In this application, the integration of two different AM techniques was missed but the test intent was to reach a filtering unit with higher resolution, trying to print a 400 μm diameter filter with 2 μm holes, reducing also the overall printing time to 15 minutes.
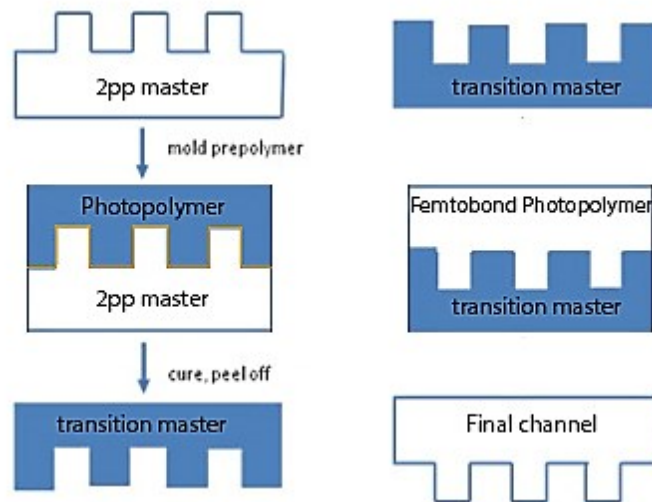
Figure 6.20 - Moulding process sequence.

The results of this last activity are visible in Figure 6.21. The filter is not perfectly built: the failure is due to the aggressiveness of the cleaning and drying process required for achieving the pores neatness.
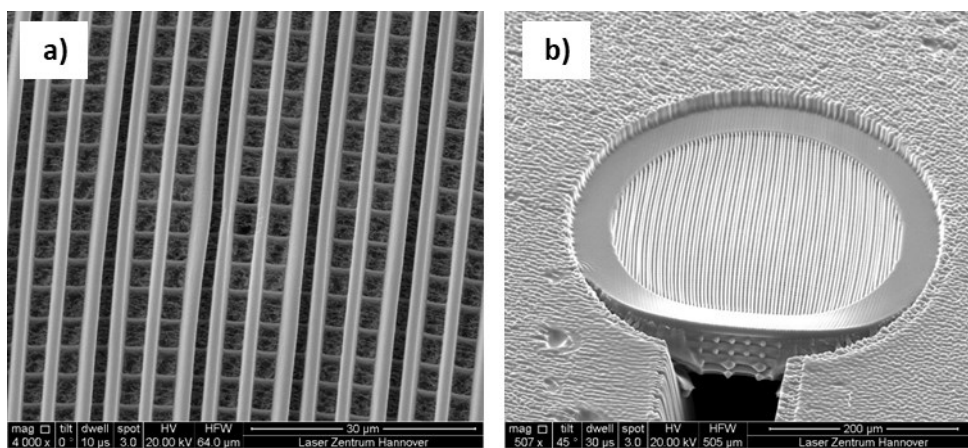
Figure 6.21 - SEM analysis of 2PP printed 400 μm ring filter 2PP channel integration. a) 3 μm size pores b) 400 μm filter damaging after developing process.

Indeed, it was documented that, before the developing and drying process, the filter was correctly built inside the 400 µm inlet, as reported in Figure 6.22.
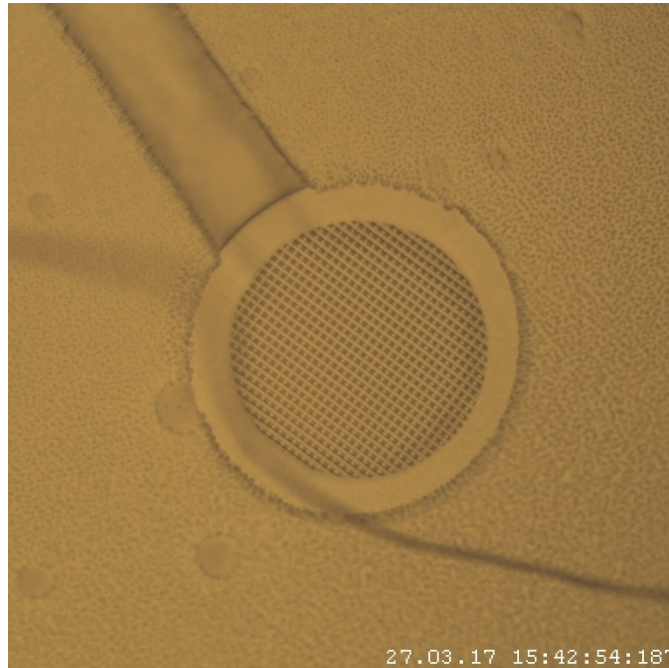
Figure 6.22 - Microscope analysis of a 400 µm filter correctly printed inside the inlet, before the developing and drying process.

6.7 Conclusion

This PhD activity represents one of the first multidisciplinary approach to the 3D printing technology for polymers. A huge group of researchers are working together to define new fabrication paradigm relied to materials, but this goal can be reached simultaneously with both technology and fabrication machine optimization.

Based on this evidence, this thesis work begins from the realization of an open SLA machine able to process both photopolymers available on the market and special matrix compounds produced at Politecnico di Torino. Indeed, the new machine prototype was used to test a non-commercial photopolymer with conductive proprieties. The aim of this research activity is to produce a conductive wire directly inside the additive manufactured object while the building process is still running. A smart device, with concrete functionalities, could be produced only through

additive manufacturing processes. Another candidate's research contribute, always related to smart device fabrication (not reported in this thesis because out of topic) was the graphene-like conversion of polyimide, performed through laser processing, to build supercapacitors or flexible conductive devices. Those interesting results are reported in [38], [44], [45].

The work described in Chapter 6 demonstrated that 2PP technology can work in synergy with other additive manufacturing techniques to obtain microfluidic chips with embedded micro-nano features. In the first part a micrometric wall, with 30 μm pores, was integrated into a SLA built microfluidic channel for filtration purposes. This first tests were mainly realized to validate the integrability of SLA and 2PP 3D printing process in creating devices for cells separation in diagnostic and therapeutic applications.

Considering the lossness of resolution among the z direction the candidate's contribution is related to an accurate and well-studied design and the developing of a printing strategy to speed up the 2PP fabrication step. In particular, the X,Y plan was exploited to build the high-resolution mesh according to a special hatching strategy, thus obtaining a suspended microfilter, with final pores size of 4 μm on a considerable area of 0.5 mm^2, in only 30 min printing process. The optimized building strategy combined with a correct post-processing allowed to 3D print a filter with few hundred nanometres wall able to withstand flows up to 10 μl/min without damages. Indeed, a filter characterization was carried out using FluoSpheres® polystyrene particles (FPs) dispersions, by Thermofisher. A 250 μl Hamilton Gastight syringe was mounted to a programmable syringe pump (NE1000) to control the liquid flow inside the microfluidic chip, while the fluorescence signal was collected by a Zeiss Axio Observer A1 microscope in combination with a 470 nm light source.

The microfluidic filtration system developed in this study was designed to be used on a wide range of cells sorting/filtration as, for example, the blood cells. The particle tracking tests confirmed that it is possible to filter 4 μm size FPs corresponding to the filtering unit porosity size (

Figure 6.23), while smaller ones could easily pass without clogging issues[46].
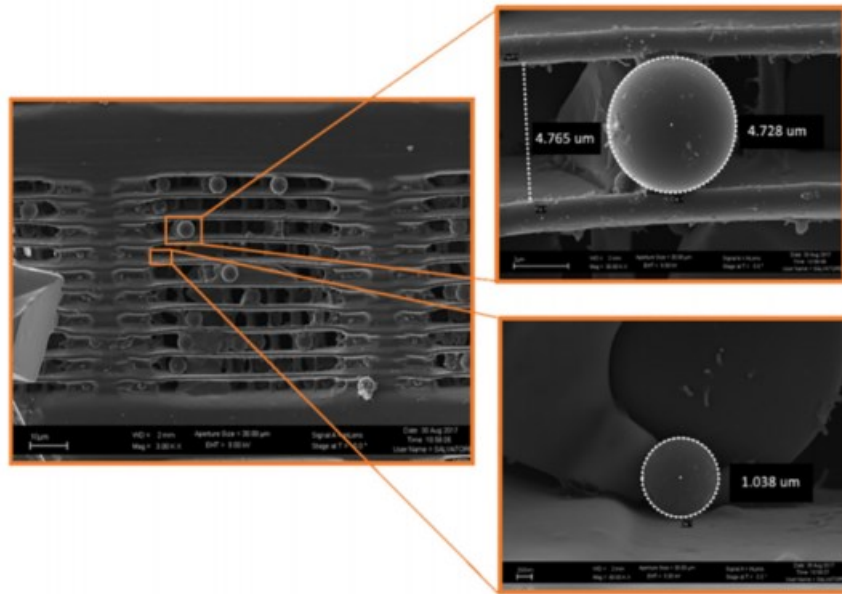
Figure 6.23 - FESEM images of the FPs in the filter.

Future works will be focused on the fabrication of more complex filtration systems to be tested with actual biological samples and to finally achieve a multi-separation device, able to work from micrometric-size cells to nano-vesicles (i.e. exosomes) [47]. Further studies will be performed also to evaluate the scalability of the 2PP printing process and to improve structures design to allow new MEMS device generation.

7   References

[1]   Rofin, "Introduction to Industrial Laser Material's Processing," 2004.

[2]   J. Ready, *Industrial Applications of Lasers 2nd Edition*. 1997.

[3]   M. Stafe, A. Marcu, and N. N. Puscas, *Pulsed Laser Ablation of Solids*. 2014.

[4]   V. Degiorgio and I. Cristiani, *Note di fotonica*. Milano: Springer Milan, 2012.

[5]   H. Ghafouri-Shiraz, *The Principles of Semiconductor Laser Diodes and Amplifiers*. 2004.

[6]   W. Luhs, "Experiment 04 - Diode Laser." MEOS GmbH 79427 Eschbach - August 1998/ July 2003, 1998.

[7]   R. Paschotta, "Q Switching," *RP Photonics Consulting GmbH*, 2018. [Online]. Available: https://www.rp-photonics.com/q_switching.html.

[8]   R. Paschotta, *Field Guide to Laser Pulse Generation*. 2016.

[9]   R. Paschotta, "Mode Locking," *RP Photonics Consulting GmbH*, 2018. [Online]. Available: https://www.rp-photonics.com/mode_locking.html.

[10]   R. Paschotta, "Chirp," *RP Photonics Consulting GmbH*, 2018. [Online]. Available: https://www.rp-photonics.com/chirp.html.

[11]   Wikipedia, "Chirp," 2018. [Online]. Available: https://en.wikipedia.org/wiki/Chirp.

[12]   R. J. Young and P. A. Lovell, *Introduction to Polymers, 3rd edn*. Taylor and Francis, 1991.

[13]   N. G. McCrum, C. P. Buckley, and C. B. Bucknall, *Principles of polymer engineering.* New York: Oxford University Press., 1997.

[14]   M. M. Painter, Paul C.; Coleman, *Fundamentals of polymer science : an introductory text.* 1997.

[15]   American Chemistry Council, "The Basics : Polymer Definition and Properties," pp. 1–9, 2017.

[16] BNP Media, "Radiation Chemistry in EB-and UV- Light-Cured Inks Electron-Beam Curing," *PCI Magazione*, 2000.

[17] D. Voll and C. Barner-Kowollik, "Photoinitiators for Polymer Synthesis. Scope, Reactivity, and Efficiency. By Jean-Pierre Fouassier and Jacques Lalavée.," *Angewandte Chemie International Edition*, vol. 52, no. 12, pp. 3312–3312, Mar. 2013.

[18] J. . Fouassier, X. Allonas, and D. Burget, "Photopolymerization reactions under visible lights: principle, mechanisms and examples of applications," *Progress in Organic Coatings*, vol. 47, no. 1, pp. 16–36, Jul. 2003.

[19] C. Hoyle and J. Kinstle, *Radiation Curing of Polymeric Materials*, vol. 417. Washington, DC: American Chemical Society, 1990.

[20] Yusuf Yagci, "Photopolymerization," 2018. [Online]. Available: http://web.itu.edu.tr/~yusuf/photopolymerization.htm.

[21] Z. Kecici, S. Babaoglu, and G. Temel, "Methacrylated benzophone as triple functional compound for the synthesis of partially crosslinked copolymers," *Progress in Organic Coatings*, vol. 115, no. November 2017, pp. 138–142, Feb. 2018.

[22] A. Jenkins, "Contemporary polymer chemistry(3rd edition). HR Allcock, FW Lampe and JE Mark. Pearson Education, Inc(Pearson/Prentice Hall), Upper Saddle River, NJ, USA, 2003. ISBN 0-13-065056-0 pp xviii+ 814," *Polymer International*, vol. 53, no. 9, pp. 1395–1395, Sep. 2004.

[23] H. Crivello and E. Reichmanis, "Photopolymer Materials and Processes for Advanced Technologies," *Chem. Mater.*, vol. 26 (1), p. pp 533–548, 2014.

[24] K. Obata, A. El-Tamer, L. Koch, U. Hinze, and B. N. Chichkov, "High-aspect 3D two-photon polymerization structuring with widened objective working range (WOW-2PP)," *Light Sci Appl*, vol. 2, no. August, p. e116, 2013.

[25] A. Korkin and F. Rosei, *Nanoelectronics and Photonics*. New York, NY: Springer New York, 2008.

[26] K. S. Lee, D. Y. Yang, S. H. Park, and R. H. Kim, "Recent developments in the use of two-photon polymerization in precise 2D and 3D microfabrications," *Polymers for Advanced Technologies*, vol. 17, no. 2, pp. 72–82, 2006.

[27] I. Gibson, D. Rosen, and B. Stucker, *Additive Manufacturing Technologies*.

2010.

[28]   ASTM International, "Standard Terminology for Additive Manufacturing Technologies," 2012.

[29]   C. Amza, A. Zapciu, and D. Popescu, "Paste Extruder—Hardware Add-On for Desktop 3D Printers," *Technologies*, vol. 5, no. 3, p. 50, Aug. 2017.

[30]   "Polymer Additive Manufacturing and Rheology," 2017. [Online]. Available: https://www.nist.gov/programs-projects/polymer-additive-manufacturing-and-rheology.

[31]   A. Bournias Varotsis, "Introduction to FDM 3D printing," 2018. [Online]. Available: https://www.3dhubs.com/knowledge-base/introduction-fdm-3d-printing.

[32]   R. J. Zaldivar, D. B. Witkin, T. McLouth, D. N. Patel, K. Schmitt, and J. P. Nokes, "Influence of processing and orientation print effects on the mechanical and thermal behavior of 3D-Printed ULTEM®9085 Material," *Additive Manufacturing*, vol. 13, pp. 71–80, 2017.

[33]   3D Matter, "What is the influence of infill %, layer height and infill pattern on my 3D prints?," 2015. [Online]. Available: http://my3dmatter.com/influence-infill-layer-height-pattern/.

[34]   R. Gabbrielli, I. G. Turner, and C. R. Bowen, "Development of Modelling Methods for Materials to be Used as Bone Substitutes," *Key Engineering Materials*, vol. 361–363, pp. 903–906, 2008.

[35]   N. Mankovich, D. Samson, W. Pratt, D. Lex, and J. Beumer, "Surgical planning using three-dimensional imaging and computer modeling.," *Otolaryngol Clin North Am.*, 1994.

[36]   Y. Huang and C. Jiang, "On-line force monitoring of platform ascending rapid prototyping system," *Journal of Materials Processing Technology*, vol. 159, no. 2, pp. 257–264, Jan. 2005.

[37]   G. V. Salmoria, C. H. Ahrens, V. E. Beal, A. T. N. Pires, and V. Soldi, "Evaluation of post-curing and laser manufacturing parameters on the properties of SOMOS 7110 photosensitive resin used in stereolithography," *Materials & Design*, vol. 30, no. 3, pp. 758–763, Mar. 2009.

[38]   G. Gonzalez *et al.*, "Development of 3D printable formulations containing CNT with enhanced electrical properties," *Polymer*, vol. 109, pp. 246–253, Jan. 2017.

[39] H. Gong, M. Beauchamp, S. Perry, A. T. Woolley, and G. P. Nordin, "Optical approach to resin formulation for 3D printed microfluidics," *RSC Advances*, vol. 5, no. 129, pp. 106621–106632, 2015.

[40] K. F. Carr, "Optical Materials: Silicon carbide mirrors benefit high-speed laser scanning," 2008. [Online]. Available: https://www.laserfocusworld.com/articles/2008/04/optical-materials-silicon-carbide-mirrors-benefit-high-speed-laser-scanning.html.

[41] K. Renap and J. P. Kruth, "Recoating issues in stereolithography," *Rapid Prototyping Journal*, vol. 1, no. 3, pp. 4–16, Sep. 1995.

[42] H. S. Cho, W. S. Park, B. W. Choi, and M. C. Leu, "Determining optimal parameters for stereolithography processes via genetic algorithm," *Journal of Manufacturing Systems*, vol. 21, no. 6, p. 465, Jan. 2002.

[43] C. Lynn-Charney and D. W. Rosen, "Usage of accuracy models in stereolithography process planning," *Rapid Prototyping Journal*, vol. 6, no. 2, pp. 77–87, Jun. 2000.

[44] A. Lamberti *et al.*, "All-SPEEK flexible supercapacitor exploiting laser-induced graphenization," *2D Materials*, vol. 4, no. 3, p. 35012, Jul. 2017.

[45] A. Lamberti *et al.*, "New insights on laser-induced graphene electrodes for flexible supercapacitors: tunable morphology and physical properties," *Nanotechnology*, vol. 28, no. 17, p. 174002, Apr. 2017.

[46] F. Perrucci *et al.*, "Optimization of a suspended two photon polymerized microfluidic filtration system," *Microelectronic Engineering*, vol. 195, no. February, pp. 95–100, Aug. 2018.

[47] V. Bertana *et al.*, "3D-printed microfluidics on thin poly(methyl methacrylate) substrates for genetic applications," *Journal of Vacuum Science & Technology B, Nanotechnology and Microelectronics: Materials, Processing, Measurement, and Phenomena*, vol. 36, no. 1, p. 01A106, Jan. 2018.

8   Annex 1

Microsoft Visual Studio Community 2017 Ver. 15.6.2
Microsoft .NET Framework Ver. 4.7.02556
Libraries:
Renci.SshNet.dll Ver. 2016.1.0.0
System.Net.Http.dll Ver. 4.0.0.0

```csharp
using Renci.SshNet;
using System;
using System.Collections.Generic;
using System.ComponentModel;
using System.Data;
using System.Diagnostics;
using System.Drawing;
using System.Linq;
using System.Text;
using System.Text.RegularExpressions;
using System.Threading.Tasks;
using System.Timers;
using System.Windows.Forms;

namespace csharp
{
  public partial class Form1 : Form
  {
    public string output;
    public string output2;
    public int statusButton2;
    public int statusButton10;
    public int Laser_Power { get; private set; }
    public string Laser_Command { get; private set; }
    public int client_laser_control = 0;
    private int client_control = 0;

    static int timer2Counter = 0;
    static int timer1Counter = 0;


    public SshClient client { get; set; }
    public ShellStream { get; set; }
    public SshClient client_laser { get; set; }
    public ShellStream shellStream_laser { get; set; }

    public Form1()
    {
      InitializeComponent();
```

```
        textBox1.MouseClick += TextBox1_MouseClick;


        panel1.Width = 370;
        this.Width = 640;

        timer1.Tick += new EventHandler(timer1_Tick);
        timer1.Interval = 1500;


        timer2.Tick += new EventHandler(timer2_Tick);
        timer2.Interval = 1500;


    }

    //CONNECT DISCONNECT SECTION --------------------------------------------------------
    //-------------------------------------------------------------------------------

    //CONNECT
    private void button1_Click(object sender, EventArgs e)
    {
      try
      {
        client_control = 1;
        button3.Enabled = true;
        client = new SshClient("192.168.10.10", 22, "debian", "temppwd");
        //client = new SshClient("192.168.0.100", 22, "pi", "raspberry");

        IDictionary<Renci.SshNet.Common.TerminalModes, uint> modes = new
Dictionary<Renci.SshNet.Common.TerminalModes, uint>();
        modes.Add(Renci.SshNet.Common.TerminalModes.ECHO, 53);

        textBox2.Text = "Connecting...";
        client.Connect();
        shellStream = client.CreateShellStream("xterm", 80, 24, 800, 600, 1024, modes);

        output = shellStream.Expect(new Regex(@"[$>]"));
        textBox2.Text = output;
        shellStream.WriteLine("cd esc-3dprinter/3dprinter");
        //shellStream.WriteLine("cd Desktop");

        output += shellStream.Expect(new Regex(@"[$>]"));
        textBox2.Text = output;

        ImageButton4.Enabled = true;
        ImageButton5.Enabled = true;

      }
      catch (Exception ex)
      {
        textBox2.Text = "Connection Failed - Press Connect to try again...";
        MessageBox.Show(ex.Message);
      }
    }
```

```
//DISCONNECT
private void button3_Click(object sender, EventArgs e)
{
  try
  {

    if (client_control == 1)
  {
  client.Disconnect();
  client_control = 0;
  }

    if (client_laser_control == 1)
  {
  client_laser.Disconnect();
  client_laser_control = 0;
  }

  button1.Enabled = true;
  button2.Enabled = false;
  button3.Enabled = false;
  button4.Enabled = false;
  button5.Enabled = false;
  button6.Enabled = false;
  button7.Enabled = false;
  button8.Enabled = true;
  button9.Enabled = false;
  button11.Enabled = false;
  ImageButton4.Enabled = false;
  }
  catch (Exception ex)
  {
    MessageBox.Show(ex.Message);
  }
}

//GO_MOVEMENTS SECTION ----------------------------------------------------------------
//------------------------------------------------------------------------------------

//GO_RACLA
private void button4_Click(object sender, EventArgs e)
{
  textBox2.Text = String.Empty;
  shellStream.WriteLine("./go-racla.sh");


  textBox2.Text += "Go Racla...";

  timer2Counter = 0;


  timer2.Enabled = true;
```

```
}

//GO_START
private void button5_Click(object sender, EventArgs e)
{
   textBox2.Text = String.Empty;
   shellStream.WriteLine("./go-start.sh");

   textBox2.Text += "Go Start...";

   timer2Counter = 0;

   timer2.Enabled = true;

}

//GO_0
private void button6_Click(object sender, EventArgs e)
{
   textBox2.Text = String.Empty;
   shellStream.WriteLine("./go-0.sh");
   textBox2.Text += "Go Zero...";

   timer2Counter = 0;

   timer2.Enabled = true;

}


//3D PRINT SECTION------------------------------------------------------------
//-------------------------------------------------------------------------


//3D.sh
private void button7_Click(object sender, EventArgs e)
{
   try
   {
   textBox2.Text = String.Empty;
   shellStream.WriteLine("./3d.sh");
   //shellStream.WriteLine("python code.py");


   //timer
   var stopwatch = Stopwatch.StartNew();
   System.Threading.Thread.Sleep(500);
   stopwatch.Stop();


   textBox2.Text += "3D Print...";
   button2.Enabled = true;
```

```
   button2.Click += new EventHandler(button2_Click);
   button10.Click += new EventHandler(button10_Click);

   timer1.Enabled = true;
   timer2.Enabled = true;


   Application.DoEvents();



   }
   catch (Exception ex)
   {
      MessageBox.Show(ex.ToString());
   }

}

//TIMER TICK CONTROL
private void timer1_Tick(object sender, EventArgs e)
{
   timer1Counter += 1;

   if (statusButton2 == 1)
   {
      ContinueProcess();
   }
   else if (statusButton10 == 1)
   {
      EndProcess();
   }
   else
   {
      ;
   }
}

//private void timer2_Tick(object sender, EventArgs e)
//{

//   output2 = shellStream.Read();

//   if (output2 != output)
//   {
//      textBox2.AppendText(output2);
//      output = output2;

//      // Inserire il timer nel ciclo if rallenta notevolmente la reattività del software
//      // ma permette una corretta lettura dello stream

//      ////timer
//      //var stopwatch = Stopwatch.StartNew();
//      //System.Threading.Thread.Sleep(3000);
//      //stopwatch.Stop();
```

```
//   }
//   else
//   {
//      timer2.Enabled = false;
//   }

//}




//CONTINUE/END PROCESS SECTION -----------------------------------------------------
//----------------------------------------------------------------------------------


//CONTINUE PROCESS - Change status

private void timer2_Tick(object sender, EventArgs e)
{

  timer2Counter += 1;
  //leggo il contenuto di output ogni timer tick
  output = shellStream.Read();

  //se l'output è diverso da un contenuto nullo appendo alla text box altrimenti non faccio nulla
  if (output != "")
  {
    textBox2.AppendText(output);
  }
  else
  {
    ;
  }

}

public void button2_Click(object sender, EventArgs e)
{
  statusButton2 = 1;
  button10.Enabled = true;
}

//END PROCESS - Change status
private void button10_Click(object sender, EventArgs e)
{
  statusButton10 = 1;
  button10.Enabled = false;
}

//CONTINUE PROCESS - Function
public void ContinueProcess()
{
  try
  {
    //timer1.Enabled = false;
```

```
        statusButton2 = 0;

        shellStream.WriteLine("c\n");
        output = shellStream.Read();

        ////timer
        //var stopwatch = Stopwatch.StartNew();
        //System.Threading.Thread.Sleep(3000);
        //stopwatch.Stop();

        timer2.Tick += new EventHandler(timer2_Tick);
        timer2.Enabled = true;
    }
    catch (Exception ex)
    {
        MessageBox.Show(ex.ToString());
    }
}

//END PROCESS - Function
public void EndProcess()
{
    try
    {
        //timer1.Enabled = false;

        statusButton10 = 0;

        shellStream.WriteLine("e\n");

        timer1.Enabled = false;
        timer1Counter = 0;
        timer2.Enabled = false;
        timer2Counter = 0;
        button2.Enabled = false;

        //timer
        var stopwatch = Stopwatch.StartNew();
        System.Threading.Thread.Sleep(6000);
        stopwatch.Stop();

        output = shellStream.Read();
        textBox2.AppendText(output);



    }
    catch (Exception ex)
    {
        MessageBox.Show(ex.ToString());
    }
}

private void label2_Click(object sender, EventArgs e)
```

```
        {

        }


        //LASER SECTION --------------------------------------------------------------
        //--------------------------------------------------------------------------------

        //MINICOM
        public void button8_Click(object sender, EventArgs e)
        {
          try
          {
            client_laser_control = 1;

            //per controllare il laser devo avviare una nuova connessione ssh
            client_laser = new SshClient("192.168.10.10", 22, "debian", "temppwd");

            IDictionary<Renci.SshNet.Common.TerminalModes, uint> modes = new
Dictionary<Renci.SshNet.Common.TerminalModes, uint>();
            modes.Add(Renci.SshNet.Common.TerminalModes.ECHO, 53);

            textBox3.Text = "Connecting Laser Control...";
            client_laser.Connect();
            shellStream_laser = client_laser.CreateShellStream("xterm", 80, 24, 800, 600, 1024,
modes);

            output = shellStream_laser.Expect(new Regex(@"[$>]"));
            textBox3.Text = output;

            //Invio il comando per l'attivazione del controllo Toptica
            shellStream_laser.WriteLine("minicom");

            //timer
            var stopwatch = Stopwatch.StartNew();
            System.Threading.Thread.Sleep(1000);
            stopwatch.Stop();

            output = shellStream_laser.Expect(new Regex(@"\s"));
            textBox3.Text = output;

            shellStream_laser.WriteLine("la on");
            shellStream_laser.WriteLine("en 2");
            shellStream_laser.WriteLine("la off");
            shellStream_laser.WriteLine("pass system");
            shellStream_laser.WriteLine("BlueNOTE!");
            shellStream_laser.WriteLine("config swi ext");
            shellStream_laser.WriteLine("config swi 3");
            shellStream_laser.WriteLine("save swi");

            output = shellStream_laser.Expect(new Regex(@"[^CMD> ]"));
            textBox3.Text = output;

            //timer
            stopwatch = Stopwatch.StartNew();
```

```
        System.Threading.Thread.Sleep(1000);
        stopwatch.Stop();

        shellStream_laser.WriteLine("la on");
        shellStream_laser.WriteLine("en 2");

        //timer
        stopwatch = Stopwatch.StartNew();
        System.Threading.Thread.Sleep(1000);
        stopwatch.Stop();

        output = shellStream_laser.Expect(new Regex(@"[^CMD> ]"));
        textBox3.AppendText(output);

        button8.Enabled = false;
        textBox1.Enabled = true;
        button9.Enabled = true;
        button12.Enabled = true;
        button3.Enabled = true;

    }
    catch (Exception ex)
    {
        MessageBox.Show(ex.ToString());
        textBox2.Text = "Connection Failed - Press Enable Laser to try again...";
    }
}

//DISABLE LASER
private void button12_Click(object sender, EventArgs e)
{
    shellStream_laser.WriteLine("la off");

    //timer
    var stopwatch = Stopwatch.StartNew();
    System.Threading.Thread.Sleep(1000);
    stopwatch.Stop();

    output = shellStream_laser.Expect(new Regex(@"[^CH2,]"));
    textBox3.AppendText(output);

    client_laser.Disconnect();
    client_laser_control = 0;

    button8.Enabled = true;
    button9.Enabled = false;
    textBox1.Enabled = false;
    button12.Enabled = false;
}

//SetPowerFunction - string formatter
public void Setlaserpower()
{
    try
    {
```

```
      Laser_Power = Int32.Parse(textBox1.Text.Trim());

      if (Laser_Power > 120)
      {
        MessageBox.Show("Insert a number between 1 and 120 to set the laser power.");
        textBox1.Clear();
      }
      else
      {
        Laser_Command = ("ch 2 power " + Laser_Power);
        label1.Text = (Laser_Command);
        textBox1.Text = (Laser_Power + "mW");
      }
    }
  catch (FormatException)
  {
    MessageBox.Show("Insert a number between 1 and 120 to set the laser power.");
    textBox1.Clear();
  }

}

//SetPowerFunction
private void button9_Click(object sender, EventArgs e)
{
  try
  {

    Setlaserpower();
    shellStream_laser.WriteLine(Laser_Command);
    shellStream_laser.WriteLine("sh level pow");

    //timer
    var stopwatch = Stopwatch.StartNew();
    System.Threading.Thread.Sleep(1000);
    stopwatch.Stop();

    shellStream_laser.Flush();

    output = shellStream_laser.Expect(new Regex(@"[^CH2,]"));
    textBox3.AppendText(output);

  }
  catch (Exception ex)
  {
    MessageBox.Show(ex.ToString());
  }
}

//MANAGE WINDOW ---------------------------------------------------------------
//---------------------------------------------------------------------

//X WINDOW CLOSE
private void ImageButton1_Click(object sender, EventArgs e)
{
```

```
    if (client_control == 1)
    {
       client.Disconnect();
       client_control = 0;
    }

    if (client_laser_control == 1)
    {
    client_laser.Disconnect();
    client_laser_control = 0;
    }
    this.Close();
}

//X WINDOW MINIMIZE
private void ImageButton3_Click(object sender, EventArgs e)
{
    this.WindowState = FormWindowState.Minimized;
}

//MENU BUTTON - Expand Collapse Window
private void ImageButton2_Click(object sender, EventArgs e)
{
    if (panel1.Width == 55)
    {
       panel1.Visible = false;
       panel1.Width = 370;

       this.Width = 640;
       Transition1.ShowSync(panel1);


    }
    else
    {
       panel1.Visible = true;
       panel1.Width = 55;

       this.Width = 325;
       Transition1.ShowSync(panel1);

    }
}

//CTRL + C
private void button11_Click(object sender, EventArgs e)
{
    shellStream.WriteLine("\x03");
    button2.Enabled = false;
    button10.Enabled = false;

    timer1.Enabled = false;
    timer1Counter = 0;
    timer2.Enabled = false;
    timer2Counter = 0;
```

```csharp
    //timer
    var stopwatch = Stopwatch.StartNew();
    System.Threading.Thread.Sleep(6000);
    stopwatch.Stop();
    output = shellStream.Read();
    textBox2.AppendText(output);

}

//SUDO SU
private void ImageButton4_Click(object sender, EventArgs e)
{
    shellStream.WriteLine("sudo su");

    //timer
    var stopwatch = Stopwatch.StartNew();
    System.Threading.Thread.Sleep(1000);
    stopwatch.Stop();

    shellStream.WriteLine("temppwd");

    //timer
    stopwatch = Stopwatch.StartNew();
    System.Threading.Thread.Sleep(1000);
    stopwatch.Stop();

    output = shellStream.Read();
    textBox2.Text = output;

    button1.Enabled = false;
    button4.Enabled = true;
    button5.Enabled = true;
    button6.Enabled = true;
    button7.Enabled = true;
    button11.Enabled = true;
    label2.Enabled = true;
    textBox1.Enabled = true;
}

//REFRESH STREAM
private void ImageButton5_Click(object sender, EventArgs e)
{
    try
    {
        output = shellStream.Read();
        textBox2.AppendText(output);
    }
    catch (Exception ex)
    {
        MessageBox.Show(ex.Message);
    }

}
```

```
//OTHERS -------------------------------------------------------------
//-------------------------------------------------------------------

private void TextBox1_MouseClick(object sender, MouseEventArgs e)
{

    textBox1.Clear();
}
}
}
```